TABLE OF CONTENTS

	Page No.	
SUMMARY	1	1/A8
INTRODUCTION	2	1/A9
LIST OF SYMBOLS	3	1/A10
WIND TUNNEL AND EXPERIMENTAL EQUIPMENT	7	1/A14
Wind Tunnel	7	1/A14
Tunnel Spanning Wing and Drive System	7	1/A14
Test Airfoil and Instrumentation	8	1/B1
TEST PROGRAM AND COMPUTATIONAL PROCEDURES	11	1/B4
Calibration Procedures	11	1/B4
Test Plan	11	1/B4
Unsteady Data Acquisition	12	1/B5
Force and Moment Computation Procedure	13	1/B6
Aerodynamic Damping Computation Procedure	16	1/B9
STEADY-STATE RESULTS	17	1/B10
Wind Tunnel Wall Corrections	17	1/B10
Steady State Response	18	1/B11
UNSTEADY RESULTS	20	1/B13
Pressure Time Histories	20	1/B13
Force and Pitching Moment Loops	20	1/B13
Discussion of Unsteady Response	21	1/B14
Discussion of Simple Sweep Theory	24	1/C3
Discussion of Aerodynamic Damping and Stability	25	1/C4
FLUCTUATING PRESSURES ON STEADY AIRFOIL	27	1/C6
Background Information	27	1/C6
Time Histories - Unswept Airfoil	27	1/C6
Time Histories - Swept Airfoil	36	1/D1
CONCLUSIONS AND OBSERVATIONS	40	1/D5
RECOMMENDATIONS	42	1/D7

TABLE OF CONTENTS (Cont'd)

		Page No.	
APPENDIXES			
I.	NUMERICAL INTEGRATION ESTIMATE OF UNSTEADY LOAD	43	1/D8
II.	NUMERICAL INTEGRATION METHODS	46	1/D11
III.	WIND TUNNEL WALL CORRECTIONS DUE TO A LIFTING SURFACE IN OBLIQUE FLOW	47	1/D12
REFERENCES		51	1/E2
TABLES		53	1/E4
FIGURES		57	1/E8

NASA :3092

MAY 23 1979

NASA Contractor Report 3092

COMPLETED

ORIGINAL

The Influence of Sweep on the Aerodynamic Loading of an Oscillating NACA 0012 Airfoil

Volume I - Technical Report

A. O. St. Hilaire, F. O. Carta,
M. R. Fink, and W. D. Jepson

CONTRACT NAS1-14373
MAY 1979

NASA

141

NASA Contractor Report 3092

The Influence of Sweep on the Aerodynamic Loading of an Oscillating NACA 0012 Airfoil

Volume I - Technical Report

A. O. St. Hilaire, F. O. Carta,
M. R. Fink, and W. D. Jepson
United Technologies Research Center
East Hartford, Connecticut

Prepared for
Langley Research Center
under Contract NAS1-14873

National Aeronautics
and Space Administration

Scientific and Technical
Information Office

1979

BLANK PAGE

TABLE OF CONTENTS

	Page No.
SUMMARY	1
INTRODUCTION	2
LIST OF SYMBOLS	3
WIND TUNNEL AND EXPERIMENTAL EQUIPMENT	7
Wind Tunnel	7
Tunnel Spanning Wing and Drive System	7
Test Airfoil and Instrumentation	8
TEST PROGRAM AND COMPUTATIONAL PROCEDURES	11
Calibration Procedures	11
Test Plan	11
Unsteady Data Acquisition	12
Force and Moment Computation Procedure	13
Aerodynamic Damping Computation Procedure	16
STEADY STATE RESULTS	17
Wind Tunnel Wall Corrections	17
Steady State Response	18
UNSTEADY RESULTS	20
Pressure Time Histories	20
Force and Pitching Moment Loops	20
Discussion of Unsteady Response	21
Discussion of Simple Sweep Theory	24
Discussion of Aerodynamic Damping and Stability	25
FLUCTUATING PRESSURES ON STEADY AIRFOIL	27
Background Information	27
Time Histories - Unswept Airfoil	27
Time Histories - Swept Airfoil	36
CONCLUSIONS AND OBSERVATIONS	40
RECOMMENDATIONS	42

TABLE OF CONTENTS (Cont'd)

Page No.

APPENDIXES

I. NUMERICAL INTEGRATION ESTIMATE OF UNSTEADY LOAD 43

II. NUMERICAL INTEGRATION METHODS 46

III. WIND TUNNEL WALL CORRECTIONS DUE TO A LIFTING SURFACE IN OBLIQUE FLOW 47

REFERENCES 54

TABLES 53

FIGURES 57

SUMMARY

Aerodynamic experiments were performed on an oscillating NACA 0012 airfoil in the United Technologies Research Center (UTRC) Main Wind Tunnel utilizing a tunnel-spanning wing in both unswept and 30 degree swept configurations. The airfoil was tested in steady-state and in oscillatory pitch about the quarter chord. The unsteady aerodynamic loading was measured using pressure transducers along the chord. Numerical integrations of the unsteady pressure transducer responses were used to compute the normal force, chord force, and moment components of the induced loading.

The main objective of this report was to examine the effects of sweep on the induced aerodynamic load response. For the range of parameters tested, it was found that sweeping the airfoil tends to delay the onset of dynamic stall. Sweeping was also found to reduce the magnitude of the unsteady load variation about the mean response.

A stability analysis of the data was performed. It was determined that at mean incidence angles greater than 9 degrees, sweep tends to reduce the stability margin of the NACA 0012 airfoil; however, for all cases tested, the airfoil was found to be stable in pure pitch.

The fluctuating pressures on a steady airfoil in stalled flow were also examined. Turbulent eddies were found to convect downstream above the upper surface and generate forward-moving acoustic waves at the trailing edge which move upstream along the lower surface.

INTRODUCTION

The need for unsteady aerodynamic data into the dynamic stall regime has long been recognized by helicopter designers, and many investigations have been performed to serve these needs. Examples are the work by Halfman et al. (Ref. 1), followed by unsteady tests performed at the United Technologies Research Center (UTRC) (Refs. 2, 3) and at the Vertol Division of Boeing (Ref. 4). While these tests yielded a great deal of detailed information on dynamic stall, they were all restricted to unswept wing configurations. Swept configurations were not included in these early test programs for two main reasons. First, oscillating swept wing tests were probably beyond the achievable state-of-the-art because of the prohibitive cost and the technical complications of the required facility. Second, it was felt that the main emphasis should be the compilation of straight wing data to serve as a basis for future investigations. Indeed, it was found that the introduction of basic unswept data in tabulated form provided a substantial improvement in the ability to predict rotor blade dynamic response (Ref. 3).

Nevertheless, it is obvious that even under the simplest of inflow conditions, a helicopter rotor blade in forward flight is instantaneously unswept in only two positions; viz., at azimuth angles of 90 deg and 270 deg. Thus, conventional, unswept, two-dimensional aerodynamic testing may not be completely adequate for helicopter rotor blade applictions. This is true because a helicopter blade section undergoes wide variations in Mach number, sweep angle, and incidence angle while traversing the azimuth plane. The wide parameter range encountered in rotor craft is indicated by the plots in Figs. 1 and 2. In Fig. 1 a typical spanwise variation in lift coefficient as a function of Mach number for several blade attitudes (including hover) is shown superimposed on two operating conditions of concern to the designer, the drag divergence region, and the potentially dangerous condition involving severe stall. (Note that the peak in C_L near the blade tip in hover is caused by a trailing vortex encounter.) Figure 2 depicts typical contours of constant sweep angle (solid lines) and constant Mach number (dashed lines) on the rotor disk plane. It is seen that high loading is encountered at moderate Mach numbers on the retreating side of the disk. It is further shown that the blade sweep angle is 15 deg or greater over 60 percent of the rotor disk plane (as shown by the shaded region in Fig. 2).

As the requirements for improved dynamic predictions have increased, the need for unsteady dynamic stall data at nonzero sweep angles has become increasingly more important. To meet these needs UTRC, under Sikorsky sponsorship, has provided a new support structure that has converted the steady-state tunnel spanning model (Ref. 5) into an oscillating airfoil system that is adaptable to sweep angles of 0 deg and 30 deg (Ref. 6). The work reported on herein is essentially a continuation of the tunnel-spanning oscillating airfoil study described in Ref. 6.

LIST OF SYMBOLS

Note: Equation or figure numbers refer to the defining relationship or to the first use of the given symbol.

A	side force, Fig. 8
A_1	Gaussian weighting constant, Eq. (25)
a	test section width, m, Eq. (26)
a_∞	free stream speed of sound, m/sec, Eq. (2)
b	blade semichord, m, Eq. (2)
C	chord force, n, Eq. (4)
C_c	chord force coefficient, Eq. (7)
C_D	drag coefficient, Eq. (14)
C_L	lift coefficient, Eq. (13)
C_M	moment coefficient, Eq. (8)
C_N	normal force coefficient, Eq. (6)
C_W	work coefficient, Eq. (16)
c	blade chord, m, Eq. (3)
$F(x)$	distribution function, Eq. (25)
f	frequency of oscillation, cps
g	distribution function, Eq. (20)
h	test section height, m, Eq. (26)
k_c	chordwise reduced frequency, Eq. (2)
ℓ	roll, Fig. 8

LIST OF SYMBOLS (cont'd)

M	moment, newton-m, Eq. (5)
M_c	chordwise Mach number normal to wing leading edge, Eq. (1)
M_∞	free stream Mach number, Eq. (1)
m,n	integers defining image location, Eq. (26)
N	normal force, newton, Eq. (3)
n	harmonic number, Eq. (18)
p	pressure, newton/m^2, Eq. (3)
p_{uT}, $p_{\ell T}$	linearly extrapolated trailing edge values of pressure, upper and lower surfaces, Eq. (9)
$p_{u_{TE}}$, $p_{\ell_{TE}}$	weighted extrapolated trailing edge values of pressure, upper and lower surfaces, Eqs. (9) and (10)
q	dynamic pressure, newton/m^2, Eq. (6), or velocity induced by image vortex, m/sec. Eq. (26)
Re	Reynolds number
t	time, sec, Eq. (3)
V	velocity, m/sec, Fig. 2
V_c	chordwide velocity normal to wing leading edge, Eq. (2)
W	vertical induced velocity, m/sec, Eq. (28)
W_f	weighting factor, Eq. (11)
X	chordwise coordinate, m, Eq. (3)
y	lateral or spanwise coordinates, m, Eq. (26), or airfoil thickness distribution, m, Eq. (4)
y_i	Gaussian coordinate, Eq. (25)

LIST OF SYMBOLS (cont'd)

Z	vertical axis, Fig. 69
α	incidence angle, deg, Eq. (11)
α_M	mean incidence angle, deg, Eq. (15)
α_u, α_c	uncorrected and corrected incidence angle, deg
$\bar{\alpha}$	pitching amplitude, deg, Eq. (15)
$\Delta\alpha$	incidence angle change due to tunnel boundaries, deg, Eq. (31)
β	dimensionless pivot axis location from leading edge, Eq. (5)
Γ	vortex circulation strength, m^2/sec, Eq. (26)
γ	Gaussian partition point, Eq. (25)
ζ	direction cosine, Eq. (27)
Λ	sweep angle, deg, Eq. (1)
μ	parameter defined by Eq. (11), or advance ratio, Fig. 2
Ξ	aerodynamic damping parameter, Eq. (17)
ϕ_n	nth harmonic phase angle, rad, Eq. (18)
$\chi = x/c$	dimensionless chordwise coordinate
ψ	azimuth angle, deg, Fig. 1
ω	frequency of oscillation, rad/sec, Eq. (2)

Subscripts and superscripts:

$( )_c$	chord

LIST OF SYMBOLS (cont'd)

$( )_l$	lower
$( )_n$	normal or nth harmonic
$( )_s$	steady
$( )_u$	unsteady or upper
$( )_{TE}$	trailing edge

WIND TUNNEL AND EXPERIMENTAL EQUIPMENT

Wind Tunnel

Tests were conducted in the 2.44 m (8 ft) octagonal test section of the UTRC Main Wind Tunnel (MWT). This is a single return, closed throat facility with a maximum speed capability in the 2.44 m (8 ft) section of approximately M = 0.9. The present test program was conducted over a range of freestream Mach number from M_∞ = 0.1 to M_∞ = 0.46. The stagnation temperature of the airstream is held constant over the range 16°C to 60°C (60°F to 140 F) by means of external air exchange valves, and tunnel stagnation pressure equals atmospheric pressure. Hence, at the M_∞ = 0.3 operating condition for the present test the Reynolds number was approximately Re/L = 6.82×10^6/m (= 2.08×10^6/ft), and for the 40.64 cm (16 in) chord model, Re = 2.77×10^6.

Tunnel Spanning Wing and Drive System

A schematic view of the tunnel spanning wing system is shown in Fig. 3 (from Ref. 5). It consists of a tunnel spanning rectangular steel spar approximately 2.44 m (8 ft) in length, plus additional end pieces to complete the spar for installation at several available sweep angles or for installation in different wind tunnels having at least one test section dimension of 1.83 m (6 ft). Interchangeable airfoil-shaped shells with 40.64 cm (16 in) chord are mounted in sections onto the spar to provide the test configuration. It is seen that the model shell consists of two sets of pieces: the upper portions which surround the spar fore and aft, and the lower cover plates which complete the airfoil profile. Also shown is the center span metric section, 20.32 cm (8 in) in width, which mounts to a pair of strain gage balances. The intent of this instrumentation package is to measure airloads far from the tunnel side walls and ceiling. The model chord length allows data to be obtained at representative full scale Reynolds numbers and at a favorable tunnel height to chord ratio of 6.

The model and its oscillatory drive system were supported outside the tunnel walls as shown in Fig. 4. Sliding seals were used to prevent leakage at each end of the span and a variable-speed 56,000 watt (75 hp) motor was used to power the drive linkage. The linkage connecting the motor drive to each end of the tunnel spanning model consisted of an eccentric cam, a vertical push rod, and a crank (cf. Fig. 4). The latter was securely fastened to the spar-end shaft by means of a compression ring coupling device. The resulting airfoil pitching motion was sinusoidal with only a 0.5 percent second harmonic distortion.

An overall downstream view of the test section with the swept configuration installed is shown in Fig. 5. Note that sheet metal end cuffs and aluminum nose pieces were required to extend the profile along the span at each end of the basic 2.44 m (8 ft) model. The portion of the spar end shaft visible in the photograph was located at the joint with the main spar, and was contoured to the basic chordwise airfoil. Also shown in this figure are the center metric section and the adjoining section containing the pressure and hot film instrumentation, both of which are discussed below. An upstream view of this system is presented in Fig. 6, showing the one-third span tension supports from both ceiling and floor of the tunnel to quarter chord pivots located in the model spar. These were installed to reduce oscillatory bending deflections resulting from the small chordwise noncoincidence of model center of gravity and pivot axis as well as from any spurious aerodynamic buffeting. Steady-state oil flow studies have demonstrated that only a small portion of the airfoil surface aft of the quarter chord was affected in the immediate vicinity of the supports, and that the effect on the center span flow was negligible.

Test Airfoil and Instrumentation

The airfoil profile tested in this program was NACA 0012 section. Airfoil coordinates in dimensionless form, are presented in Table I and a cross section view of the airfoil is shown in Fig. 7. Here it is seen that the airfoil consisted of two parts: an upper portion that included both leading and trailing edges, and a lower cover panel. Except for the metric section, these parts were bolted to the steel spar, which occupied most of the center cavity shown in the figure. (Clearance spaces were provided fore and aft of the spar for transducer wires and pneumatic tubing.) The metric section was separated from its neighboring side panels by a 1.27 mm (.050 inch) sealed gap at each end and was bolted to the balance system, which in turn was bolted to the spar.

The balance system consisted of two cylindrical balances each capable of load measurements in six directions as shown schematically in the upper portion of Fig. 8. However, only the normal and chord force vectors were measured in this test program. The lower portion of Fig. 8 summarizes the force system that was used. The normal and chord forces measured by the forward and rear balances are denoted by subscripts F and R, respectively. Chordwise balance offsets relative to the quarter chord are X_1 and X_2, and d is the height of the balance center line above the chordline. A detailed description of the balance system can be found in Ref. 5.

Figure 7 shows the locations of the unsteady pressure transducer measuring stations in a chordwise reference line normal to the span. Primary unsteady pressure data acquisition took place along this line and the number

appended to each measuring station denotes the coordinate location, in percent chord, relative to the leading edge. The twelve suction surface orifices and the eight pressure surface orifices were independently grouped in two Gaussian arrays as described in Ref. 7, from 0.4 percent chord near the leading edge to 97.1 percent chord near the trailing edge. This arrangement is unlike past experience in which the upper and lower surface instrumentation arrays were identical to permit pressure difference computations at each transducer station at any instant. However, an increased resolution of the force distribution is more desirable than a point-by-point difference computation. Furthermore, experience has shown that the pressure surface gradients and magnitudes are much lower than the suction surface gradients and magnitudes under virtually all load conditions. Therefore, the use of high density transducer placement in regions of large pressure gradients near the suction surface leading edge, and low density placement in regions of small gradients everywhere else on the airfoil can produce a significant increase in resolution without significantly increasing the total number of chordwise measuring stations.

An additional orifice was located near the reference line at 1 percent chord to help document the leading edge suction peak behavior. This extra location is shown in the planform view of the suction surface (Fig. 9) which also depicts the complete transducer layout (both pressure and hot film) in both the chordwise and spanwise directions. The location of each transducer or hot film is denoted by a pair of coordinates corresponding to the chordwise and spanwise position, in percent chord, relative to the leading edge and relative to the reference line, respectively. For example, the transducer labeled (14.9, 17.7) was at 14.9 percent chord aft of the leading edge and at 17.7 percent chord along the span from the reference line. The reference line was located at 0.36C (or 36 percent of the chord) along the span, away from of the edge of the metric section.

As seen in Fig. 9, several of the transducers were placed along the span to provide both spanwise arrays and 30 degree arrays. Specifically, four pressure transducers in the reference line (at 0.4, 4.5, 14.9 and 26.8 percent chord) are each part of a two- or three-transducer array along the span, while two transducers in the reference line (at 45.4 and 97.1 percent chord) are each part of a four-transducer array swept at 30 degrees. The swept arrays were aligned in the streamwise direction during swept wing testing. Similarly, there are six hot films placed in a normal chordwise array which is located along a line parallel to and 0.1C away from the pressure reference line. Four other hot films provide additional arrays in both spanwise and 30 degree swept directions. In this figure the pressure arrays are connected by solid lines and the hot film arrays by dashed lines. A complete listing of the pressure and hot film transducer locations can be found in Table II.

All of the miniature pressure transucers used in this test were single-surface absolute transducers rated at ± 0.34 atmospheres (± 5 psi) relative to ambient pressure, with nominal sensitivities of 0.68 mv/atmos (10 mv/psi) at 10 v excitation. Each device consisted of a circular diaphragm 2.36 mm (.093 in.) in diameter on a paddle base 6.1 mm (.24 in.) long. Figure 10 schematically depicts the typical transducer installation. It is seen that the desired pressure responses were monitored by transducers mounted in counterbored (or milled) holes on the opposite surface. After installation each transducer was sealed in place and the sealant was sanded smooth to conform to the local airfoil contour.

All transducer outputs were ac-coupled with "high" pass filters (which rolled off at 6 dB/octave below 1 cps). The steady portion of the signal was recovered with pneumatic static pressure orifices located adjacent to each transducer. In effect, the long tube lengths (approximately 10 m of 1.5 mm diameter tubing) between the pneumatic orifices and the control room scanivalve served as the low pass filter portion of the data acquisition system. The pneumatic portion of the data acquisition system yielded a time average of the signal, equivalent to the zeroth harmonic component of the signal in a Fourier series representation, and the electronically filtered signal represented the total signal with the time average removed. The sum of these measurements equals the complete pressure response at each location.

The hot film devices each consist of a small flat foil sensing region (similar to a miniature strain gage) which is sputtered onto a larger plastic insulating sheet approximately 0.025 mm (0.001 in) thick. The units are bonded to the airfoil surface with epoxy. Each hot film is a resistance thermometer element which reacts to the local heat transfer between itself and the adjacent fluid. This is measured by using a constant-temperature anemometer which completes the bridge circuit and provides all necessary control functions (Refs. 8 and 9). In its simplest application, changes in surface flow behavior are revealed through changes in heat transfer. As the heat transfer from the film to the surrounding fluid changes, the voltage required to maintain constant temperature also changes. The resulting bridge unbalance is recorded and subsequently processed by a digital computer.

The angular displacement of the airfoil was measured using a wire-wound rotary potentiometer with linear response characteristics.

TEST PROGRAM AND COMPUTATIONAL PROCEDURES

Calibration Procedures

Prior to testing, all pressure transducers were individually calibrated. A vacuum line was applied to each location and the diaphragm of each transducer was subjected to pressures approximately 84 cm H_2O (33 in H_2O) below atmosphere. The calibration curves are essentially linear. Balance element calibrations were performed by the direct application of known loads to the metric section. These loads were applied at discrete independent load points such that only one individual component (i.e., normal force, chord force, or pitching moment) was loaded at any given time. The actual procedure is described in detail in Ref. 5.

In addition to static calibrations, no-flow dynamic tare tests were performed at each incidence angle and frequency combination to obtain a dynamic reference. Records were taken of both balance and pressure transducer responses. While the latter were negligible for all conditions, the former responses were large and contained high frequency oscillations of significant magnitude relative to the fundamental response. A Fourier breakdown of a sample response is shown in Fig. 11. In addition to the type of inertial reaction that was observed by Phillipe (Ref. 10) in his oscillating airfoil experiments, the magnitude of the higher harmonic components of the balance response spectrum (Fig. 11) indicates that the amplitude of the pitching motion may have been large enough to also induce a non-negligible, nonlinear mechanical reaction. This nonlinear response is believed to have been further aggravated by the high mass of the metric section and the noncoincidence of model pivot axis with the system center of gravity. (It should be noted that the model was originally constructed for steady-state testing only and the primary design criterion was for a steady load capacity at high Mach number.) One consequence of such an arrangement is that the system becomes susceptible to a vertical bending reaction over the span as the airfoil undergoes imposed pitching motions about the pivot axis. Presumably, the balance response was also aggravated by the constraints of the part-span cable supports. However caused, the resulting contamination of the primary signal made it impossible to use the flow-on balance results obtained in the oscillatory part of this test. Therefore, the data so obtained are not discussed herein.

Test Plan

The unsteady experiments undertaken in the overall study were performed for the matrix of parameters shown in Table III. These parameters were the sweep angle, Λ, the amplitude of motion $\bar{\alpha}$, the mean incidence angle, α_M,

the pitching frequency, f, and the approach Mach number. To provide a standard of comparison, the test results were based on the chordwise Mach number normal to the wing leading edge, M_c, which is related to the free stream Mach number by the formula

$$M_c = M_\infty \cos \Lambda \tag{1}$$

Therefore, M_c = 0.3, 0.4 for both swept and unswept tests whereas M_∞ = 0.3, 0.4 for zero sweep and M_∞ = 0.346, 0.462 for Λ = 30 deg. (One exceptional case at M_c = 0.10 was run at Λ = 30 deg and α_M = 15 deg.) Other parameter values were Λ = 0, 30 deg, $\bar{\alpha}$ = 8, 10 deg, and α_M = 0, 9, 12, 15 deg (for most tests). The choice of frequencies used in this test was predetermined according to Table IV which lists the nominal values of chordwise reduced frequency parameter,

$$k_c = \frac{b\omega}{V_c} = \frac{b\omega}{a_\infty M_c} \tag{2}$$

for the basic test program. The unswept portion of the test was conducted first, and with few exceptions was performed at three values of frequency, f = 4, 8, 10 cps at both M_c = 0.3 and 0.4, as denoted by the horizontal arrows along the right column of Table IV. In the subsequent swept test, the same three frequencies were matched at both Mach numbers, but in addition a chordwise reduced frequency match was obtained between the two Mach numbers, as denoted by the diagonal arrows between the two columns. Specifically, the frequencies used were f = 4, 6, 8, 10 cps at M_c = 0.3 and f = 4, 5.33, 8, 10, 10.67 cps at M_c = 0.4.

In addition to these unsteady tests a substantial steady-state program was performed. Both pressure and balance data were taken and a significant penetration into the stall-flow regime was made over a range of Mach numbers.

Unsteady Data Acquisition

Two FM tape recorders were employed to record the data for subsequent digitizing and computer processing, as indicated in the upper right portion of the block diagram in Fig. 12. Time histories of the unsteady angle of attack and of the several channel of unsteady pressure and hot film response were recorded on the two FM tapes at 1-7/8 inches/sec. In addition, a modified IRIG B time code was simultaneously recorded on each tape. The pulse rise time of the time code was sufficiently short to permit correlation between the two digitized records to within 10^{-4} seconds.

The number of channels of data desired in this test exceeded the available number of data channels (26) in the FM tape system. This was overcome with a two-mode selector switching system (upper right portion of Fig. 12) which allowed up to 52 data acquisition channels to be selected, 26 at a time, for recording through the instrumentation amplifiers onto two analog tapes.

Force and Moment Computation Procedure

The total unsteady aerodynamic normal force, chord force (excluding effects due to viscous drag), and moment are obtained by integrating the time-dependent pressure distribution on each surface independently and then taking the difference between the upper and lower surface loads. The equations are:

$$N(t) = -\underbrace{\int_0^c (p_u(x,t) + p_s(x))dx}_{\text{suction surface}} + \underbrace{\int_0^c (p_u(x,t) + p_s(x))dx}_{\text{pressure surface}}, \tag{3}$$

$$C(t) = -\underbrace{\int_0^c (p_u(x,t) + p_s(x))\frac{\partial y}{\partial x}\,dx}_{\text{suction surface}} + \underbrace{\int_0^c (p_u(x,t) + p_s(x))\frac{\partial y}{\partial x}\,dx}_{\text{pressure surface}}, \tag{4}$$

and

$$M(t) = \underbrace{\int_0^c (p_u(x,t) + p_s(x)(x-\beta c))dx}_{\text{suction surface}} - \underbrace{\int_0^c (p_u(x,t) + p_s(x))(x-\beta c)dx}_{\text{pressure surface}} \tag{5}$$

where subscripts u and s represent the unsteady and steady-state values, respectively. The quantity c is the airfoil chord length and βc is the pivot axis location relative to the leading edge. In the present case, $\beta = 0.25$. Equations (3), (4), and (5) were numerically computed via the trapezoidal rule. A brief discussion of the accuracy of this approach is presented in Appendix I.

The sign convention used in Eqs. (3), (4) and (5) defines the normal force, N(t), the chord force, C(t), and the moment, M(t), to be positive in the upward, upstream, and nose up directions, respectively. These integrations are performed with the tacit assumption that the flow is two-dimensional near the instrumented midspan region and that, as a result, the quantities N(t), C(t) and M(t) are per-unit-span values.

Although the airfoil was tested in the unswept (Λ = 0 deg) and swept (Λ = 30 deg) configurations, the evaluation of N(t), C(t), and M(t) is independent of Λ because the integrations are chordwise rather than streamwise. The effects of sweep on these quantities occur implicitly in the measured responses and are approximately accounted for by nondimensionalizing the integrated results with respect to the velocity component normal to the leading edge. The normal force, chord force, and moment coefficients become

$$C_N(t) = N(t)/cq\cos^2\Lambda \tag{6}$$

$$C_M(t) = M(t)/c^2q\cos^2\Lambda \tag{7}$$

and

$$C_C(t) = C(t)/cq\cos^2\Lambda \tag{8}$$

respectively. This nondimensionalization scheme is based on a steady-state sweep analysis which assumes the flow to be potential and the pressure distribution on the wing to be determined entirely by the magnitude of the normal velocity component, $V_\infty \cos\Lambda$. Although these assumptions may not be consistent with the actual flow environment, the approach is being used as a matter of convenience.

Equations (3), (4) and (5) were used to numerically calculate the chordwise integrals of the unsteady pressure time histories, and Eqs. (6), (7) and (8) were used to convert the integrated normal force, chord force, and pitching moment time histories into coefficient form. Although the transducer locations along the chord correspond approximately to the polynomial roots of the segmented Gaussian quadrature (which is described in Ref. 7), the numerical integration was performed via the trapezoidal rule. (Appendix II presents a brief discussion of the reasons for replacing the segmented Gaussian quadrature approach with a trapezoidal rule integration in the evaluation of Eqs. (3), (4) and (5).) Unlike the Gaussian quadrature approach, the trapezoidal rule requires a knowledge of the end point values of the integration interval; therefore, time-dependent approximations were made of the leading and trailing edge pressure responses of the airfoil prior to integration.

The leading edge pressure response was assumed equal to the average of the forward most transducer signals from each surface. Conversely the trailing edge value of the pressure response for each surface was independently extrapolated from the two rearward most signals of each surface to obtain P_{u_T} for the upper surface and P_{ℓ_T} for the lower surface. Rather than averaging these two values to obtain a common trailing edge response for each surface, a weighting factor, w_f, was introduced to approximate the effects of the shear layer separation at the trailing edge. The time-dependent trailing edge values for the upper and lower surfaces were estimated from the expressions

$$P_{u_{TE}} = (w_f P_{uT} + P_{\ell T})/(1 + w_f) \tag{9}$$

and

$$P_{\ell_{TE}} = (P_{uT} + w_f P_{\ell_T})/(1 + w_f) \tag{10}$$

respectively. The weighting factor was empirical and dependent on both the time-dependent angle of incidence, α, and the freestream Mach number, M_∞,

$$\begin{aligned} w_f &= 1 \quad ; \quad \alpha \leq \mu \\ w_f &= 1 + \alpha - \mu \; ; \; \alpha > \mu \end{aligned} \tag{11}$$

where

$$\mu = 20(1 - M_\infty) \tag{12}$$

Equation (12) is an empirical expression which is based on data (unpublished) supplied by Sikorsky.

Finally, Eqs. (6) and (7) were used to obtain the unsteady lift and pressure drag coefficients of the induced aerodynamic load,

$$C_L = C_N \cos\alpha + C_C \sin\alpha \tag{13}$$

$$C_D = C_N \sin\alpha - C_C \cos\alpha \tag{14}$$

respectively. In these equations, α is given by

$$\alpha = \alpha_M + \bar{\alpha} \sin \omega t. \tag{15}$$

A schematic depicting the load configuration is shown in Fig. 13.

Aerodynamic Damping Computation Procedure

The prediction of airfoil torsional stability is related to the prediction of the transfer of energy between the airfoil pitching motion and the surrounding unsteady flow environment. For torsional motions, the transfer of energy can be computed in terms of the work per cycle coefficient given by

$$C_W = \int_0^{2\pi} C_M d\alpha , \tag{16}$$

For pure sinusoidal motions, the corresponding torsional aerodynamic damping parameter is obtained from the expression

$$\Xi = - \frac{C_W}{\pi \bar{\alpha}^2} . \tag{17}$$

where $\bar{\alpha}$ the pitching amplitude of the airfoil. When Ξ is positive (work done by the airfoil), there is a net transfer of energy from the airfoil to the airstream and the motion is stable. Conversely, a negative value of Ξ represents an unstable motion.

With the aid of Fourier analysis, the damping parameter can be readily estimated from Eqs. (15), (16), (17) and the following expression for C_M

$$C_M = \sum_n C_n \sin (n\omega t + \phi_n), \tag{18}$$

where C_n and ϕ_n are the amplitude and phase angle lead (relative to the airfoil motion) of the nth harmonic component of the periodic moment. The damping parameter reduces to

$$\Xi = - \frac{C_1}{\bar{\alpha}} \sin \phi_1. \tag{19}$$

Therefore, for simple harmonic motions, only the first harmonic component of the unsteady moment is relevant to the stability of the motion. Furthermore, stability is determined by the sign of ϕ_1; that is, whether the first harmonic component of the moment leads or lags the blade motion.

STEADY-STATE RESULTS

Wind Tunnel Wall Corrections

The Tunnel Spanning Wing System (TSW) is designed to minimize wind tunnel wall and ceiling corrections and interference. All model instrumentation used to measure the aerodynamic airloads are located at midspan and in the center of the wind tunnel test section, the point most removed from the tunnel walls. For the UTRC 8 foot octagonal test section, the TSW has a span of 2.44 m (8 ft) and 2.82 m (9.24 ft) for the zero and 30 degree sweep angle installations, respectively. The midspan metric section has a span of only 20.32 cm (8 in.); the dynamic pressure taps are located to the side of the metric section within .457 m (18 in.) of the wind tunnel centerline. Therefore, no instrumentation is any closer to the walls than two model chord lengths (one chord length is .406 m or 16 in.).

For the unswept flow condition, the conventional ceiling and floor corrections (Ref. 11) are relatively small, because the model installed in the UTRC tunnel has a large height to chord ratio of 6; i.e., the ceiling and floor boundaries are well removed. In addition, blockage effects, which tend to increase the local Mach number, are essentially negligible because the model blockage area (thickness times span) is only 2 percent of the test section cross sectional area.

The corrections to free air conditions are computed by methods that are valid only up to stall and/or before any significant flow separation (Ref. 11). This computation is accomplished by superposing a series of images above and below the model using the tunnel ceiling and floor as reflecting planes. For the swept wing, the tunnel walls must also be treated as reflection planes in order that the effect of these boundaries on the local model incidence angle be estimated when comparing swept data with conventional unswept data. A method for accomplishing this is given in Ref. 12 for potential flow. This approach is a variation of the method of images which assumes that the local flow distortion can be estimated by the induced flow generated by the bound vortices representing a lattice of swept wing panels as shown in the sketch

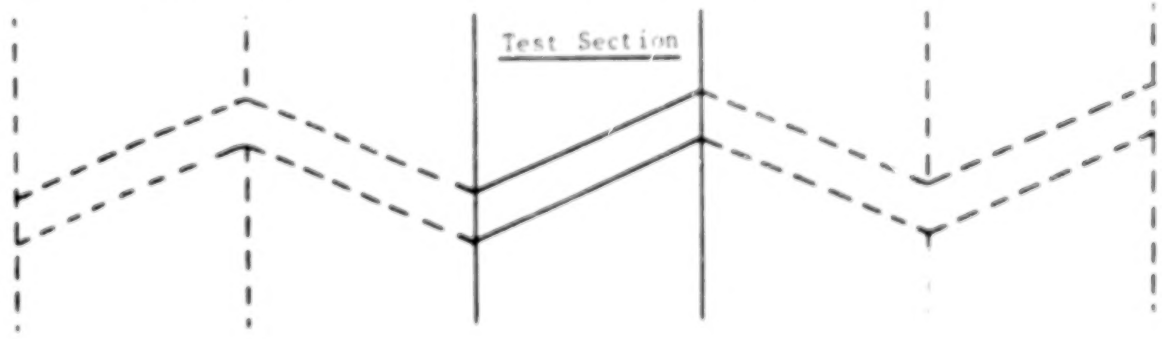

above (representing a planform view in the plane of the model), extending to infinity above, below, and to both sides of the test section. Necessary modifications to the governing equations were introduced to allow evaluation of the induced flow at the airfoil model 50 percent chord station as in the classical theory. The modified equations are presented in Appendix III. To demonstrate the magnitude of these corrections, their effect on the local incidence angle for data taken at the center of the test section and at low Mach number (M_∞ = 0.3) are shown in the table below as a function of lift coefficient:

NACA 0012

C_L	Δa	a_u	a_c
	(degrees)		
0	0	-0.6	-0.6
.4	0.05	3.4	3.45
.8	0.09	7.0	7.09
1.2	0.14	11.0	11.14
1.6	0.18	--	--

The table demonstrates that these corrections to free air conditions amount to about 1.2 percent without consideration of compressibility effects. However, wind tunnel wall corrections to free air conditions were not applied for the dynamic test data.

Some airfoil surface oil flow studies were conducted during a related program (not discussed herein) to investigate possible interference effects of the walls and the part-span support struts. These studies showed that their effects were localized and did not influence the instrumented midspan region. For the dynamic tests it is expected that the strut effects would also be localized.

Steady-State Response

Figures 14 through 17 present the uncorrected lift, drag, and pitching moment coefficient data from metric section balance measurements on the TSW model of the NACA 0012 profile. A data system malfunction made it impossible to retreive the unswept data taken during this test for final data reduction. On-line spot checks of these data, made prior to the malfunction, indicated qualitative agreement with earlier data, and for reference, these previous unswept results (unpublished) are included here in Figs. 14 and 15. The curves for Λ = 30 deg obtained in this test are found in Figs. 16 and 17.

The effect of Mach number is confined primarily to a rounding of the lift curve on the unswept model, and the effect of sweep is to extend the lift curve to higher values of C_L without any significant drop due to stall. Both drag and moment coefficient are relatively insensitive to these effects. Finally, a comparison of the lift curve slopes between the unswept and swept configurations indicates that simple sweep theory can be used to convert unswept steady-state lift data into swept data over the potential flow range of the steady-state response. However, if steady-state swept data are needed beyond stall, current state-of-the-art requires that they be measured directly.

There is a large scatter in the drag measurements at low incidence as shown in Figs. 14 and 15. These results indicate that the present balance system cannot provide sufficiently repeatable steady-state drag data at low Mach number. The deviation in measured drag values is greatest in the neighborhood of the drag divergence knee, especially for the oblique flow cases where the chord force is small. This deviation in measured drag coefficient values was as large as $\Delta C_D = 0.100$.

UNSTEADY RESULTS

Pressure Time Histories

Two examples of the unsteady pressure time histories obtained in this test are presented in Figs. 18 and 19 for mean incidence angles α_M = 0 deg and α_M = 12 deg, respectively. Other test parameters, identical for both cases, were M_c = 0.3, f = 10 cps, k = 0.124, and $\bar{\alpha}$ = 8 deg, and both results were obtained in the swept configuration. In each figure the top trace is for the first chordwise station at x = x/c = 0.004, and subsequent traces are for downstream locations, back to the rearmost trace at x = 0.971. At the bottom of each figure is the angular displacement time history relative to the mean incidence angle. These two results are singled out as typical examples to demonstrate the quality of the measured unsteady pressure distributions and to point out the increased opportunity for a future examination, in detail, of the complex surface phenomena.

The potential flow results in Fig. 18 illustrates the upstroke-to-downstroke symmetry of the response and the large variation in pressure amplitude from leading edge to trailing edge. Note that the double minimum of the leading edge trace over the low incidence angle region signals the passage of the leading edge stagnation point over this transducer, first as it moves rearward for decreasing α, and then as it moves forward for increasing α.

In contrast, the stalled flow penetration case in Fig. 19 contains no evidence of upstroke-to-downstroke symmetry in the pressure response. The most striking characteristic here is the abrupt collapse of suction at x = 0.004 just prior to maximum incidence angle, and the propagation of this event rearward along the chord to the trailing edge. Note that the pressure wave that reaches the trailing edge in Fig. 19 is several orders of magnitude greater than the amplitude of the trailing edge response in Fig. 18 for α_M = 0 deg.

Force and Pitching Moment Loops

The integrations of Eqs. (3), (4), and (5) were performed after the cycle-to-cycle repeatability of the individual pressure transducer responses was verified. A cycle averaging procedure was then used over 5 cycles (Ref. 3) to smooth out any variations of the signals from cycle-to-cycle, thus obtaining a mean representation of the cyclical response signatures of the normal force, moment and chord force coefficients. Equations (13) and (14) were then used to compute the cycle-averaged time histories of the lift and pressure drag coefficients. (Again, it is noted that viscous drag effects are not included.)

With the elimination of time as the independent variable, hysteresis loops are obtained when the cycle-averaged force and moment coefficients are plotted as functions of the airfoil motion. Since normal force and moment loops have been the subject of many earlier reports (e.g., Refs. 1-4, 6, 13 and 14), a detailed discussion of these is not presented herein. Conversely, the computation of the chord force hysteresis response is new (cf. Ref. 14) and its contribution (relative to the normal force contribution) to the lift and pressure drag hysteresis loops is briefly examined. Figure 20 depicts the contributions of C_N and C_C to C_L and C_D for the extreme case in which the unswept airfoil test parameters are f = 10 cps, α_M = 12 deg, $\bar{\alpha}$ = 10 deg and M = 0.4. The upper two loops in the left column depict the normal and chordwise components of the induced load. The upper two loops in the right hand column show their respective contribution to the drag hysteresis loop (shown in the lowermost plot of the right hand column). Here it is seen that the contributions of C_N and C_C to C_D are of comparable magnitude, as might be expected. Conversely, the contribution of C_C to C_L ($C_C \sin\alpha$; not shown) is at least an order of magnitude smaller than that of C_N ($C_N \cos\alpha$; also not shown) even at large values of α. The superposition shown at the lower left of Fig. 20 clearly illustrates this. In contrast to this, Fig. 21 shows how C_N and C_C contribute to C_D for the same test condition with the exception that the mean incidence angle equals zero degrees. A comparison of C_N and C_L is not shown in this case since there are no discernable differences between these force components.

Instead of presenting a detailed discussion of the physics of these loops, the present discussion concentrates on those features of the test results that add to our knowledge of the dynamic stall response in terms of its sensitivity to the various configuration parameters. (Results which include a discussion of periodic transition and separation at the leading edge and the events that follow during the passage of the shed vortex can be found in Refs. 1-4, 6, 13, and 14.) In particular, the integrated quantities of unsteady lift, $C_L(\alpha)$, unsteady pressure drag, $C_D(\alpha)$, and unsteady moment, $C_M(\alpha)$, are used in the next section to parametrically determine the effects of sweep, pitching amplitude, mean incidence angle, frequency, and chordwise Mach number. Also discussed in a subsequent section are the implications of the results in terms of the stability of the pitching motion of the airfoil.

Discussion of Unsteady Response

The discussion of results is based on a limited selection of typical data. A complete set of data can be found in Ref. 15. Figures 22 through 39 compare the unsteady load characteristics of the NACA 0012 airfoil in the swept and unswept configurations. Although the results are presented in a format which emphasizes the effects of blade sweep, the influence of pitching amplitude (Figs. 22-39), mean incidence angle (Figs. 28-36), frequency (Figs. 22-27)

and chordwise Mach number (Figs. 37-39), is also indicated. In each of these figures, the solid and dashed lines represent loops corresponding to th unswept and swept configurations, respectively. In addition, the left hand column of loops shows the effect of sweep at a pitching amplitude of 8 deg while the right hand column depicts the corresponding comparison at a pitching amplitude of 10 deg. Finally, the direction of traverse of each loop is designated by arrows. It is noted that a counterclockwise enclosure of the moment loop indicates that the unsteady aerodynamic load is stabilizing, and that a clockwise traverse is indicative of a destabilization.

Figures 22 through 24 show the effects of sweep, pitching amplitude, and pitching frequency on the lift, pressure drag, and moment responses at constant values of mean incidence angle (α_M = 12 deg) and chordwise Mach number (M_c = 0.30) In Fig. 22 it is seen that the area enclosed by the lift loops, for the range of frequencies shown, grows larger with increasing frequency which means that the unsteady component of lift becomes more important as the pitching frequency is increased. This behavior with frequency is similar for each sweep angle and pitching amplitude tested and is in qualitative agreement with potential flow theory; however, the magnitude of the observed unsteady effect is much larger than indicated by the theory. This is true because the airfoil is operating well beyond the static stall angle, and the dominant effect on the loop shapes is dynamic stall. For the range of parameters shown in Fig. 22, sweeping tends to delay the onset of dynamic stall. This effect is not as discernable at $\bar{\alpha}$ = 10 deg as it is when $\bar{\alpha}$ = 8 deg. Sweep also reduces the magnitude of the unsteady component of the lift force relative to the mean distribution of C_L as a function of α (i.e., the loops for 30 deg sweep are narrower than those for the unswept configuration).

While mean values are important in determining the load capability at a given condition the extremal excursions of the unsteady loads and their locations during the cycle are also important since they are a measure of the dynamic environment. For both the unswept and swept configurations it is seen from a careful examination of the data shown in Figs. 22 through 24 that the peak responses in lift, pressure drag, and moment not only increase in magnitude but also shift to higher incidence angles as the frequency is increased. Beyond the peak response it is seen that the severity of the dynamic stall phenomenon (i.e., the sudden change in C_L, C_D, and C_M near peak incidence) is significantly reduced at low frequencies when the airfoil is swept back. However, as the frequency is increased, the effect of sweep on the dynamic stall response is seen to markedly diminish.

It is well known that in potential flow the unsteady pitching moment about the quarter chord produces an elliptical loop with major axis approximately parallel to the α-axis. In Fig. 24 it is shown that an increase in pitching frequency delays the onset of moment stall for both the unswept and

swept configurations. Also, when the blade is swept back, the nose down impulse which accompanies dynamic stall is reduced in magnitude and occurs over a narrower range of α. This effect is especially noticeable at lower frequencies. Although the effect of sweep tends to favorably alter the moment response near peak incidence, the collective effect of the accompanying change in the unsteady moment response over the entire cycle of motion may be to reduce the stability margin of the airfoil. Further details are presented in the next section. Finally, an increase in the pitching amplitude tends to delay the onset of dynamic stall. This occurs partly because of the delay in the deceleration maximum of the blade motion near peak incidence.

Figures 25 through 27 show the same comparisons as presented in Figs. 22 through 24 but at a chordwise Mach number equal to 0.40. It is seen that the same general trends occur with one exception. For the unswept configuration the increase in Mach number appears to promote a viscous breakdown of the flow at a smaller incidence angle. However, when the blade is swept at $M_c = 0.40$, the unsteady response for both C_D and C_M tends to follow the steady-state characteristics more closely and the maximum achievable loads near peak incidence are seen to exceed those of the unswept configuration, especially when $\bar{\alpha} = 8$ deg.

Figures 28 through 36 show how the lift, pressure drag, and moment hysteresis loops vary with increasing mean incidence angle for both the swept and unswept orientations and at both amplitudes of the motion. The effect of mean incidence angle for a reduced frequency of $k = .099$ ($f = 8$ cps) and a chordwise Mach number of $M_c = 0.30$ is shown in Figs. 28 through 30. As the mean incidence angle increases, th dynamic stall event becomes increasingly more important for both the swept and unswept configurations. For example, at zero degrees mean incidence, the lift force loop is nearly elliptical thus signifying a predominantly potential flow situation. However, when the mean incidence angle is increased until the airfoil oscillation penetrates the dynamic stall region, the resulting loss in lift causes a reversal in the direction of the loop traverse path over part of the cycle. If the event is not too severe as shown in Fig. 28 for the swept airfoil at 9 deg mean incidence and 8 deg amplitude, the unsteady aerodynamic load reassumes a potential flow behavior in the lower incidence angle portion of the cycle. As the mean incidence angle is increased sufficiently, the entire response is influenced by dynamic stall.

Another important outcome of the comparison shown in Figs. 28-30 is that sweep is generally favorable for the entire mean incidence angle range tested at $M_c = 0.30$. In particular, it is noted that the severity of the nose down impulse in the unsteady moment (Fig. 30) is reduced in all cases shown, and even for the extreme cases of $\alpha_M = 15$ deg at $\bar{\alpha} = 8$ deg (note that unswept data at $\bar{\alpha} = 10$ deg was not obtained for this extreme condition).

The comparisons shown in Figs. 31 through 33 are the same as shown in Figs. 28 through 30 except at a lower reduced frequency (k = .049 or f = 4 cps). The trends in loop behavior with respect to α_M and Λ are basically the same as observed in Figs. 28 through 30 but the unsteady responses associated with dynamic stall are generally diminished in magnitude relative to the results obtained at k = .099 (f = 8 cps). Figures 34 through 36 show the same comparisons as in Figs. 28 through 30 but at an increased Mach number (M_c = 0.40). As noted earlier in the discussion of Figs. 25 through 27, the maximum achievable responses of C_D and C_M of the swept configuration generally exceed those of the corresponding unswept configuration for the range of mean incidence angles tested. Otherwise, the hysteresis loops of Figs. 34 through 36 confirm the trends of Figs. 28 through 33. Figures 37 through 39 show more directly the effect of Mach number on the lift, pressure drag, and moment loops. As noted earlier, the airfoil tends to stall at a lower incidence angle as M_c increases from 0.30 to 0.40. For the cases shown, this Mach number effect appears to diminish as the airfoil is swept back.

A special series of runs were made at the chordwise Mach number value of M_c = 0.10. This test was performed for 4 values of frequency (f = 2.5, 3.8, 4.0, and 5.0 cps or k = .106, .156, .212, and .261, respectively) at α_M = 15 deg, $\bar{\alpha}$ = 10 deg, and Λ = 30 deg. These results are shown in Figs. 40 through 42 for C_L, C_D, and C_M, respectively. Here, it is seen that the unsteady load response is qualitatively different from the responses obtained at the higher chordwise Mach number values of 0.30 and 0.40. This difference is especially discernable in the C_L and C_D plots as the reduced frequency is increased. For example, it is noted that as the reduced frequency is increased the loss of lift and pressure drag occurs progressively later in the cycle until it actually occurs after the peak incidence angle is reached. Stated another way, dynamic stall tends to lag the deceleration maximum of the blade motion when the reduced frequency is sufficiently large; that is, the viscous breakdown and accompanying loss in lift occurs during the accelerative phase of the downstroke rather than during the decelerative phase of the upstroke. Finally, it should be noted that the trends shown in Figs. 40 through 42 are in qualitative agreement with the results obtained by the authors of Ref. 14. Figure 30 of Ref. 14 presents C_L, C_D, and C_M loops obtained for the same parameters as herein, but for the unswept configuration.

Discussion of Simple Sweep Theory

In the figures cited in the preceding section it is seen that the unswept and swept lift responses are uniformly displaced from one another during the upstroke portion of the cycle. This displacement occurs at all mean incidence angles except zero degrees in which case the loops are only slightly misaligned. This outcome disagrees with the steady-state result in which the

normalized unswept and swept lift responses are aligned within the potential flow range of the data (cf. Figs. 14 through 17). Therefore, it appears that the use of simple sweep theory to normalize the unsteady lift fails to reconcile the effect of sweep within the potential flow range of the response. An examination of the moment loop comparisons leads to the same conclusion about this limitation of the simple sweep theory.

Discussion of Aerodynamic Damping and Stability

The stability of the airfoil motion in terms of its dependence on parameter variations (sweep, mean incidence angle, and frequency) was determined by performing a Fourier analysis of all of the moment responses obtained in the test program and substituting the first harmonic component values into Eq. (19) to obtain the torsional aerodynamic damping parameter, Ξ, which is positive for stable motions.

Figures 43 and 44 contain the results of the final step in the reduction of the unsteady pressure data for amplitude values of 8 and 10 deg, respectively. These figures show the variation of induced aerodynamic damping with reduced frequency, $k = b\omega/V$, for four values of mean incidence angle and two values of chordwise Mach number.

In Fig. 43 the data obtained at zero mean incidence angle and $M_c = .30$ follow the theoretical linear prediction, $\Xi = \pi k/2$ (cf. Ref. 16); however, when the chordwise Mach number is raised to .40, the qualitative trend deviates from the linear theory as k is increased.

When the mean incidence angle is increased beyond 9 deg, blade sweep tends to reduce the stability margin of the airfoil. In terms of the moment loop results, this outcome implies a net decrease in the area bordered by a counterclockwise traverse path due to the cancellation effect of the clockwise subloops that appear as a result of dynamic stall. The moment loops shown in Fig. 30 are a good illustration of this event. At 12 deg mean incidence the unswept result shown in Fig. 30 represents a mixed condition in which some of the area at each end is enclosed counterclockwise. The central region represents that part of the cycle during which the airstream feeds energy into the motion thus reducing the stability margin. Although sweeping is beneficial from the standpoint of reducing the nose down impulsive moment due to dynamic stall, it is seen that sweeping also intensifies the relative importance of the central portion of the clockwise-traversed subloop for the basic profile.

Figure 44 shows the variation of induced aerodynamic damping as a function of reduced frequency for the case in which the pitching amplitude is set at 10 deg. It is seen that the general behavior of the data is the

same as presented in Fig. 43. For example, at zero mean incidence angle, the unswept results vary linearly with k but with slopes greater than the theoretical prediction. (Comparable swept data were not obtained in this test program.) In addition, as the mean incidence angle increases beyond 9 deg, blade sweep tends to reduce the stability margin of the motion as cited earlier for $\bar{\alpha}$ = 8 deg. Finally, it is noted that unswept data were not obtained at α_M = 15 deg when $\bar{\alpha}$ = 10 deg. Thus it appears that the NACA 0012 profile is stable in pure pitch for the range of parameters tested.

FLUCTUATING PRESSURES ON STEADY AIRFOIL

Background Information

During the course of the test program, the rapid-response pressure transducers and hot film gages on the surface of a nonoscillating airfoil at angles of attack beyond stall onset showed occasional large fluctuations of output. These fluctuations resembled those on airfoils oscillated into stall onset during the increasing-angle portion of their cycle. Qualitative similarity should be expected because the basic features of the aerodynamic flow field are the same. In both cases, the edge of the boundary layer extends relatively far above the airfoil upper surface. These features are sketched in Fig. 45, taken from Figs. 2 and 3 of Ref. 13. The outer part of the thick turbulent boundary layer over the upper surface contains large-scale eddies which are convected downstream at less than free stream velocity. The inner portion of the boundary layer and near wake contains a reversed flow region with maximum velocity magnitude much less than free stream velocity. Because of these similarities, it was expected that improved understanding of aerodynamic phenomena occurring on oscillating airfoils could be achieved from examination of rapid-response data from nominally steady flow past stalled airfoils.

Few other studies of rapid-response flow field data are available for nonoscillating airfoils. Flow visualization data were given in Ref. 13 for a large NACA 0012 airfoil model at a low airspeed (Mach number less than 0.1). The test Reynolds number of 2.5×10^6 was close to that for the present tests, but subsonic compressibility effects were negligible. In contrast to that study of incompressible stalled flow, the investigation reported in Ref. 17 was directed toward an understanding of transonic flow past airfoils undergoing shock-induced separation and trailing edge separation. Fluctuations of suface pressure and wake velocity were analyzed statistically. Crosscorrelation coefficients and time delays were utilized to establish convection of flow disturbances and propagation of pressure waves. This general viewpoint was useful in establishing cause-and-effect relationships between measured flow changes.

Time Histories - Unswept Airfoil

Mach Number 0.30

At a Mach number of 0.30 and steady incidence angle of 15 deg, the unswept NACA 0012 airfoil was just beyond stall. Time histories of fluctuating pressures on the upper surface are shown in Fig. 46. The pressure traces for 1, 7, and 15 percent chord (Fig. 46(a)) were almost identical in shape and

amplitude. Increased downstream distance within that region caused the traces to become less smooth but did not change the general shape of the traces. The signal measured at 0.4 percent chord was about twice as large as those for 1 to 15 percent chord, but all of these signals had the same shape.

In contrast, the signal measured at 27 percent chord (Fig. 46(a)) was similar in general trends but different in detailed shape. The peak which developed between 110 and 125 milliseconds for all of these traces was reproduced, but most of the other broad details were markedly changed in shape. Some peaks had nearly disappeared and others had strengthened. Hot film gages at 15 and 25 percent chord, at a spanwise distance 10 percent chord from the streamwise row of pressure transducers, showed signals in opposite phase to these pressure traces. That is, increased static pressure corresponded to decreased local heat transfer as would be expected.

Further downstream (Fig. 46(b)), the signal at 66 percent chord was about as large as that for 0.4 percent chord and twice as large as those between them. Some major features of the upstream traces persisted, but many of the dominant portions of this signal were not present at the upstream locations. The traces at 85 and 97 percent chord closely resembled each other, and had some features which also occurred at 66 percent chord. They had little resemblance to the well-correlated pressure traces along the forward 27 percent chord.

Relationships between pressure fluctuations measured at different positions can be determined by examining time delays between the signals. Features which did occur in all sets of data, such as the pairs of positive peaks at 67 and 74 milliseconds, and at 176 and 191 milliseconds at 66 percent chord, appeared at the downstream positions 4 milliseconds later. Any time delay in signals along the forward 27 percent chord, and between there and 66 percent chord, was only about one millisecond. These time delays on the forward 2/3 chord correspond to disturbances being convected downstream at close to freestream velocity. A 4 millisecond delay between 66 and 97 percent chord might, at first glance, be regarded as caused by a downstream convection velocity roughly 1/3 that of the free stream. However, this interpretation would not explain why the signal at 85 percent chord has about the same or one millisecond larger time delay. An alternate interpretation is that turbulent eddies convected downstream near the airfoil surface at 66 percent chord move away from the surface within the separated wake, are convected further downstream, and are returned toward the surface within the recirculation region. This return might occur between 85 and 97 percent chord, at positions which vary for each eddy. Thus the pressure signal at either transducer might lead the other.

Pressure traces on the lower surface are compared in Fig. 47 with each other and with those at various positions on the upper surface. Absolute values of pressure fluctuation on the lower surface were largest near the leading and trailing edges, and had very low amplitude elsewhere. To evaluate the flow behavior, each trace was scaled relative to its own rms fluctuation. These self-scaled traces are compared in Fig. 48. This type of presentation shows clearly that the pressure signal at 97 percent chord on the lower surface (second trace) matches the shape of that for the same position on the upper surface (first trace), but is delayed by about 2 milliseconds. Absolute level was less than half that on the upper surface. The signal retains its shape (although it decreases to less than 1/20 its amplitude) between this near trailing edge position and 19 percent chord on the lower surface. Upstream signals occurred roughly 2 milliseconds after those for 97 percent chord. This time delay generally agrees with the 1.3 milliseconds expected for an acoustic wave moving forward against the local airflow on the lower surface which was at nearly freestream velocity. It is well known that convection of turbulence past a trailing edge which is sharp relative to the eddy size will generate acoustic pressure fluctuations. These pressure fluctuations are strongest in the upstream direction, and are much weaker than the fluid dynamic pressure fluctuations associated with the turbulence. The delay time between signals on the lower surface and the rapid decrease of amplitude with distance from the trailing edge are consistent with this aeroacoustic process. Acoustic waves would also be expected to propagate forward from the trailing edge along the upper surface. However, they are too small in amplitude to be observed in the presence of convected turbulence on that surface.

The self-scaled trace for 0.5 percent chord on the lower surface (Fig. 48 (b)) closely matches that for 0.4 percent chord on the upper surface (bottom trace). This result had been expected because the stagnation point for this lifting airfoil lies on the lower surface downstream of 0.5 percent chord so the upper surface streamline passes over this point. Absolute amplitude at the lower surface position was about 1/6 of that for the forward upper surface. The two positions are less than 2.5 percent chord apart in terms of arc length along the airfoil surface. The close match of shape but large difference of amplitude probably corresponds to shedding of turbulence in a locally separated flow near the upper surface transducer. The fluctuating pressure field caused by this turbulence would decay rapidly with distance. It would be superimposed on the steady flow at the lower surface transducer but would not separate that flow.

The self-scaled pressure trace at 1.7 percent chord on the lower surface seems to contain a mixture of the pressure signals which come around the leading edge from the upper surface and those which move upstream along the lower surface. These self-scaled traces are highly irregular because the

absolute level of pressure fluctuation at this position is very low. Note that many portions of the traces at 0.5 and 19 percent chord on the lower surface seem to be of opposite phase. Pressure maximums in one signal nearly match the pressure minimums of the other. This is illustrated more clearly in Fig. 49. The normalized traces at 0.5 percent chord, inverted in sign, generally agree with those measured at about the same time at 19 percent chord. Pressure disturbances may be generated by shedding of turbulence very near the leading edge of the upper surface and convected downstream to the trailing edge, producing sound waves that travel upstream within the lower surface flow. These acoustic waves become reversed in sign when they pass through the stagnation point, which is known to behave as a constant-acoustic-pressure boundary. The transmitted acoustic waves generate disturbances in the flow around the leading edge which affect the unsteady separation. Major disturbances occurred in the pressure signals at intervals of about 20 to 30 milliseconds. However, the time required for a pressure signal to be convected from leading to trailing edge along the upper surface and acoustically propagated back to the leading edge along the lower surface was about 10 milliseconds. If this acoustic wave induced a change in turbulence at the leading edge which then propagated around the airfoil, the phase reversal of pressures near the stagnation point could qualitatively explain a 20 millisecond time interval. Oscillation of the separation point and shedding of turbulent eddies depends on the fluctuating flow properties existing when the acoustic pressure wave arrives. The resulting time duration required for each change of the separation point therefore varies randomly. Thus the feedback mechanism inferred from these pressure data does not produce a highly periodic flow.

In summary, a weak feedback process exists within the flow field adjacent to a stalled airfoil. Turbulent eddies are convected downstream in the separated flow above the upper surface. When each eddy reaches the trailing edge, it generates an acoustic wave which travels upstream in the local flow along each surface. This acoustic wave is much weaker than the fluctuations associated with convected turbulence, so the acoustic wave could not be traced along the upper surface. However, it clearly moved upstream against the attached flow on the lower surface. Arrival of this wave at the lower-surface stagnation point produced an acoustic wave of opposite sign, which moved forward to the leading edge along the lower surface. For some, but not all flow disturbances, arrival of this acoustic wave at the leading edge separation region causes a change in the shed turbulence. This change produces a convected pressure disturbance of opposite sign, resulting in quasi-periodic time histories of unsteady pressure on the airfoil surfaces.

Spanwise variation of flow fluctuations on the upper surface of this unswept airfoil at a Mach number of 0.30 and incidence angle of 15 deg is shown in Fig. 50 for positions near the leading edge. Note that data for

chordwise and spanwise variations were taken at different times, so different nonperiodic unsteady flows are sampled in Fig. 50 than in Figs. 46-48. Self-scaled traces are plotted for static pressures at three spanwise locations along a line parallel to and 0.4 percent chord from the leading edge: at the chordwise reference line and at 26 and 56 percent chord from that line (cf. Fig. 9). Also shown are traces from two hot film gages at 2 percent chord from the leading edge and at 10 and 35 percent chord in the spanwise direction from the line of pressure transducers. Decreased local velocity corresponds to increased local static pressure but decreased local heat transfer. Signals from the hot film gages were therefore plotted reversed in sign so that each flow disturbance would cause both sets of traces to move in the same direction.

All of these self-scaled plots show a response to a flow disturbance at 90 to 100 milliseconds. However, this disturbance peaked about 5 milliseconds later at 0 and 26 percent span than at 35 and 56 percent span. Absolute levels of the fluctuation were up to 6 times larger for positions between 0 and 26 percent span. Other disturbances were strongest in other spanwise regions, and most of the flow disturbances extended over just part of the instrumented position of the span. Essentially the same results were obtained by comparing pressure signals (not shown) at 4.5 percent chord from the leading edge and at spanwise distances of 0, 24, and 53 percent chord from the reference line, and pressure signals at 27 percent chord from the leading edge and at spanwise distances of 0 and 41 percent chord from the reference line.

Spanwise measurements along the forward 27 percent chord of the unswept airfoil therefore show that some but not all flow disturbances extended across the instrumented region. The unsteady flow was more highly correlated in the chordwise than the spanwise direction. This result is consistent with the viewpoint that turbulence shed near the leading edge of a stalled airfoil is nonuniform in its spanwise properties, and changes slowly as it physically convects downstream.

Pressure traces along the chordwise reference line on the airfoil upper surface are plotted in Fig. 51 for an incidence angle of 19 deg at a Mach number of 0.30. Traces measured from 0.4 to 15 percent chord (Fig. 51(a)) had essentially identical shapes. However, the magnitudes of pressure fluctuations at 0.4 and 1 percent chord were roughly 4 and 2 times, respectively, those measured from 2 to 15 percent chord. Magnitudes at the two most forward positions matched those measured at 15 deg incidence angle, but those for the remainder of this region were only about half as large. This could mean that as incidence angle was increased, turbulent eddies shed near the leading edge moved downstream at a larger distance above the airfoil upper surface. The traces became more irregular downstream of 4.5 percent chord.

Agreement in shape of the pressure traces deteriorated considerably between 15 and 27 percent chord (Fig. 51(b)), but many of the pressure oscillations persisted over this distance. In contrast, few if any details of the shape which existed at 27 percent chord were aparent at 66 percent chord. Traces for 85 and 97 percent chord showed general agreement, with the downstream signal leading by one millisecond. Some features of these traces also occurred at 66 percent chord, roughly one millisecond later than at 85 percent chord. These time delays correspond to an upstream convective velocity of about 0.6 times free stream velocity. Of course, accuracy of the time delay and therefore of this velocity ratio is very poor. Magnitudes were about the same for these three aft locations, and were about twice those from 2 to 27 percent chord. This result shows that the turbulent eddies were close to the airfoil surface in this aft region.

Pressure fluctuations on the lower surface are shown in Fig. 52. Those at 97 percent chord on the lower surface closely matched the shape of those for the same location on the upper surface. They were about 40 percent as large, and generally occurred two milliseconds later in time. However, the lower surface pressure transducer at 83 percent chord generally showed a zero to one millisecond time delay relative to pressure disturbances at 97 percent chord on the upper surface. Amplitudes at 83 percent chord were about half those at 97 percent chord on the lower surface. This ratio is consistent with the ratio of 3/17, or about 0.42, predicted for acoustic waves generated at the trailing edge by turbulence that is coherent over a spanwise distance larger than the distance from 83 percent chord to the trailing edge.

Pressure traces for this incidence angle clearly show pressure maximums on the upper surface near the leading edge (Fig. 51(a)) at times of about 130 to 135 and 150 to 155 milliseconds, with pressure minimums near 120, 140, and 160 milliseconds. These patterns generally can be traced downstream (Fig. 51(b)) to sharp maximums near the trailing edge of the upper surface at about 140 and 160 milliseconds. Self-scaled traces, presented in Fig. 53, show that the sharp peaks became broader as they moved upstream along the lower surface with little time delay. These broad pressure maxima at 19 percent chord on the lower surface approximately coincided in time with the pressure minima measured near the leading edge on both surfaces. This portion of the time histories resembles that which would be expected for the periodic feedback loop described for 15 deg incidence angle.

Surface pressure and hot film traces at various spanwise positions near the leading edge for an incidence angle of 19 deg are shown in Fig. 54. As with 15 deg incidence angle (Fig. 50), they showed occasional spanwise coherence in time at which large flow disturbances occurred. These events were not equal in strength along the spanwise instrumented region. Many of

the flow disturbances affected three of the six transducers located very near the leading edge, corresponding to a lateral extent of about 1/3 chord.

Further increases of incidence angle decreased the pressure fluctuations on the airfoil upper surface to about half those for angles just beyond stall. The irregularities in shape of those traces along the chord were so severe that it was not clear whether disturbances moved upstream or downstream along the upper surface. Pressure traces on the lower surface clearly corresponded to acoustic waves moving upstream from the trailing edge to 19 percent chord. Interpretation of data for the forward lower surface and entire upper surface at more than 20 deg incidence angle was uncertain.

Mach Number 0.40

Pressure traces for a Mach number of 0.40 and 12 deg incidence angle are plotted in Fig. 55. Absolute levels of pressure fluctuation over the upper forward 27 percent chord (Fig. 55(a)) were 3 to 4 times those measured at a lower Mach number of 0.30. Dynamic pressure had increased by a factor of about 1.7, so these large amplitudes correspond to a doubling of fluctuating pressure coefficient between the two Mach numbers. Absolute levels of fluctuating pressure coefficient at a Mach number of 0.4 were about 0.014 at 0.4 percent chord and 0.01 elsewhere in this forward region. These levels are much smaller than the values of 0.06 to 0.08 cited in Ref. 17 for positions under an oscillating shock wave or 0.03 downstream of that shock. In attached flow at this Mach number and 10 deg incidence angle (not shown), fluctuating pressure coefficients were only about 0.001. The local flow field near the leading edge of this airfoil at a Mach number of 0.4 and these incidence angles is transonic. Flow separation probably is initiated by a shock wave rather than by a distributed adverse pressure gradient.

Inviscid attached flow around this NACA 0012 airfoil at a Mach number of 0.40 and 12 deg incidence angle was calculated with the transonic flow computer program of Ref. 18. A region of locally supersonic flow was predicted to develop in the expansion around the leading edge. This region was predicted to have a maximum height of about 0.1 chord and maximum local Mach number of about 1.5, and to be ended by a shock wave at about 7 percent chord. The actual stalled flow over this airfoil at this test condition undoubtedly had a much smaller extent of locally supersonic flow and smaller maximum local Mach number. The small magnitude of fluctuating pressure coefficient relative to that for transonic free stream Mach number is likely to reflect the much smaller size of this locally supersonic region.

The shapes of the pressure traces along the forward upper 27 percent chord clearly were convected downstream from the leading edge. Shapes measured at 66, 85, and 97 percent chord on the upper surface (Fig. 55(b))

also appear to be convected downstream. However, there was a major difference between the shapes measured at 27 and 66 percent chord. Self-scaled plots of all traces are compared in Fig. 56. Except for an adjustment in time, the two signals for 27 and 66 percent chord appear to be 180 deg out of phase. This is shown in Fig. 57 by comparing the inverse of the pressure at 27 percent chord, delayed an arbitrary 5 milliseconds, with that for 66 percent chord. With this reversal of phase, they match closely.

Phase reversal between signals from adjacent pressure transducers was reported in Ref. 17 for two conditions. Fluctuations at 10 percent chord (the closest position to the leading edge) on the upper and lower surfaces of that airfoil were of opposite phase, and pressure waves were stated to propagate upstream along the upper surface. This same behavior was noted here for pressure waves moving upstream on the lower surface to 19 percent chord and the pressure traces measured between 0.5 percent chord on the lower surface to 27 percent chord on the upper surface. The fluid-flow mechanism which causes this shift is likely to be a chordwise fluctuation of the stagnation point, driven by the weak acoustic pressure waves. Phase reversal also was noted in Ref. 17 to occur between pressure traces measured upstream and downstream of a shock wave. In the example studied in Ref. 17, the cause of this behavior was the transmission of upstream-moving pressure waves through a shock wave. In the example of these data for separated flow on an NACA 0012 airfoil at a Mach number of 0.4, the cause may be transmission of downstream-moving turbulence through a shock wave.

It should be recognized that unsteady flow past an airfoil undergoing shock-induced separation of a turbulent boundary layer can occur in the absence of upstream flow disturbances. Calculated time-dependent solutions of the Reynolds-averaged compressible Navier-Stokes equations are given in Ref. 19 for transonic flow past a thick nonlifting airfoil at a Reynolds number of 11×10^6. It had been expected that numerical solutions of the time-dependent equations would approach steady solutions which include strong interactions between the airfoil shock wave and turbulent boundary layer. Steady flow without separation at the shock wave but with trailing edge separation was calculated for the lowest transonic Mach number, and steady flow with shock-induced separation was calculated for a higher Mach number. For an intermediate transonic case, an unsteady periodic flow with shock-induced separation was computed. Changes of shock wave position and strength on one surface of the airfoil produced oscillations of static pressure near the trailing edge. These changes of pressure affected the boundary layer thickness near the trailing edge of the airfoil's opposite surface, inducing a change in its shock wave position and strength. This change then fed back through the boundary layer to the trailing edge, reversing the shock wave displacement on the initial surface. The calculations had been conducted because wind tunnel tests exhibited this flow hysteresis over a range of Mach

number. Thus an unsteady flow field can occur as a result of coupling between shock-induced separation and the adjustment of the separated flow near the airfoil trailing edge, even if the upstream flow is steady.

Absolute-level pressure traces for a Mach number of 0.4 and 14 deg incidence angle are plotted in Fig. 58. Traces over the forward 27 percent chord of the upper surface (Fig. 58(a)) were in good agreement and corresponded to a disturbance convected downstream. Absolute levels measured at 0.4 percent chord corresponded to a fluctuating pressure coefficient of only about 0.005, and those from 10 to 27 percent chord were only about 1/4 as large. However, absolute levels at 66, 85, and 97 percent chord (Fig. 58(b)) were as large as those at 0.4 percent chord. Pressure traces at these aft positions had considerably more high-frequency content then did those measured further upstream. Self-scaled versions of these data are shown in Fig. 59. A reversal of phase similar to that for 12 deg incidence angle seemed to occur between 66 and 85 percent chord (Fig. 59(a)) and to be convected to 97 percent chord on the upper and then transmitted to the lower surface. Pressure traces moved upstream along the lower surface (Fig. 59(b)) to 19 percent chord in about 3 milliseconds, as is reasonable for acoustic pressure waves moving against the local flow. Normalized traces at 19 and 0.5 percent chord on the lower surface (Fig. 59(b)) also were 180 deg out of phase.

These two examples of phase reversal in normalized pressure traces on the aft upper surface and forward lower surface are plotted in Fig. 60 with one trace of each pair reversed in sign. On the upper surface, some but certainly not all of the pressure disturbances occurred first at 85 percent chord and appeared several milliseconds later at 66 percent chord. As with the data discussed in Ref. 17, these acoustic disturbances were reversed in sign as they traveled upstream through the shock wave into a region of locally supersonic flow. These high frequency disturbances (periods less than 10 milliseconds) also passed around the trailing edge and traveled upstream along the lower surface. However, they were superimposed upon lower-frequency disturbances with periods of 30 to 50 milliseconds. These latter disturbances, reversed in sign, occurred at 19 percent chord on the lower surface several milliseconds later than at 0.5 percent chord on the upper or lower surfaces. Data at a Mach number of 0.40 therefore exhibit two types of pressure fluctuation. Each undergoes a phase reversal as it passes through a shock wave or stagnation point on the airfoil surface.

Pressure traces at 19 deg incidence angle (not shown) had more high-frequency content than those for smaller angles or the smaller Mach number. Pressure fluctuations were relatively large on the aft upper surface near and downstream of the shock wave. Further increase of incidence angle to 25 deg halved the amplitudes of pressure fluctuation from those at 14 and 19 deg. Chordwise uniformity of the pressure traces was increased, with disturbances

being convected downstream past the upper surface at about 2/3 free stream velocity. Spanwise uniformity was decreased, with few disturbances extending as far as 0.3 chords.

Time Histories - Swept Airfoil

Sweepback of a lifting airfoil produces lateral displacement between streamline locations on the upper and lower surface. Calculated streamlines on the surface of an NACA 0012 airfoil with 30 deg sweepback, for incompressible flow at a lift coefficient of one, are plotted in Fig. 61. The streamline which moves over the upper surface is displaced toward the swentforward side. Because its local velocity on the upper surface is larger than free stream velocity, its local direction is rotated from the free stream direction toward a normal to the leading edge. The lower surface streamline that originates at the same stagnation point has less than free stream velocity, so it is displaced in the sweptback direction and rotated away from a normal to the leading edge. Streamlines that were adjacent at the stagnation point would have spanwise positions roughly 20 percent chord apart at streamwise distances greater than midchord. Now consider a flow disturbance of limited spanwise extent, convected along the upper surface to the trailing edge. The resulting acoustic disturbance produced at the trailing edge must travel upstream along the lower surface for a longer distance before it reaches the stagnation line. Thus it will be weaker than for the unswept case, and its spanwise location of maximum strength will be displaced relative to the initial path of the flow disturbance. The apparent feedback process therefore should be weaker for swept than for unswept airfoils.

Mach Number 0.30 Normal to Leading Edge

Absolute-level pressure fluctuation on a line normal to the leading edge of the 30 deg sweptback NACA 0012 airfoil at a freestream Mach number of 0.346 and 15 deg incidence angle are plotted in Fig. 62. (Incidence angle was measured in a reference plane perpendicular to the leading edge.) At this sweepback and Mach number, the component of freestream velocity normal to the leading edge had a Mach number M_c of 0.30 as with the tests of the unswept airfoil. This combination of Mach number and incidence angle in the plane perpendicular to the leading edge had produced a highly unsteady stalled flow past the unswept airfoil. However, as can be seen from Fig. 62, static pressure fluctuations on the swept airfoil were small except on the upper surface very near the leading edge. Flow past sweptback wings at high angles of attack is typified by local boundary layer separation on the forward upper surface, flow of this separated air in a direction nearly parallel to the leading edge, and reattachment at a slightly larger chordwise position. The separating flow thus encloses a leading edge vortex which produces attached

downstream flow at angles of attack, in the plane normal to the leading edge, that would stall a two-dimensional flow.

Self-scaled plots of these traces are shown in Fig. 63. As can be recognized from Fig. 61, the line of transducer locations normal to the leading edge cuts across the streamlines. Pressure traces over the forward 11 percent chord of the upper surface (Fig. 63(a)) were highly correlated, with time delays that corresponded to disturbances being convected downstream. By 27 percent chord there was little similarity with the upstream traces. Traces measured further downstream were poorly correlated with one another. There was little relationship between pressure traces at 97 percent chord on the upper and lower surfaces (Fig. 63(b)), or between those at aft and forward locations on the lower surface.

This comparison shows that the sweptback airfoil had relatively steady unstalled flow at a test condition for which the two-dimensional flow in a plane normal to the leading edge had been highly unsteady and stalled. Sweepback therefore delayed onset of unsteady stalled flow at constant Mach number and incidence angle in a reference plane normal to the leading edge. Inviscid-flow simple sweepback theory would indicate no effect of sweep if those two parameters are held constant.

Absolute-scaled pressure traces on the upper surface along two lines parallel to the free stream at 20 deg incidence angle are plotted in Fig. 64. The measurement at 0.4 percent chord and one spanwise location (Fig. 64(a)), and also (not shown) at the nearest hot film gage at 2 percent chord, had a shift in measured level between 130 and 150 milliseconds. At the other spanwise location, this flow change appeared (Fig. 64(b)) as a region of very little pressure fluctuation at 0.4 percent chord and (not shown) very small fluctuations of heat transfer at 2 percent chord between 130 and 170 milliseconds. However, the pressure transducers along both lines at 4.5 percent chord had no distinctive behavior during that time interval. Relatively quiescent flow for durations of 50 to 100 milliseconds had also been observed on the unswept airfoil (Fig. 50). Perhaps the flow past a small spanwise region becomes reattached near the upper surface leading edge for occasional short intervals of time.

In contrast to the highly irregular pressure traces over the forward 27 percent chord, the signal at 97 percent chord (Fig. 64(a)) consisted of strong discrete spikes at intervals of about 10 milliseconds, separated by low-amplitude fluctuations. This type of signal also was observed (not shown) for a hot film gage at 45 percent chord. Amplitude of these pulse-like signals was larger than had been measured for all but the most upstream pressure and hot-film locations. This waveform had not been observed in tests of the unswept airfoil at the same Mach number and at an incidence angle of 19 deg in the plane normal to the leading edge.

Some understanding of this flow process can be obtained from self-scaled plots of pressures on a line normal to the leading edge. Data for the airfoil upper surface are presented in Fig. 65(a). Strong positive pulses occurred at 0.4 percent chord at about 90, 120, and 160 milliseconds. These persisted to 2 percent chord (not shown) but by 4.5 percent chord they were reversed in sign. These pulses remained negative to 66 percent chord but were positive at 85 and 97 percent chord. In general, pulses occurred slightly earlier at downstream than at upstream locations. The total difference along the upper surface was only about 2 milliseconds, which corresponds to the time required for an acoustic disturbance to travel upstream one chord length against the free-stream velocity.

Self-scaled pressures on the lower surface, and near the leading and trailing edges of the upper surface, are shown in Fig. 65(b). Pressure pulses at about 0.5 percent chord on the upper and lower surfaces had oppposite signs. Phase reversal between these two positions had never occurred in tests of the unswept airfoil. Another reversal of sign took place between 1.7 and 5.5 percent chord on the lower surface. Pressure pulses occurred at very nearly the same time for all positions on the lower surface. There was some indication that acoustic pressure pulses were traveling upstream at the speed of sound within the local flow beneath the airfoil. That flow had a velocity considerably less than the freestream, and the time required would be only about one millisecond. These weak pressure pulses might be caused by small discrete turbulent eddies convected over the trailing edge to generate trailing edge noise, or by shock wave oscillation. They moved upstream at the speed of sound within the local flow, and reversed their sign on the lower surface near the stagnation point and on the upper surface at about 2/3 to 3/4 chord and again near the leading edge. Disturbances arriving at the leading edge from the upper and lower surfaces had opposite phase, but those on the upper surface had much larger magnitude.

Strong pressure fluctuations on the upper surface at larger incidence angles could be followed from 0.4 to 97 percent chord with about 5 milliseconds time lag. This time is consistent with convection of turbulence along the swept-wing streamlines at close to free stream velocity. Some of these disturbances occurred over the entire instrumented spanwise distance of 43.3 percent chord normal to the free stream. A few pressure spikes such as were observed at 20 deg incidence angle also occurred at larger angles. For sufficiently large incidence, unsteady flow over this sweptback airfoil qualitatively resembled that for the unswept airfoil at the same Mach number normal to the leading edge and at large incidence. Amplitudes of the fluctuations, however, were considerably larger than for the unswept airfoil.

Mach Number 0.40 Normal to Leading Edge

Data were also obtained for the 30 deg swept airfoil at a free stream Mach number of 0.462, which provides a Mach number of 0.40 normal to the leading edge. Absolute-level pressure fluctuations on a streamwise line at that Mach number and 16 deg incidence angle are plotted in Fig. 66. Pressure fluctuations at 0.4 percent chord on this sweptback airfoil had much lower amplitude than those for the unswept airfoil at smaller incidence (Fig. 58). They contained sharp spikes of pressure fluctuation separated by relatively quiescent flow. This type of wave form had been observed further aft on the sweptback airfoil at the lower Mach number and 20 deg incidence angle. Traces measured at the other three positions (4.5, 27, and 97 percent chord) were of different shape and lower amplitude. They had large high-frequency content, as had been found for the unswept airfoil at 0.40 Mach number. Because of the short time interval between successive fluctuations, there is no assurance that any one pressure pulse can be traced along the measurement line. Some of the negative pressure spikes at 0.4 percent chord, such as the three between 213 and 225 milliseconds, coincide with weak positive spikes at 4.5 percent chord.

Absolute-level plots of pressure fluctuation along lines normal to the leading edge are shown in Fig. 67. The forward upper surface (Fig. 67(a)) from 0.4 to 4.5 percent chord had a generally similar shape, with increased pressure between 100 and 190 milliseconds. The pressure spikes which occurred at 0.4 and (not shown) 1 percent chord had essentially disappeared by 2 percent chord. Also, they did not occur at 0.5 percent chord on the lower surface (not shown). By 10 percent chord the time interval of general pressure increase had changed to one of pressure decrease which persisted to 15 percent chord. Traces measured further aft on the upper surface are shown in Fig. 67(b). The highly chaotic strong high-frequency fluctuations measured at 27 percent chord do not resemble those measured either upstream or downstream of that position. They resemble the pressure field downstream of a shock wave (Ref. 17). Smaller-amplitude fluctuations were measured further aft. Those at 85 and 97 percent chord generally match in shape and amplitude, with events occurring first at 97 percent chord. Measurements for the lower surface (not shown) are consistent with pressure waves moving upstream at the speed of sound relative to the flow. Thus the pressure traces illustrate the occurrence of different flow processes on the upper surface within the first 1 to 2 percent chord, between these and 10 to 15 percent chord, and near the quarter-chord. Pressure fluctuations on the lower surface and aft upper surface consist of disturbances moving upstream from the trailing edge or wake. The changes in flow behavior over the first few percent chord, and chordwise location of large high-frequency pressure fluctuations corresponding to the presence of a shock wave, do not match the data measured at the corresponding Mach number and angle of attack of the unswept airfoil.

CONCLUSIONS AND OBSERVATIONS

The following is a list of the more significant findings of this test program. Items 1 through 7 are associated with the oscillatory wing study, and Items 8 and 9 were observed from pressure fluctuation measurements taken during steady-state testing.

1. In general, sweep tends to delay the onset of dynamic stall. In addition, sweep reduces the magnitude of the unsteady components of lift, pressure drag, and moment relative to their corresponding mean response (i.e., the swept wing loops are generally narrower than those for the unswept wing).

2. For both the unswept and swept configurations, an increase in frequency tends to increase the magnitude of the unsteady component of lift about its mean value, $\bar{C}_L(\alpha)$. Furthermore, the peak responses in lift, pressure drag, and moment increase in magnitude and shift to higher incidence angles as the frequency increases within the range of frequencies tested.

3. At low frequencies, the severity of the sudden change in lift, pressure drag, and moment near peak incidence is significantly reduced when the wing is swept. However, as the frequency is increased, this effect of sweep is markedly diminished.

4. The simple sweep theory method of normalization aligns the swept and unswept steady-state lift response within the potential flow range of the data. Conversely, it appears that the application of this normalization procedure to treat unsteady data fails to reconcile the effect of sweep on the lift response in this flow range.

5. An increase in pitching amplitude at constant frequency tends to delay the onset of dynamic stall, thus suggesting a relationship between the onset of dynamic stall and the magnitudes of $\dot{\alpha}$ and $\ddot{\alpha}$.

6. When the wing is unswept, an increase in Mach number (from 0.30 to 0.40) causes dynamic stall to occur at a smaller incidence angle. This effect is less discernable when the wing is unswept.

7. Both the unswept and swept configurations were found to be stable in pure pitch over the range of parameters tested. However, at mean incidence angles greater than 9 deg, sweep tends to reduce the stability margin of the motion.

8. Pressure fluctuations on a steady NACA 0012 airfoil at incidence angles beyond stall include downstream convection of turbulence from the suction surface leading edge, forward propagation of acoustic waves in the attached flow adjacent to the pressure surface, and unsteady shock waves on the suction surface. Amplitude of pressure fluctuations associated with convected turbulence was much larger than that of the acoustic waves.

9. Pressure fluctuations on a steady airfoil at incidence angles beyond stall are reversed in phase when they pass through a stagnation point or a shock wave. The resulting pressure fluctuation which is fed back to the suction surface leading edge region tends to restore the flow toward its average levels.

RECOMMENDATIONS

1. An attempt should be made to modify the simple sweep theory for application under dynamic conditions. It is recommended that swept data be estimated from unswept measurements and that the discrepancies between estimated and measured values be identified. It is also recommended that future experimental programs include several runs at very low frequencies, beginning in each case with a steady-state point. This data would be used to empirically modify the simple sweep theory to account for the effects of frequency in the normalization of measured responses.

2. Unsteady pressure data on pitching airfoils should be examined for the types of static pressure fluctuations which were observed on steady airfoils beyond stall. Possible relevance of the unsteady feedback process to onset and recovery from unsteady flow separation should be established.

3. Unsteady pressure data taken in future tests should be digitized at a time scale small enough to permit following the propagation of acoustic waves along the chord.

APPENDIX I

NUMERICAL INTEGRATION ESTIMATE OF UNSTEADY LOAD

The purpose of the strain gage balance system was to obtain a direct measure of the induced unsteady aerodynamic load, including the normal and chord force components, and the moment. The normal and chord force components would then be used to compute the induced lift and drag forces. However, because the balance element responses were contaminated with a high frequency signal, this part of the test program was not successfully completed. Therefore, an attempt was made to estimate the unsteady chord force component via an integration of the induced chordwise pressure transducer response distribution.

For the reasons cited in Appendix II, the integration was performed via the trapezoidal rule rather than the more powerful segmented Gaussian quadrature approach. The accuracy of the trapezoidal rule approach was examined by using it to compute the induced loading from a known integrable pressure distribution function and then comparing the result with an accurate approximation of the exact value of the induced load. For the sake of simplicity this evaluation was restricted to the suction surface load response and to a simple airfoil shape. It is further noted that the test for accuracy was performed using only one specific suction surface distribution function and no attempt was made to formally evaluate the accuracy of the present trapezoidal rule integration scheme in the generalized sense.

The suction surface pressure distribution function that was used (cf Ref. 7) is given by

$$g(\chi) = 100\chi e^{-(50\chi-1)} + \frac{3}{4}\chi^{1/7}(1-\chi), \tag{20}$$

and is shown plotted in Fig. 68. The function $g(\chi)$ represents the extremes of a typical suction surface pressure distribution with little or no separation; that is, a sharp leading edge region peak response followed by a non-negligible response toward the trailing edge. The simple airfoil shape that was used is given by

$$y(\chi) = .06\sqrt{1-\frac{1}{9}(8\chi-3)^2};\ 0 \le \chi \le 3/5 \tag{21}$$

$$y(\chi) = .12(1-\chi);\ 3/5 \le \chi \le 1.$$

In this equation the forward 60 percent chord is represented by an ellipse and the aft 40 percent chord is assumed to be a linear taper toward the trailing edge. The airfoil shape has a thickness to chord ratio of 0.12, and has continuous derivatives at the 60 percent chord matching point. It should be noted that the only criteria used in choosing the functional forms given by Eqs. (20) and (21) is that they are reasonable, simple representations of the induced load distribution and the airfoil shape.

The exact values of the normal force, chord force, and moment were computed from Eqs. (20) and (21) and are given below to four place accuracy:

$$\text{Normal Force} = \int_0^1 g(\chi)\, d\chi = 0.4150 \tag{22}$$

$$\text{Chord Force} = \int_0^1 g(\chi)\, \frac{\partial y}{\partial \chi}\, d\chi = 0.0588 \tag{23}$$

$$\text{Moment} = \int_0^1 g(\chi)\, (\chi - 1/4)\, d\chi = 0.0120 \tag{24}$$

By using the suction surface coordinates given by χ = 0, .004, .010, .019, .045, .073, .098, .114, .149, .268, .454, .658, .851, .971, and 1.000, the trapezoidal rule yields the following computed results:

Normal Force = .4130; error = 0.5%
Chord Force = .0574; error = 2.4%
Moment = .0094; error = 21.7%

The major source of error in the computation of the moment occurs in the region $.454 < \chi < .851$, and is mainly a consequence of the coarseness of the grid. However, the absolute value of the moment is small (comparable to a steady-state condition below stall) and the error is within the range of normal experimental accuracy. Compared with a typical maximum moment value of order 0.1 the computed error is more like 2 percent of full scale. Furthermore, it is important to note that the estimate of both normal force and chord force in this case is excellent.

Although this prediction was made for only one special situation, it indicates that a satisfactory measure of the induced unsteady chord force can generally be obtained by this method.

Finally, if the segmented Gauss quadrature approach is used (cf Ref. 7) with the following transducer locations: .004, .020, .045, .073, .098, .114, .148, .268 .454, .664, .851, and .970, the computed values become

Normal Force = .4150; Error = 0%
Chord Force = .0594; Error = 1.0%
Moment = .0120; Error = 0%

These results are a promising indication that present techniques are capable of yielding accurate calculations of all forces and moments on both steady and oscillating airfoils, provided that an appropriate integration scheme is used with an adequate number of measuring stations. However, additional calculations with a coarser trapezoidal grid have shown a significant deterioration in accuracy for the specific functional distribution of Eq. (20). It is expected that this work will be pursued further to perform the following tasks:

1) Modify the analytical form of Eq. (20) to simulate changes in load distribution so the present transducer arrangement can be evaluated in greater depth.

2) Expand the technique to assist the experimentalist in selecting both the number and placement of measuring stations to minimize error.

APPENDIX II

NUMERICAL INTEGRATION METHODS

During the planning stages of test program, the intention was to lay out the pressure transducer array in such a way as to permit integrating the induced pressure distribution via the segmented Gaussian quadrature approach described in Ref. 7. By design, with the aid of Gaussian quadrature theory, the upper and lower surface distributions were to be monitored with 12 and 8 pressure transducers, respectively. However, the precise location of the transducers is crucial to the success of the approach and the machining errors made during the pressure tap drilling process were large enough to cause the concept to be abandoned for the time being. Therefore, an extra tap was introduced at the one percent chord location (relative to the leading edge) thus increasing the number of taps on the upper surface to 13 and the integration of the pressure distribution was carried out using the standard trapezoidal rule. However, for completeness (and for future reference) a brief summary of the two-segment Gaussian quadrature approach follows.

The two-segment Gaussian quadrature representation of the integrated distribution function $F(\chi)$ is

$$\int_0^1 F(\chi)\,d\chi = \gamma \sum_{i=1}^{n} A_i F(\chi_i) + (1-\gamma) \sum_{i=n+1}^{m} A_i F(\chi_i) \tag{25}$$

where A_i are weighting constants, χ_i are transducer locations, and γ is some partition point within the nondimensional airfoil chord range $[0,1]$. The first and second Gaussian quadratures of Eq. (25) operate in the chord ranges $[0,\gamma]$ and $[\gamma,1]$, respectively. The transducer locations, χ_i, are directly related to the Gauss points, y_i, of each quadrature where $\chi_i = \gamma y_i$ and $\chi_i = \gamma + (1-\gamma)y_i$ are the relations corresponding to the first and second quadratures, respectively. The main advantage of the segmented Gaussian quadrature over the use of one quadrature applied over the entire chord is the freedom to choose the precise location of any one transducer station along the chord. The specification of this transducer station determines the value of the constant γ. This feature leads to the main limitation of the theory which is that A_i and y_i are exclusively determined by the chosen order of the quadrature. It follows, that once γ is known, the locations of all other transducers are automatically specified.

The accuracy of the Gaussian quadrature approach is directly related to the accuracy of the station point locations. Finally, it is pointed out that the superiority of this approach over conventional methods such as the trapezoidal rule is determined by the fact that a much smaller number of transducers is needed to achieve the same accuracy in the integrated result.

APPENDIX III

WIND TUNNEL WALL CORRECTIONS DUE TO A LIFTING SURFACE IN OBLIQUE FLOW

The wall corrections presented below arise because the lifting surface is immersed in a bounded flow and the normal-to-span chord lines are skewed at an angle, Λ, relative to the free stream. These corrections do not include the effects of solid and wake blocking, and buoyancy which arises if the tunnel has a longitudinal static pressure gradient. These effects are considered in Ref. 11 and must be added to the following corrections. The present analysis will follow the approach developed in Ref. 12 with some modifications as noted below.

In order to compare the steady-state test results for the swept wing with those for the unswept wing, it is necessary to consider tunnel-wall interference effects on both wings. Analysis of the problem for the swept wing indicates that it is necessary to determine the extent to which the tunnel walls alter the incidence angle from what it would be if the walls were not present. This discussion is limited to swept wings placed midway between the upper and lower tunnel walls. Hence, the correction to the incidence angle is considered to be dependent upon the magnitude of tunnel-wall-induced velocity at the horizontal center plane of the wind tunnel.

For an infinite yawed wing in potential flow, lines of constant pressure are parallel to the leading edge of the wing. Ideally, the flow over the swept wing of this test program should correspond to the flow over the infinite yawed wing. However, because the vertical tunnel walls function as reflection planes, the actual wing corresponds more nearly to a panel of a "kinked" wing, as illustrated in the sketch below. In the computation of the tunnel-wall corrections, the lines of constant pressure are considered parallel to the leading edges of the respective wing panels. It is realized that adjacent to the vertical walls, the lines of constant pressure are no longer parallel to the leading edge but are curved and become normal to the walls at the walls. With this discrepancy in flow alignment, the computed corrections are not expected to be adequate adjacent to the vertical walls. The calculated corrections should be satisfactory for correcting to approximately free-air conditions for sections of the wing more than one chord length from either wall.

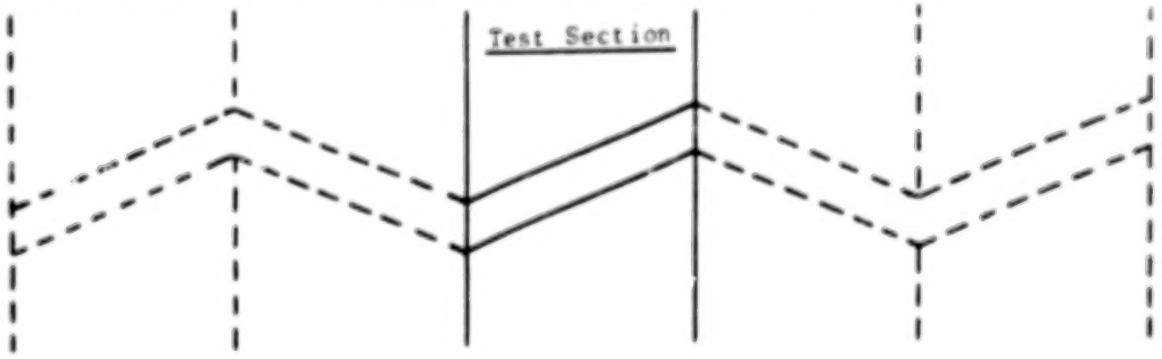

The analysis proceeds by assuming that the bounded wing and all image wings are small compared to the test section and each may be approximated by a single vortex at its quarter chord line. The analysis for calculating the change in incidence angle due to this array of vortices is the method of images. Because the wing is skewed, the classical image system which extends above and below the test section to infinity and which represents the tunnel floor and ceiling for an airfoil in bounded flow, must be extended to include an infinite spanwise image system to the right and the left of the test section. This system is shown in Fig. 69 together with the arrangement for assigning direct and inverted vortex systems and also the arrangement for assigning positive and negative sweep angles to represent the kinked wing system. There are three effects that are represented by this image system: first, the missing downward curvature (induced vertical velocity) of the airstream that is realized in free-air and reduced due to the ceiling and floor boundaries; second and thirdly, the induced longitudinal and lateral velocities which are induced by the tunnel walls. The vertical velocity effect is the most significant; it induces an upwash and, hence, a local incidence angle change, $\Delta\alpha$. The longitudinal and lateral velocity effects are much smaller and are ignored for presentation. This is a modification to Ref. 12, where the longitudinal velocity is presented as more significant.

Application of the Biot-Savart law to determine the total velocity of one bound image vortex at the 50 percent chord station of the test wing gives rise to the following equation:

$$q = \left\{ \frac{\Gamma \sec \Lambda}{4\pi a \left[(n \sin \Lambda + c/4a)^2 + m^2 (h/a)^2 \right]^{1/2}} \right\} x$$

$$\left\{ \frac{n \cos^2 \Lambda - y/a + 1/2}{\left[\left[(y/a - 1/2) \tan \Lambda + c/4a \right]^2 + \left[-y/a + 1/2 + n + (c/4a) \sin \Lambda \right]^2 + m^2 (h/a)^2 \right]^{1/2}} \right. \tag{26}$$

$$\left. - \frac{n \cos^2 \Lambda - y/a - 1/2}{\left[\left[(y/a + 1/2) \tan \Lambda + c/4a \right]^2 + \left[y/a + 1/2 - n + (c/4a) \sin \Lambda \right]^2 + m^2 (h/a)^2 \right]^{1/2}} \right\}$$

Equation (26) for the effect of a bound vortex in skewed flow can be developed from the unskewed case presented in standard aerodynamic texts such as Ref. 20 (Eq. (11.10) p.219). It is evaluated at the semi-chord in accordance with standard practice, representing the average effect of the induced flow field over the airfoil chord. This is a modification to the method of Ref. 12 where the induced flow is evaluated at the wing quarter chord. If the quarter chord is used, the summation of the induced flow effects from all the image vortices is zero. Classical, unswept theory also predicts no effect when evaluated at the quarter chord. The semi-chord should be used as in classical theory for the reason noted above.

Resolution of the total velocity, q, into its vertical component is achieved by multiplying by the direction cosine:

$$\zeta = \frac{n \sin\Lambda + c/4a}{\left[(n \sin\Lambda - c/4a)^2 + m^2(h/a)^2\right]^{1/2}} \tag{27}$$

Accordingly,

$$w = \zeta q \tag{28}$$

The circulation, Γ, in Eq. (26) is related to the wing lift coefficient, C_L, by:

$$\Gamma = \frac{1}{2} \frac{c}{\cos\Lambda} V_0 C_L \tag{29}$$

Therefore, combining Eqs. (26) through (29) and multiplying by the appropriate sign for the assigned circulation direction, the equation for the induced flow in the tunnel, w, ratioed to the free stream velocity becomes:

$$\frac{w}{V} = \left[\frac{(-1)^m}{8\pi a}\ \frac{C}{\cos^2\Lambda}\right]\left\{\frac{n\sin\Lambda + C/4a}{\left[(n\sin\Lambda - C/4a) + m^2(h/a)^2\right]}\right\} \times$$

$$\left\{\frac{n\cos^2\Lambda - y/a + 1/2}{\left[\left[(y/a - \frac{1}{2})\tan\Lambda + C/4a\right]^2 + \left[-y/a + \frac{1}{2} + n + (C/4a)\sin\Lambda\right]^2 + m^2(h/a)^2\right]^{\frac{1}{2}}}\right. \tag{30}$$

$$\left. - \frac{n\cos^2\Lambda - y/a - \frac{1}{2}}{\left[\left[(y/a + \frac{1}{2})\tan\Lambda + C/4a\right]^2 + \left[y/a + \frac{1}{2} - n + (C/4a)\sin\Lambda\right]^2 + m^2(h/a)^2\right]^{\frac{1}{2}}}\right\} C_L$$

$$w/V = K_1 C_L = \Delta\alpha \tag{31}$$

But w/V is the change in incidence angle, $\Delta\alpha$, due to the tunnel boundaries, and

$$\Delta\alpha \text{ (degrees)} = 57.3\ \frac{w}{V}$$

When summed over the entire lattice, the resulting w is negative, which is an upwash. Therefore, the corrected or free stream incidence angle becomes, in the plane of the free stream:

$$\alpha_{air} = \alpha_{tunnel} + \Delta\alpha \tag{32}$$

$$\alpha_{air} = \alpha_{tunnel} + K_1 C_L$$

or in the plane normal to span:

$$\alpha_{n_{air}} = \alpha_{n_{tunnel}} + \frac{K_1 C_L}{\cos\Lambda} \tag{33}$$

REFERENCES

1. Halfman, R. L., H. C. Johnson, and S. M. Haley: Evaluation of High-Angle-of-Attack Aerodynamic-Derivative Data and Stall Flutter Prediction Techniques. NACA Technical Note TN2533, November 1951.

2. Carta, F. O.: Experimental Investigation of the Unsteady Aerodynamic Characteristics of an NACA 0012 Airfoil. United Aircraft Research Laboratories Report M-1283-1, August 1960.

3. Carta, F. O., G. L. Commerford, R. G. Carlson, and R. H. Blackwell: Investigation of Airfoil Dynamic Stall and its Influence on Helicopter Control Loads. USAAMRDL Technical Report 72-51, U. S. Army Air Mobility Research and Development Laboratory, Fort Eustis, Virginia, September 1972.

4. Liiva, J., F. J. Davenport, L. Gray, and I. C. Walton: Two-Dimensional Tests of Airfoils Oscillating Near Stall. Vol. I, Summary and Evaluation of Results. USAAVLABS Technical Report 63-13A, Vol. II, Data Report. USAAVLABS Technical Report 63-13B, U. S. Army Aviation Material Laboratories, Fort Eustis, Virginia, April 1968.

5. Jepson, W. D: Two Dimensional Test of Four Airfoil Configurations with an Aspect Ratio of 7.5 and a 16 Inch Chord up to a Mach Number of 1.1. Sikorsky Engineering Report SER-50977, April 5, 1977, performed under Contract No. N60921-73-C-0057.

6. Carta, F. O., and A. O. St. Hilaire: An Experimental Study of Sweep Effects on the Unsteady Aerodynamics of a Pitching Airfoil. United Technologies Research Center Report R76-411931, March 1976.

7. St. Hilaire, A. O.: The Segmented Gaussian Quadrature and its Application for Optimizing Airfoil Instrumentation Arrays. United Technologies Research Center Report UTRC76-150, October 5, 1976.

8. McCroskey, W. J., and E.J. Durbin: Flow Angle and Shear Stress Measurements Using Heated Films and Wires. Trans. ASME, Journal of Basic Engineering, Vol. 94, No. 1, March 1972, pp. 46-52.

9. Bellinger, E. D., W. P. Patrick, L. E. Greenwald, and A. J. Landgrebe: Experimental Investigation of the Effects of Helicopter Rotor Design Parameters on Forward Flight Stall Characteristcs. Report USAAMRDL-TR-74-1, April 1974.

10. Phillipe, J. J. and M. Sagner: Calcul et Mesure des Forces Aérodynamiques sur un Profil Oscillant avec et sans Décrochage. Presenteé à la réunion du Groupe Dynamique des Fluides de l'AGARD. Marseilles, 1972. (O.N.E.R.A. Report No. T.P. 132, 1972).

11. Allen, H. J. and W. G. Vincenti: Wall Interference In a Two-Dimensional Flow Wind Tunnel, with Consideration of the Effect of Compressibility. NACA Report 782, 1944.

12. Dannenberg, R. E.: Measurements of Section Characteristics of a 45^{o} Swept Wing Spanning a Rectangular Low-Speed Tunnel as Affected by the Tunnel Walls. NACA TN 2160, August 1950.

13. Carr, L. W., K. W. McAlister, and W. J. McCroskey: Analysis of the Development of Dynamic Stall Based on Oscillating Airfoil Experiments. NASA Technical Note, TN D-8382, January 1977.

14. McAlister, K. W., L. W. Carr and W. J. McCroskey: Dynamic Stall Experiments on the NACA 0012 Airfoil. NASA Technical Paper 1100. January 1978.

15. St. Hilaire, A. O.and F. O. Carta: The Influence of Sweep on the Aerodynamic Loading of an Oscillating NACA 0012 Airfoil. Vol. II - Data Report. NASA CR-14[illegible]350, 1979.

16. Carta, F. O. and C. F. Niebanck: Prediction of Rotor Instability at High Forward Speeds, Vol. III, Stall Flutter. USAAVLABS Technical Report 68-18C, U.S. Army Aviation Material Laboratories, Fort Eustis, Virginia, February 1969.

17. Roos, F. W. and D. W. Riddle: Measurements of Surface-Pressure and Wake-Flow Fluctuations in the Flow Field of a Whitcomb Supercritical Airfoil. NASA TN D-8443, August 1977.

18. Carlson, L. A.: TRANDES: A Fortran Program for Transonic Airfoil Analysis or Design. NASA CR-2821, June 1977.

19. Levy, L. L.,Jr.: Experimental and Computational Steady and Unsteady Transonic Flows About a Thick Airfoil. AIAA Journal, Vol. 16, No. 6, June 1978, pp 569-572.

20. Pope, A.: Basic Wing and Airfoil Theory, 1st Ed. McGraw-Hill Book Company, New York, 1951.

TABLE I

NACA 0012 AIRFOIL COORDINATES

x/c	y/c Upper
0	0
.005	.0121
.010	.0170
.020	.0235
.040	.0321
.080	.0429
.120	.0497
.180	.0559
.250	.0592
.350	.0593
.500	.0528
.600	.0455
.700	.0365
.800	.0261
.900	.0144
.950	.0080
1.000	.0013

y/c lower = -y/c upper
Thickness distribution = 2 (y/c upper)

TABLE II

PRESSURE AND HOT FILM MEASUREMENT STATIONS

(All coordinates in percent chord. For non-metric section, first coordinate aft of leading edge, second coordinate spanwise from reference line. For metric section, chordwise coordinate only).

Non-Metric Section, Steady, and Unsteady

Suction Surface		
Pressures		Hot Films
Reference Line or Chordwise Array	L.E. Region	Chordwise
0.4, 0.0	1.0, 3.5	2.1, 10.0
2.0, 0.0	First Swept Array	7.4, 10.0
4.5, 0.0	0.4, 26.0	14.8, 10.0
7.3, 0.0	4.5, 23.6	25.0, 10.0
9.8, 0.0	14.8, 17.7	45.4, 10.0
11.4, 0.0	(45.4, 0.0)*	85.1, 10.0
14.8, 0.0	Second Swept Array	First Swept Array
25.8, 0.0	0.4, 55.8	2.1, 35.0
45.4, 0.0	4.5, 53.4	25.0, 21.8
66.4, 0.0	25.8, 40.5	(45.4, 10.0)*
85.1, 0.0	(97.0, 0.0)*	Second Swept Array
97.0, 0.0		2.1, 57.9
		41.8, 35.0
		(85.1, 10.0)*

( )* = Location also in chordwise array

Pressure Surface, Pressures
0.5, 0.0
1.5, 0.0
5.2, 0.0
18.5, 0.0
39.2, 0.0
62.7, 0.0
83.4, 0.0
96.7, 0.0

Metric Section, Steady Only

Suction Surface
0.0
1.0
2.0
4.0
6.0
10.0
12.0
12.5
15.0
20.0
25.0
30.0
40.0
50.0
60.0
70.0
80.0
81.0
90.0

Pressure Surface
1.0
4.0
6.0
10.0
20.0
35.0
50.0
70.0
90.0

TABLE III

UNSTEADY TEST MATRIX FOR NACA0012 AIRFOIL

Airfoil	Λ (deg)	$\bar{\alpha}$ (deg)	α_M (deg)	M_∞	M_c	f (cps) 4	5.33	6	8	10	10.67
NACA0012	0	8	0	.3	.3	X			X	X	
			"	.4	.4	X			X	X	
			4	.3	.3	X			X	X	
			"	.4	.4	X			X	X	
			12	.3	.3	X			X	X	
			"	.4	.4	X			X	X	
			15	.3	.3	X			X	X	
			"	.4	.4	X			X	X	
		10	0	.3	.3	X			X	X	
			"	.4	.4	X			X	X	
			9	.3	.3	X			X	X	
			"	.4	.4	X			X	X	
			12	.3	.3	X			X	X	
			"	.4	.4	X			X	X	
NACA0012	30	8	0	.346	.3	X		X	X	X	
			"	.462	.4	X	X		X	X	X
			9	.346	.3	X		X	X	X	
			"	.462	.4	X	X		X	X	X
			12	.346	.3	X	X	X	X	X	
			"	.462	.4	X	X		X	X	X
			15	.346	.3	X		X	X	X	
			"	.462	.4	X	X		X	X	X
		10	9	.346	.3	X		X	X	X	
			"	.462	.4	X	X		X	X	X
			12	.346	.3	X		X	X	X	
			"	.462	.4	X	X		X	X	X
			15	.346	.3	X		X	X	X	
			"	.462	.4	X	X		X	X	X

Additional Test Points:						f (cps) 2.5	3.75	5	6.25	
NACA0012	30	10	15	.104	.09					

TABLE IV

NOMINAL VALUES OF k_c FOR BASIC TEST PROGRAM

M_c = / f (cps)	0.3	0.4	
	VALUES OF k_c		
4	.051	.038	←
5.33	.067	.051	
6	.076		
8	.102	.076	←
10	.127	.095	←
10.67		.102	

Notes:

1. All values displayed were run at least once.
2. Horizontal arrows on right column denote nominal values used for unswept runs.
3. Boxed numbers denote nominal values used for swept runs.
4. Diagonal arrows indicate matched values of k_c.

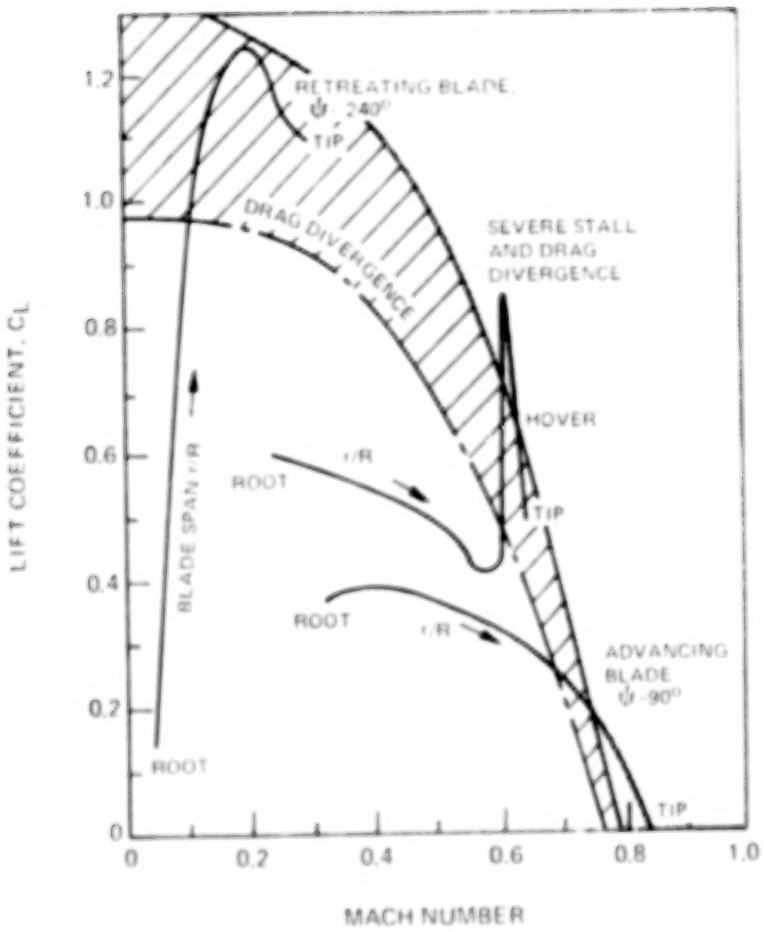

Figure 1 Operating Envelope

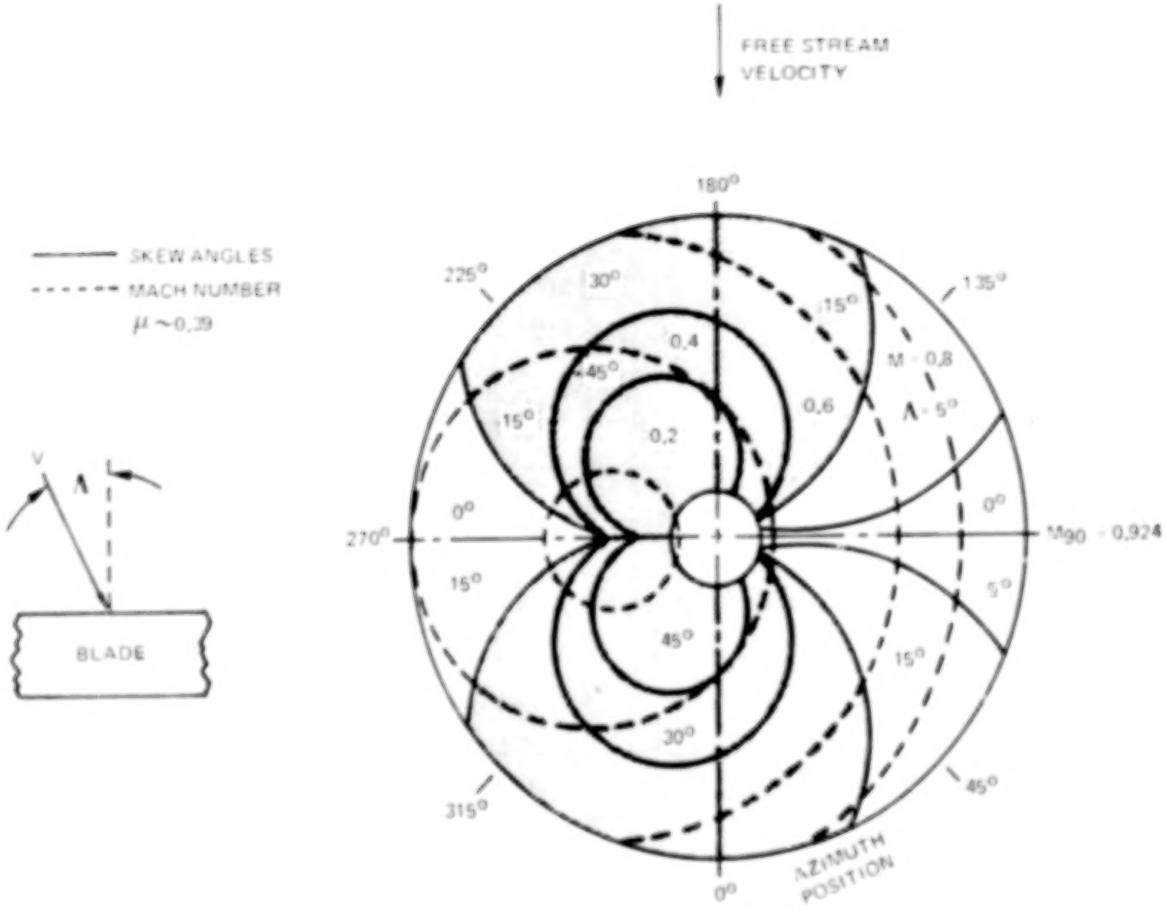

Figure 2 Contours of Sweep Angle and Mach Number

BLANK

PAGE

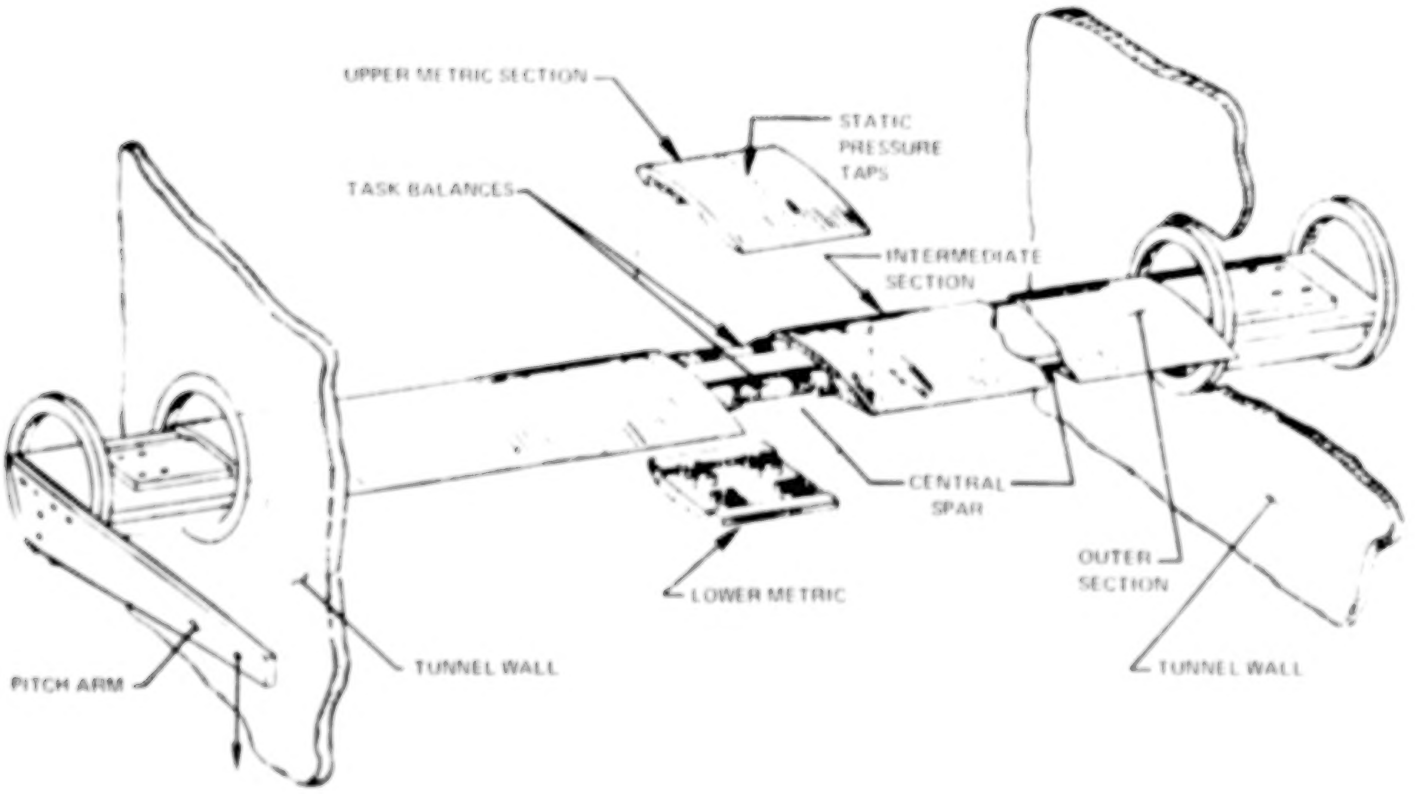

Figure 3 Spar and Shell Assembly with Balance

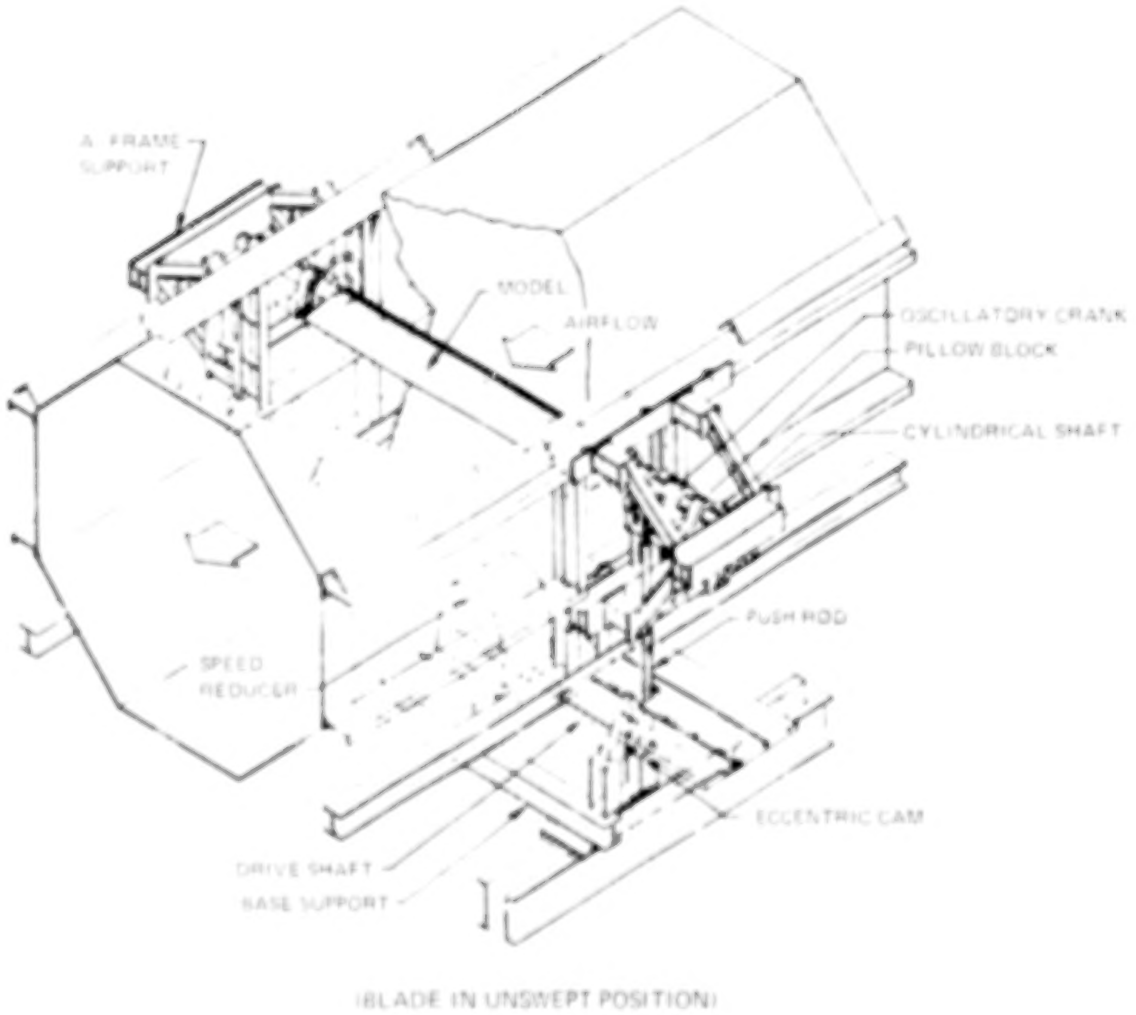

Figure 4 UTRC Main Wind Tunnel Oscillatory Model System

BLANK

PAGE

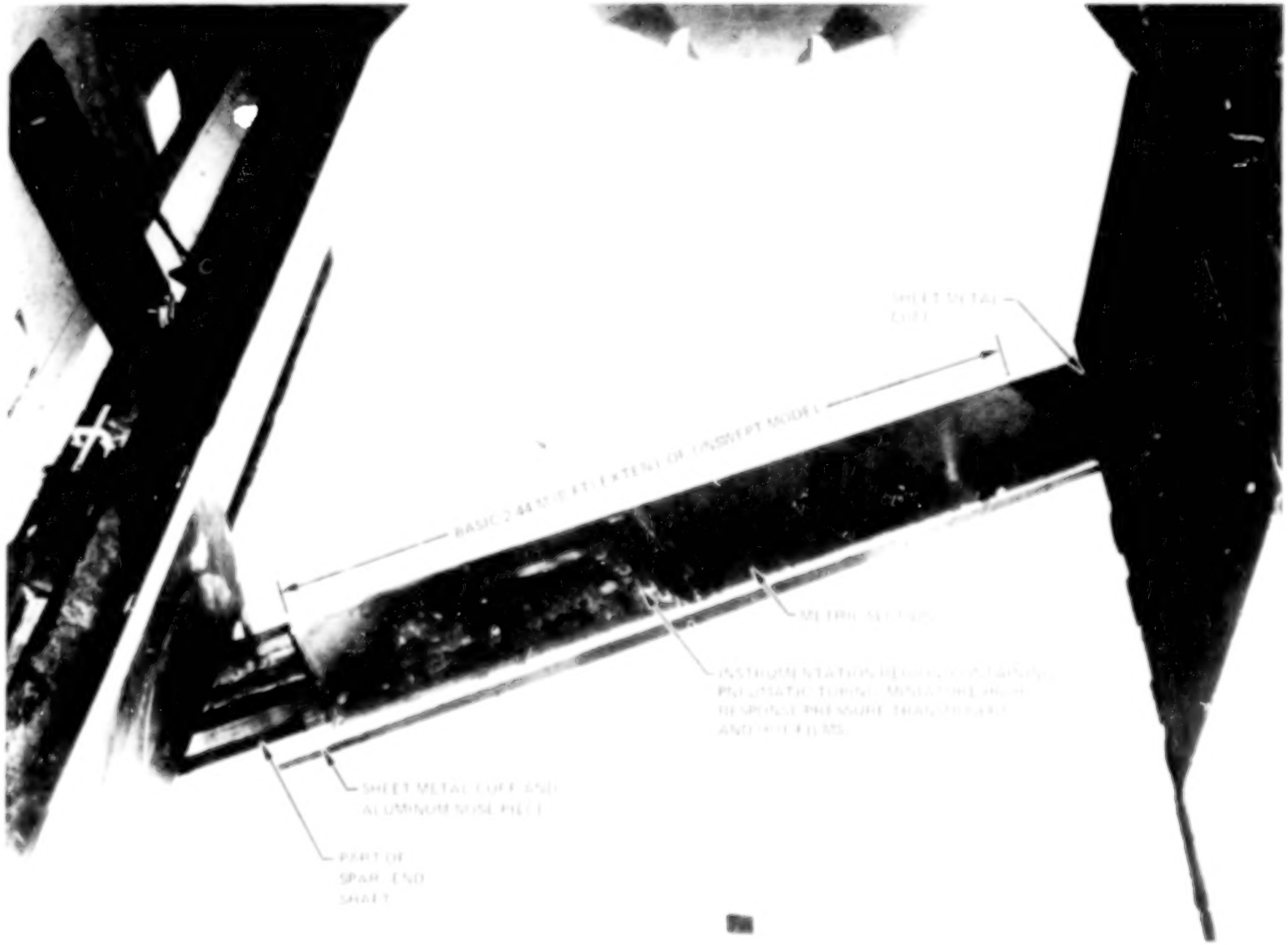

(DOWNSTREAM VIEW WITHOUT PART-SPAN SUPPORTS)

Figure 5 Swept Tunnel – Spanning Model

Figure 6 UTRC Installation, $\Lambda = 30^{\circ}$

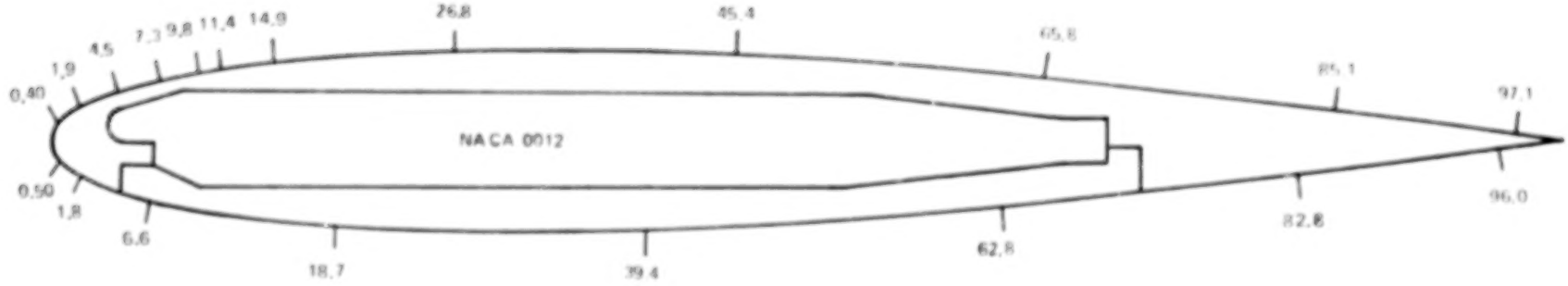

TIC MARKS AND NUMBERS INDICATE PRESSURE MEASURING STATIONS ALONG REFERENCE LINE, PERCENT CHORD

Figure 7 Airfoil Cross Section Showing Chordwise Measuring Stations Along Reference Line

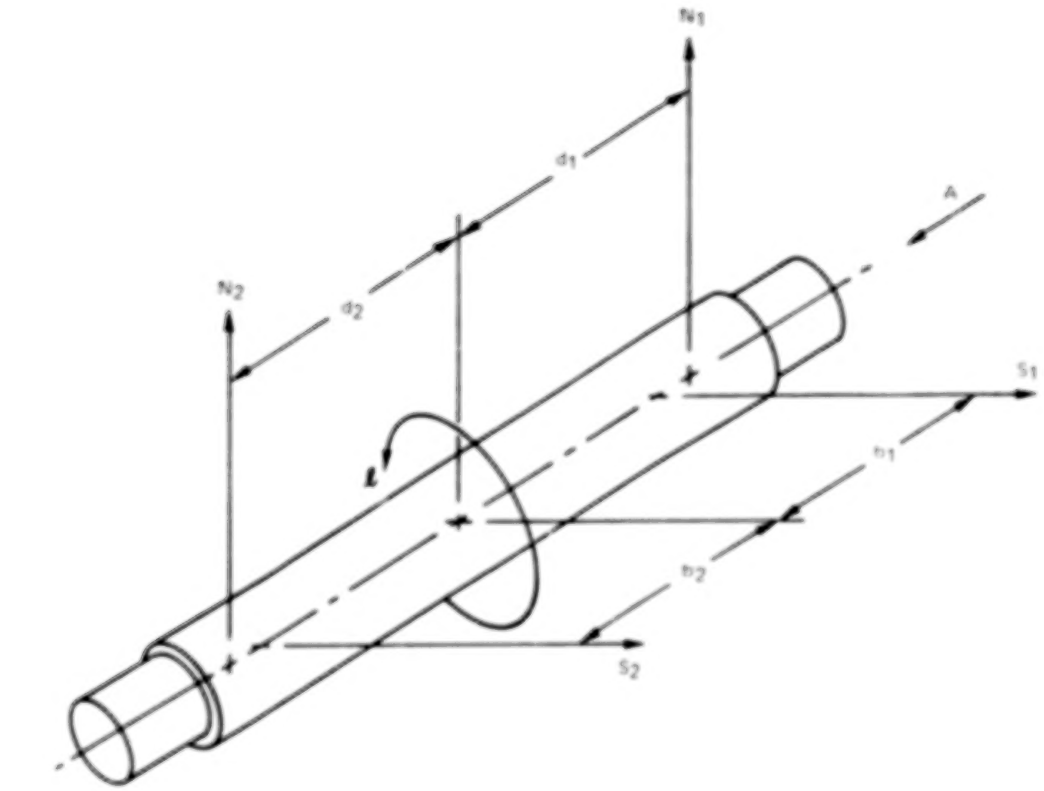

a) SINGLE ELEMENT SCHEMATIC

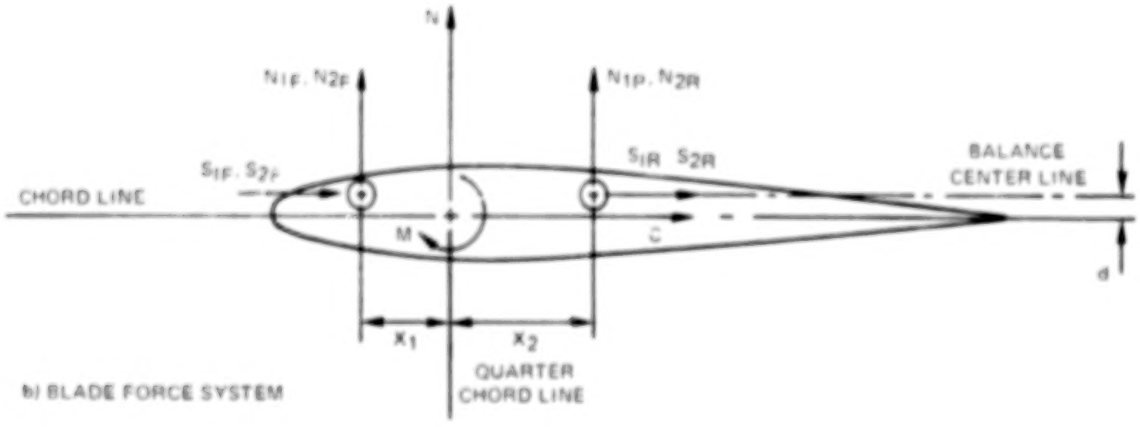

b) BLADE FORCE SYSTEM

Figure 8 Balance Schematic

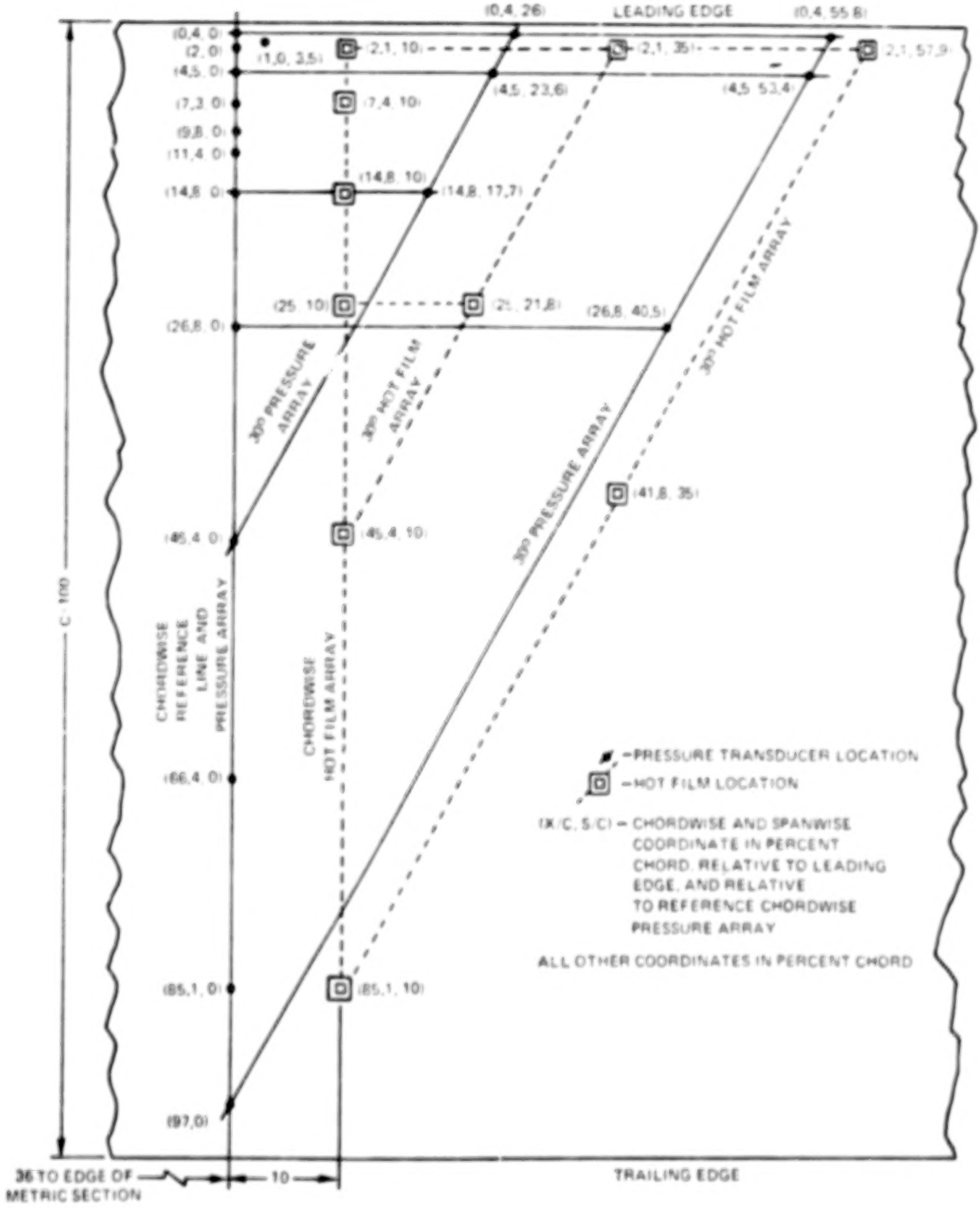

Figure 9 Pressure Transducer and Hot Film Layouts on Airfoil Suction Surface

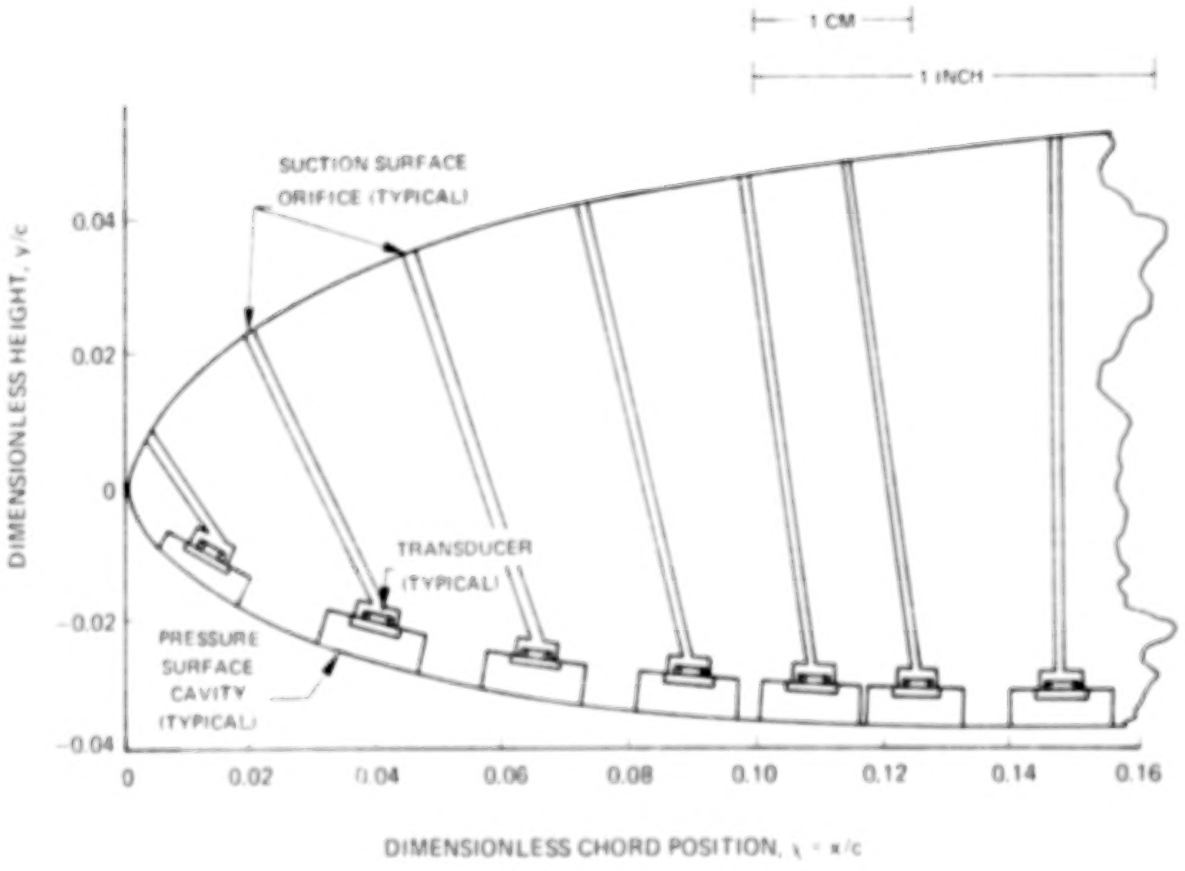

Figure 10 Section View Showing Suction Surface Instrumentation (Schematic)

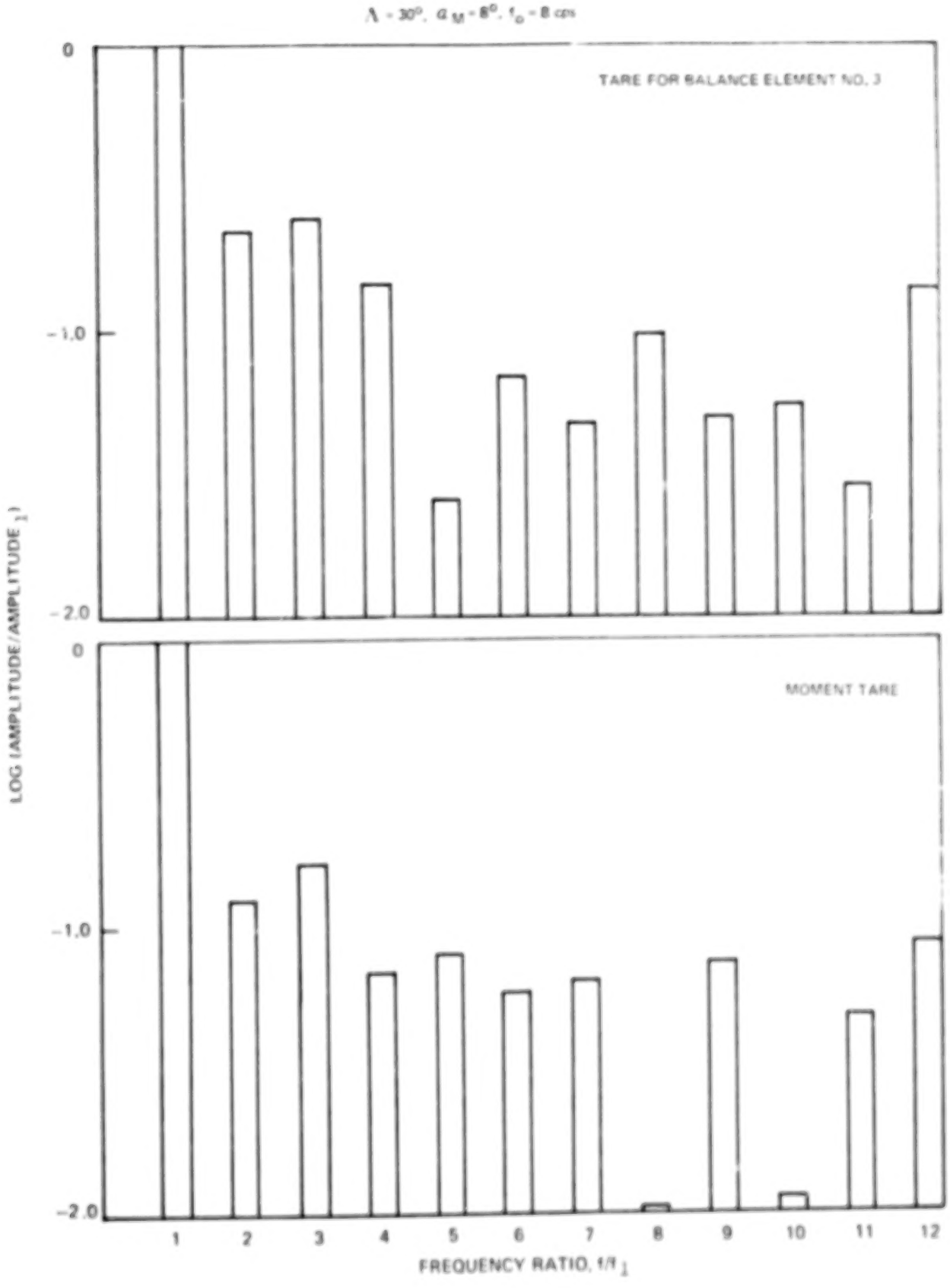

Figure 11 Typical Harmonic Content of No–Flow Balance Response

Figure 12 Block Diagram for Data Acquisition and Digitizing

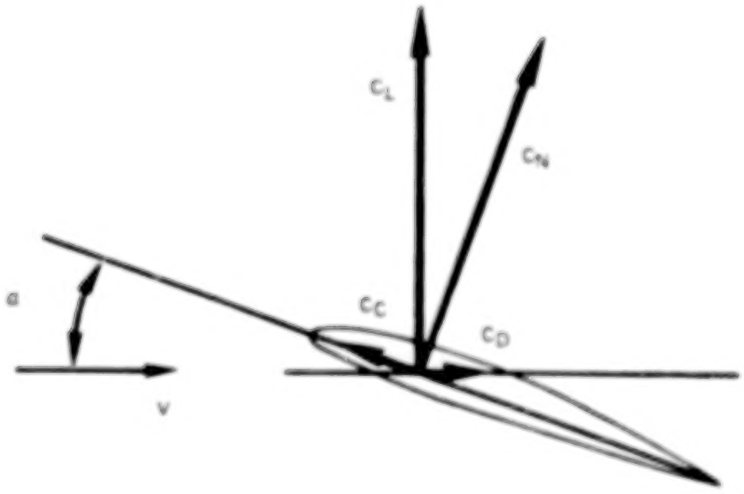

$$C_D = C_N \sin \alpha - C_C \cos \alpha$$

$$C_L = C_N \cos \alpha + C_C \sin \alpha$$

Figure 13 Airfoil Force Schematic

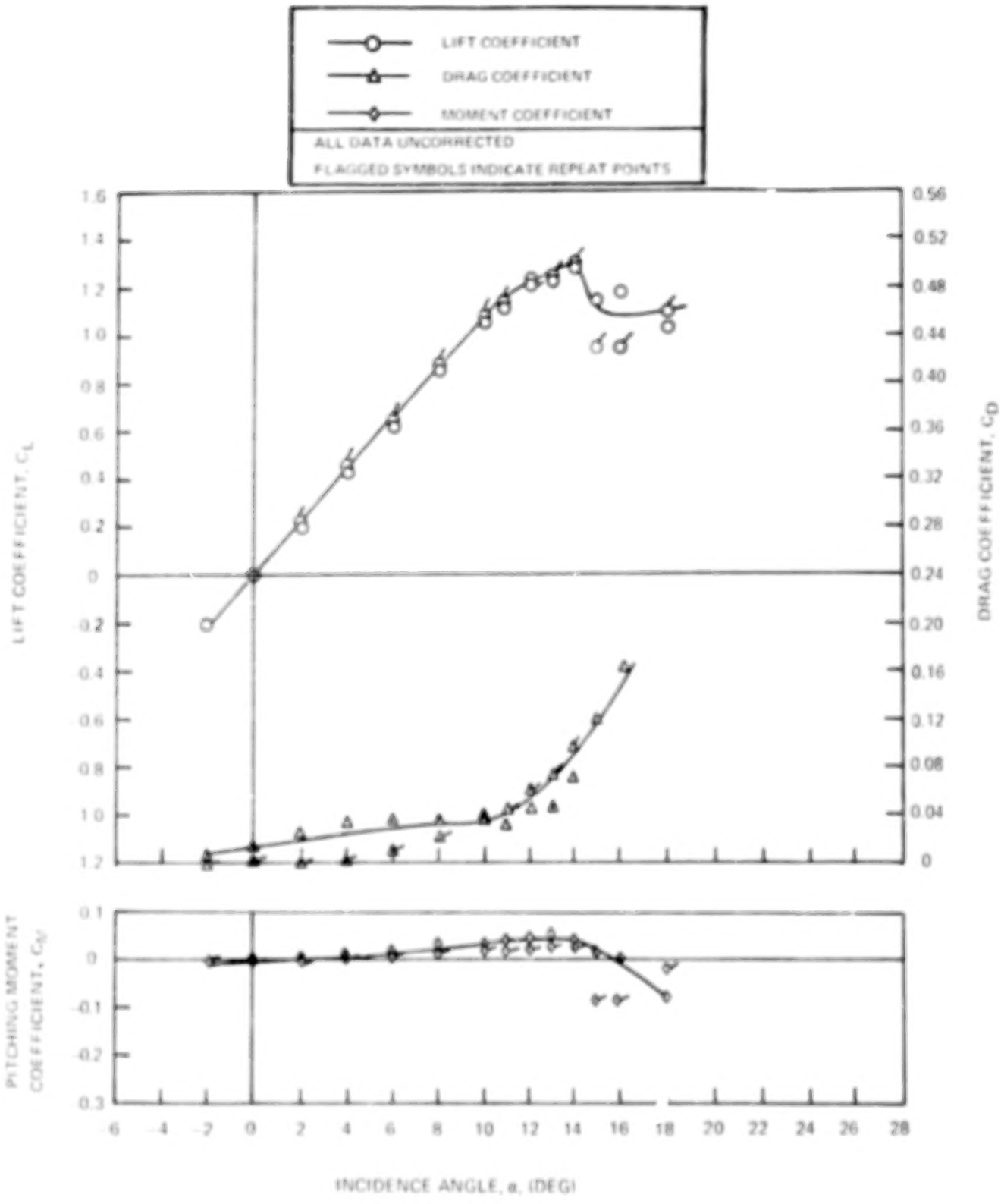

Figure 14 Steady–State Lift, Drag, and Pitching Moment Coefficients for the NACA 0012 Airfoil at $M_c = 0.3$ and $\Lambda = 0$ Deg.

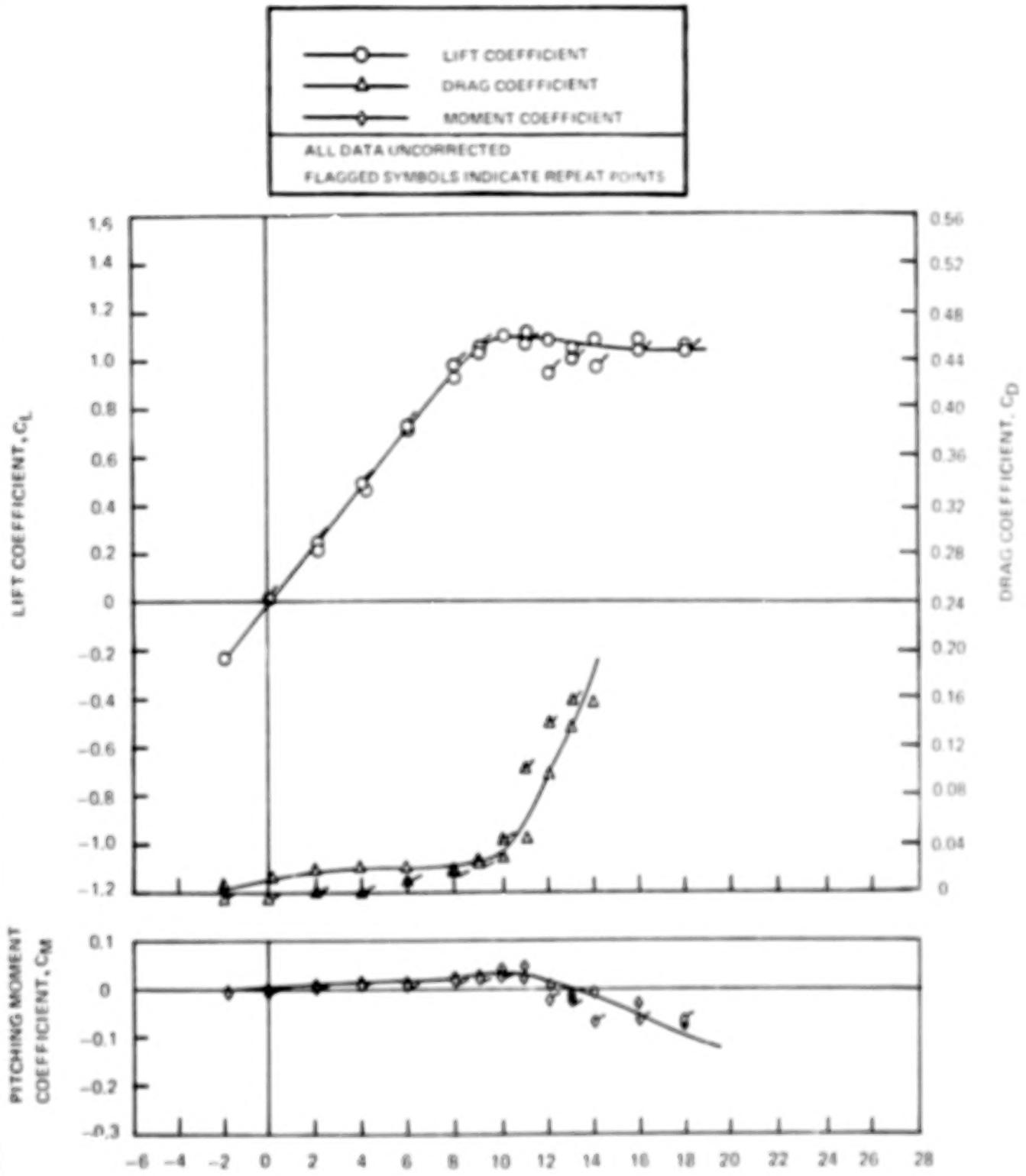

Figure 15 Steady–State Lift, Drag, and Pitching Moment Coefficients for the NACA 0012 Airfoil at M_c = 0.4 and Λ = 0 Deg.

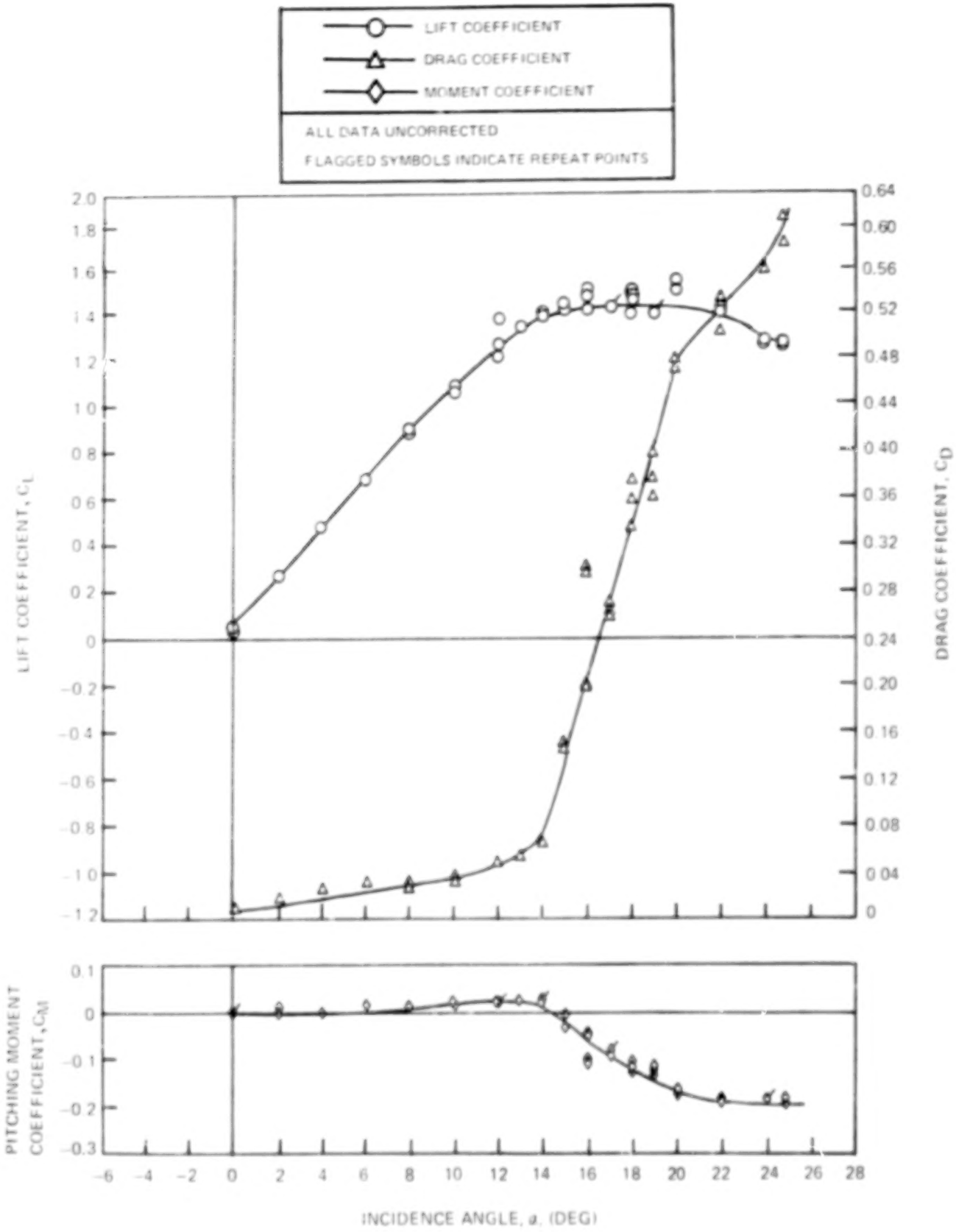

Figure 16 Steady–State Lift, Drag, and Pitching Moment Coefficients for the NACA 0012 Airfoil at $M_c = 0.3$ and $\Lambda = 30$ Deg.

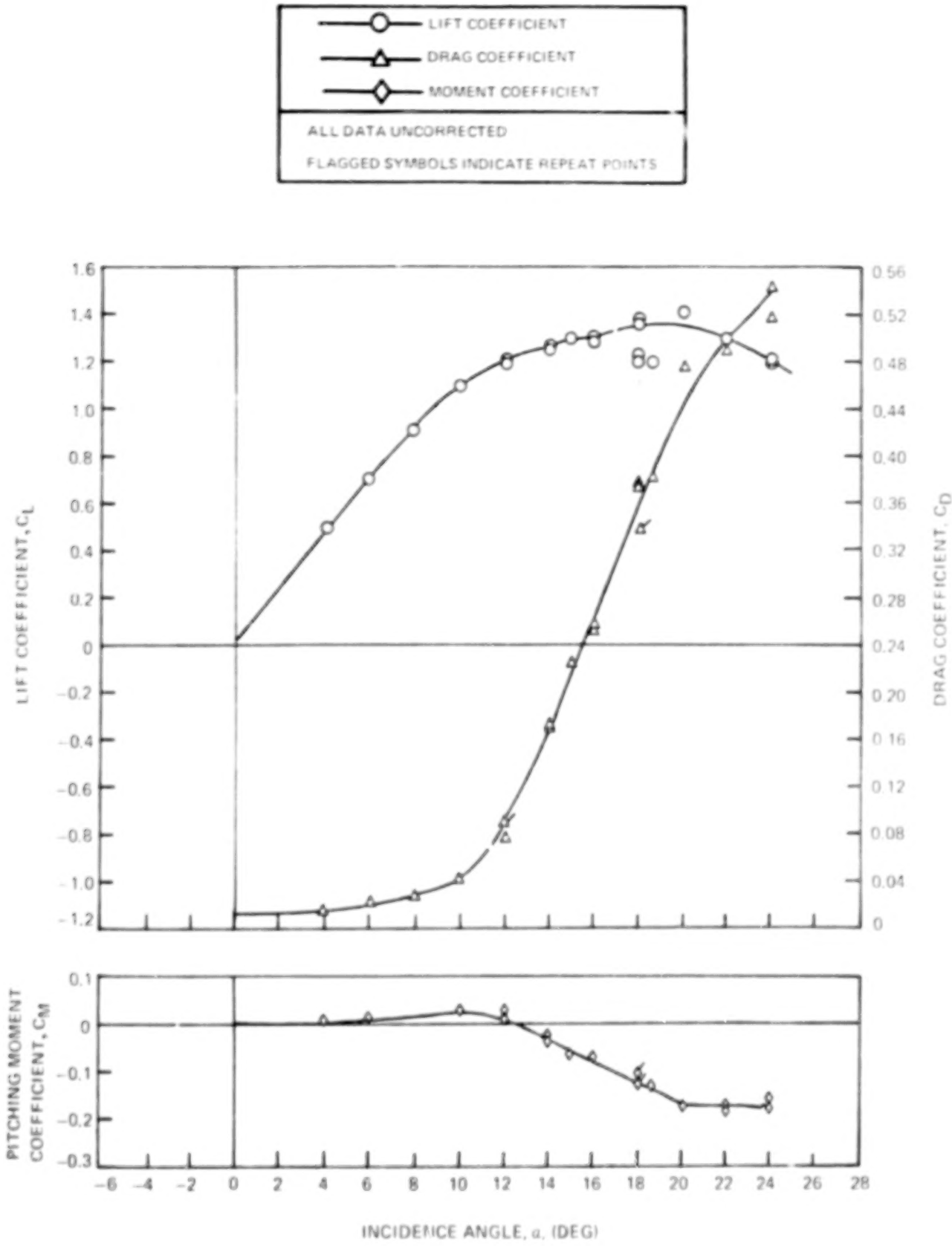

Figure 17 Steady–State Lift, Drag, and Pitching Moment Coefficients for the NACA 0012 Airfoil at $M_c = 0.4$ and $\Lambda = 30$ Deg.

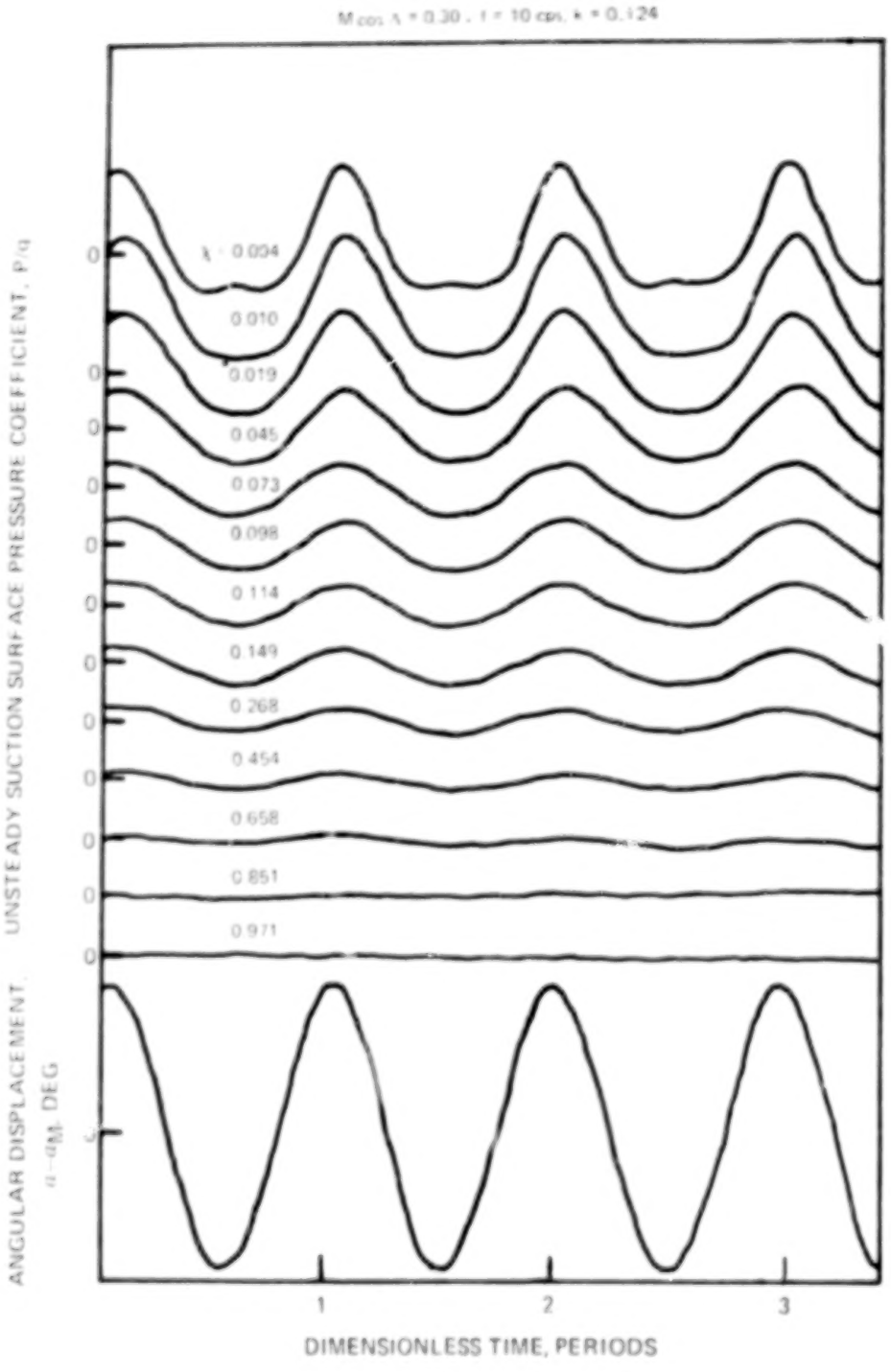

Figure 18 Unsteady Pressure Time History for Potential Flow, $\alpha_M = 0^o$

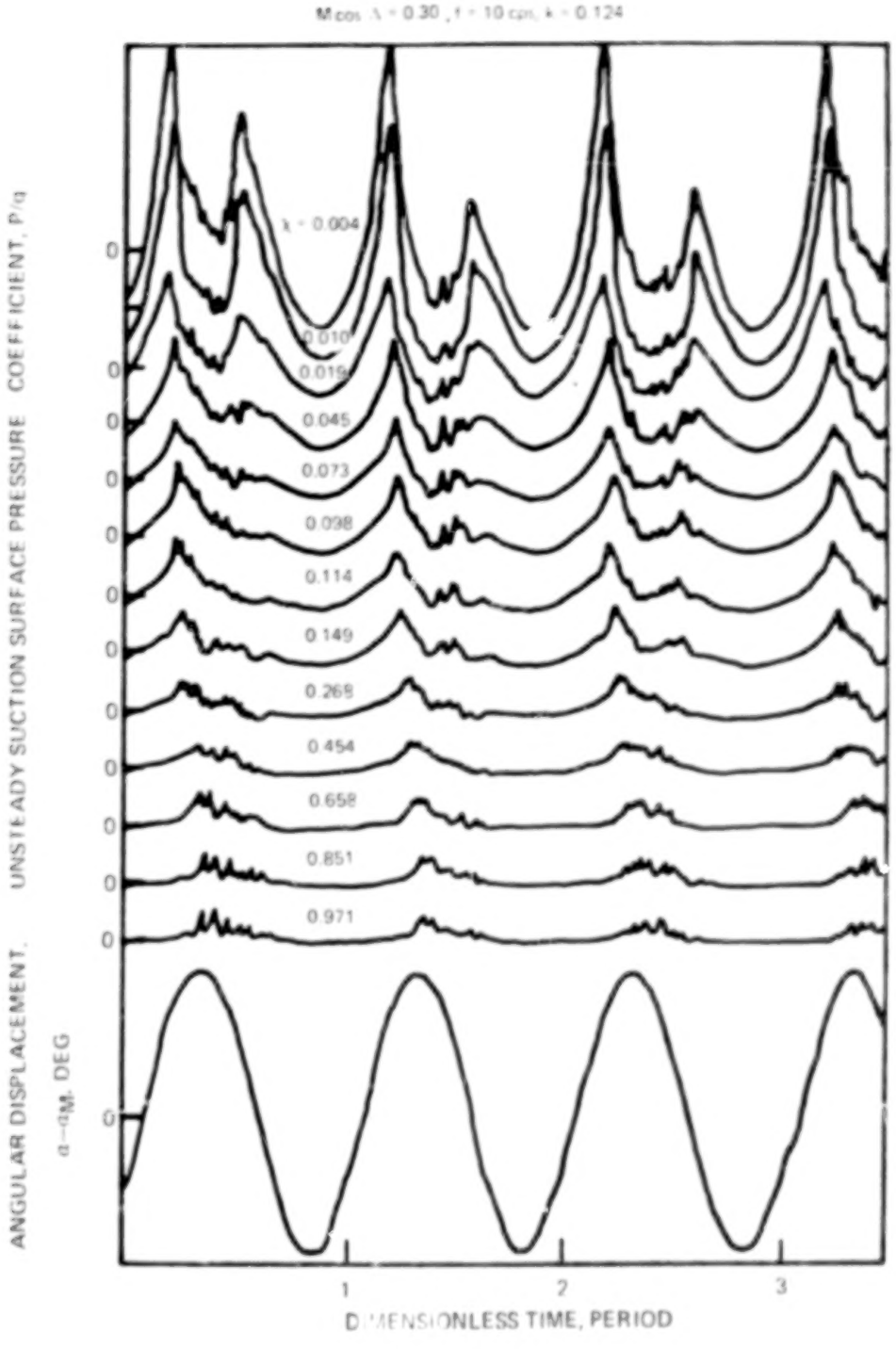

Figure 19 Unsteady Pressure Time History for Stalled Flow Penetration, $\alpha_M = 12^o$

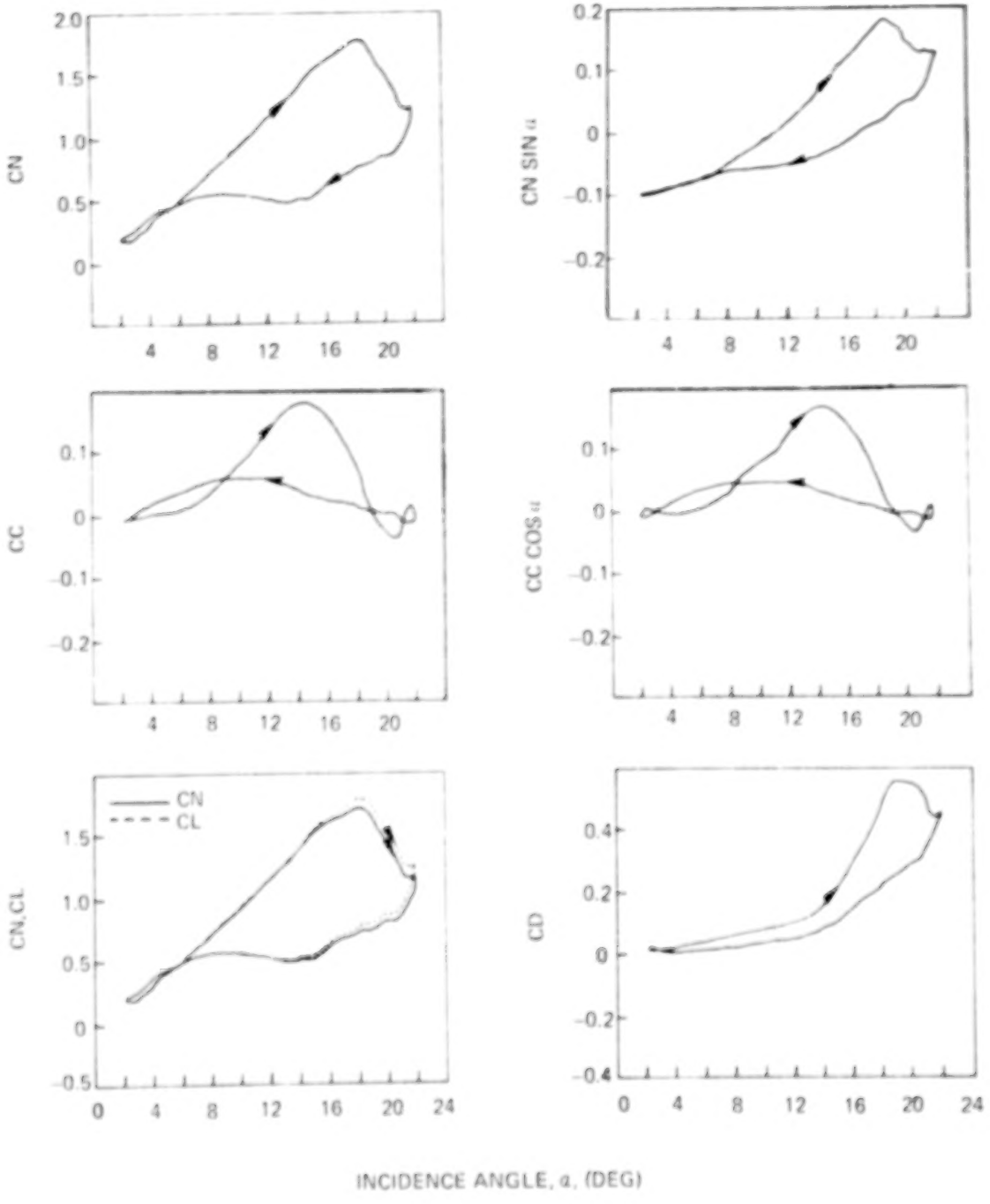

Figure 20 Contribution of C_N and C_C Components to the Pressure Drag Component, C_D, for Λ = 0 Deg, $\bar{\alpha}$ = 10 Deg, M_c = 0.40, α_M = 12 Deg, and f = 10 cps

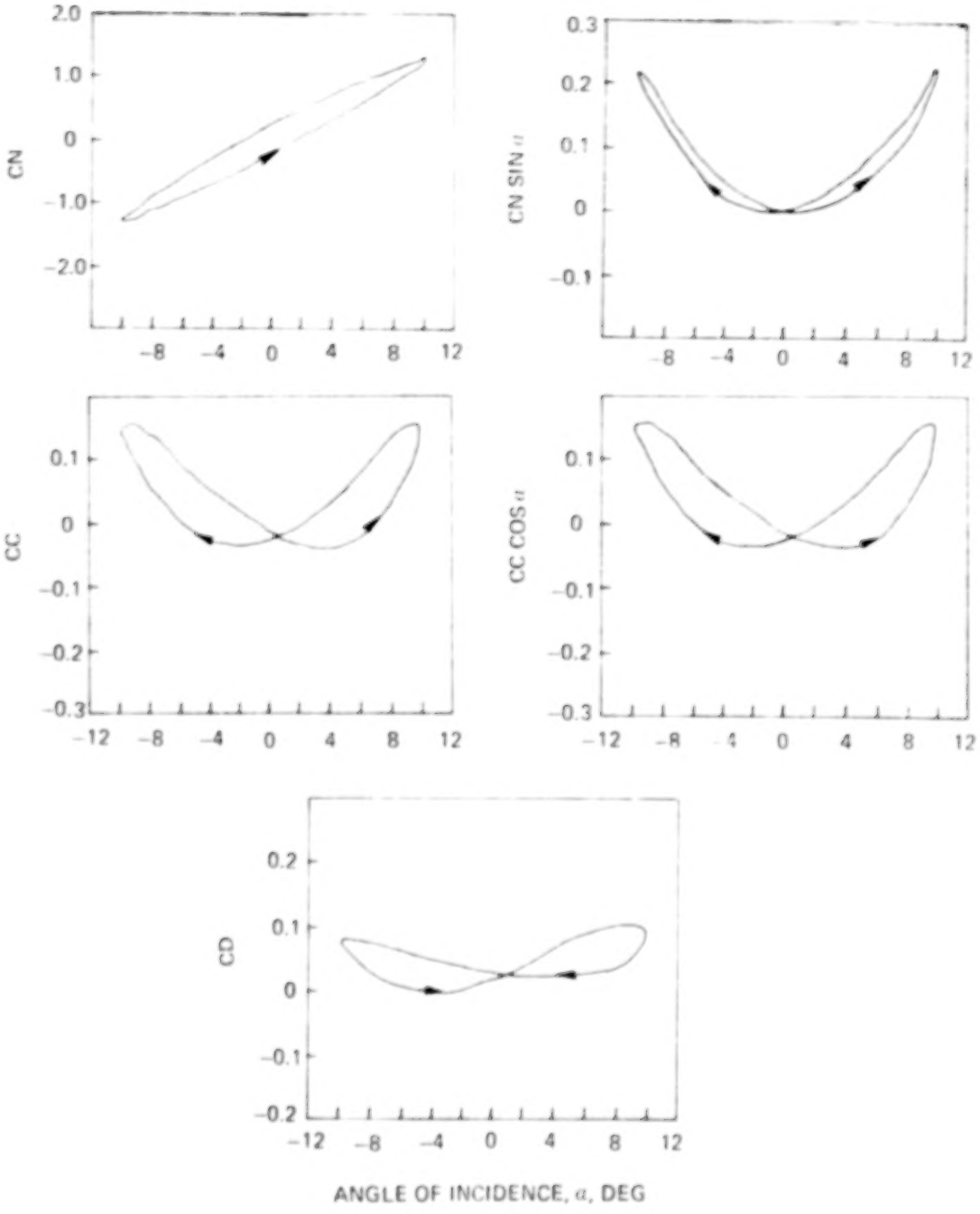

Figure 21 Contribution of C_N and C_C Components to the Pressure Drag Component, C_D, for Λ = 0 Deg, $\bar{\alpha}$ =10 Deg, M_c = 0.40, α_M = 0 Deg, and f = 10 cps

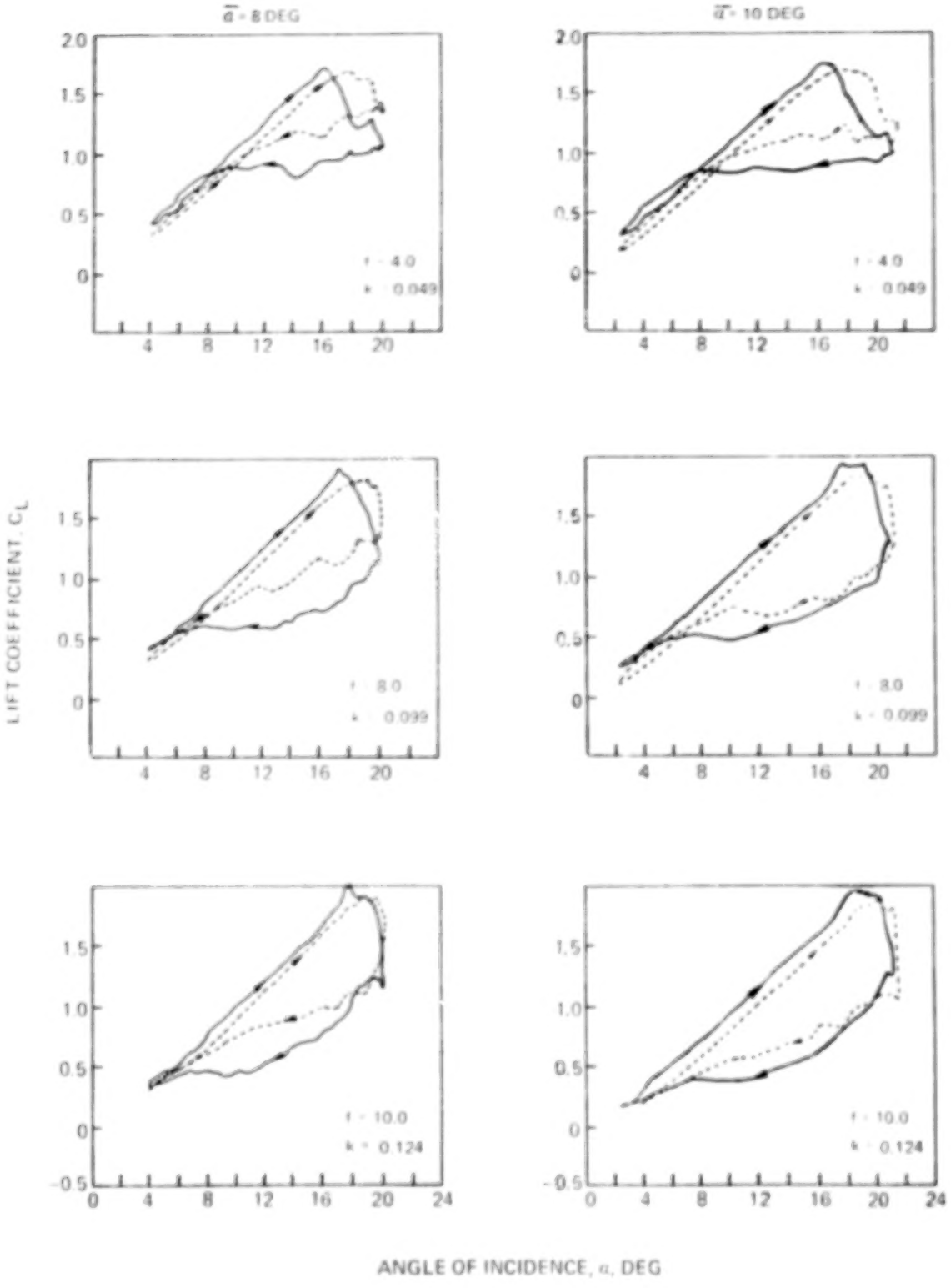

Figure 22 Effect of Sweep, Amplitude and Frequency on the Induced Lift Response for M_c = 0.30 and α_M = 12 Deg, —— Λ = 0 Deg; - - - Λ = 30 Deg

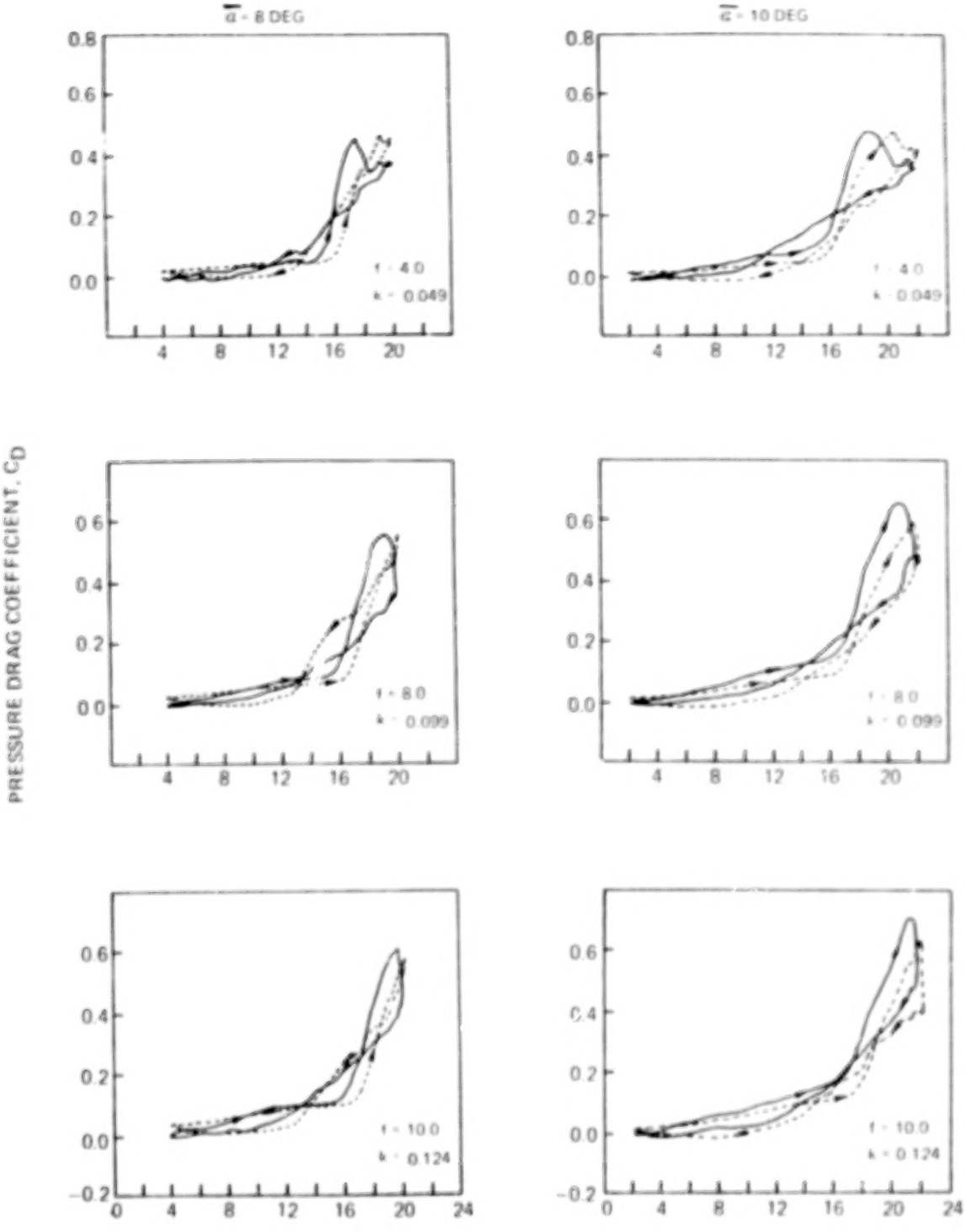

Figure 23 Effect of Sweep, Amplitude and Frequency on the Induced Pressure Drag Response for M_c = 0.30 and α_M = 12 Deg, —— Λ = 0 Deg; - - - Λ = 30 Deg

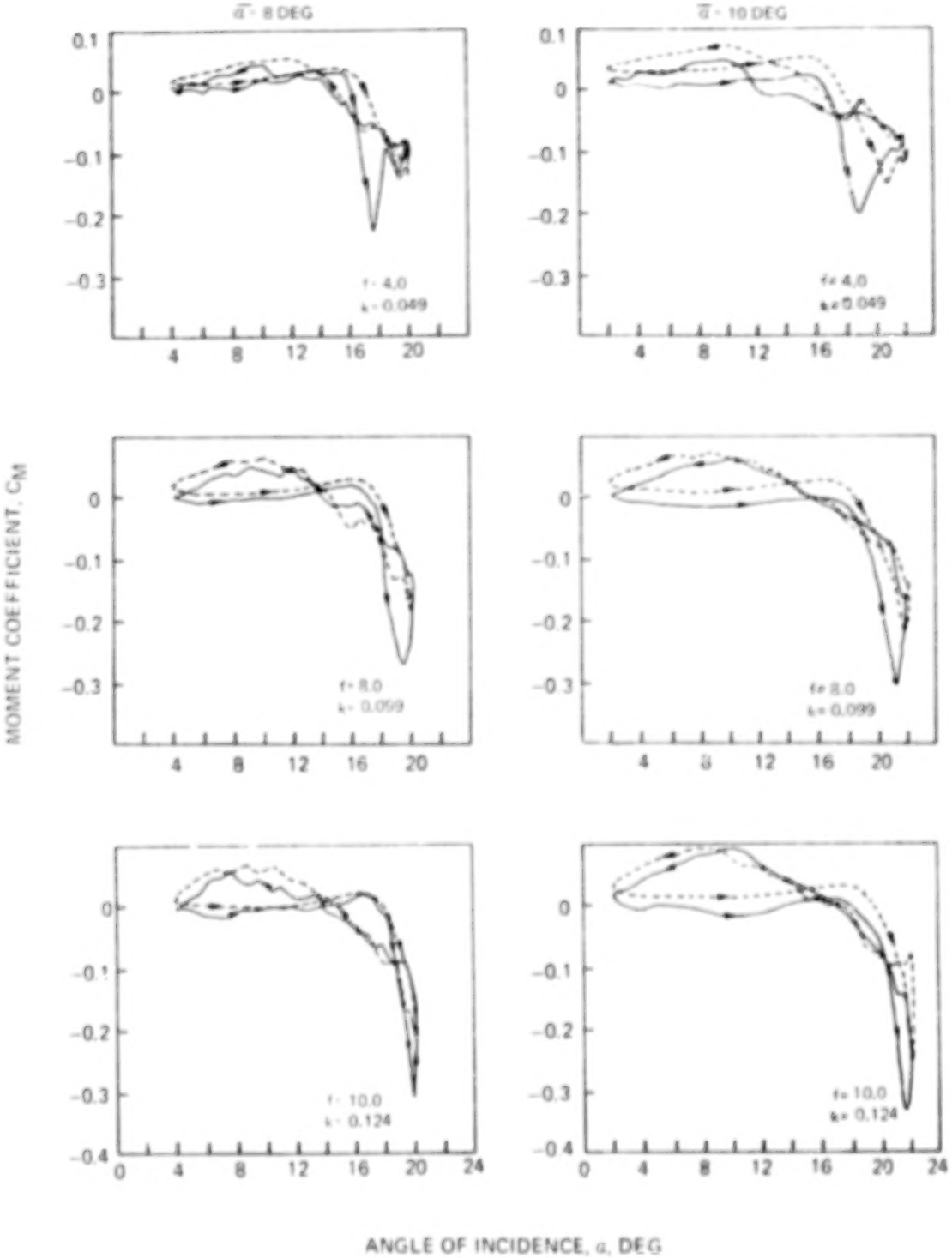

Figure 24 Effect of Sweep, Amplitude and Frequency on the Induced Moment Response for $M_c = 0.30$ and $\alpha_M = 12$ Deg —— $\Lambda = 0$ Deg; - - - - - $\Lambda = 30$ Deg

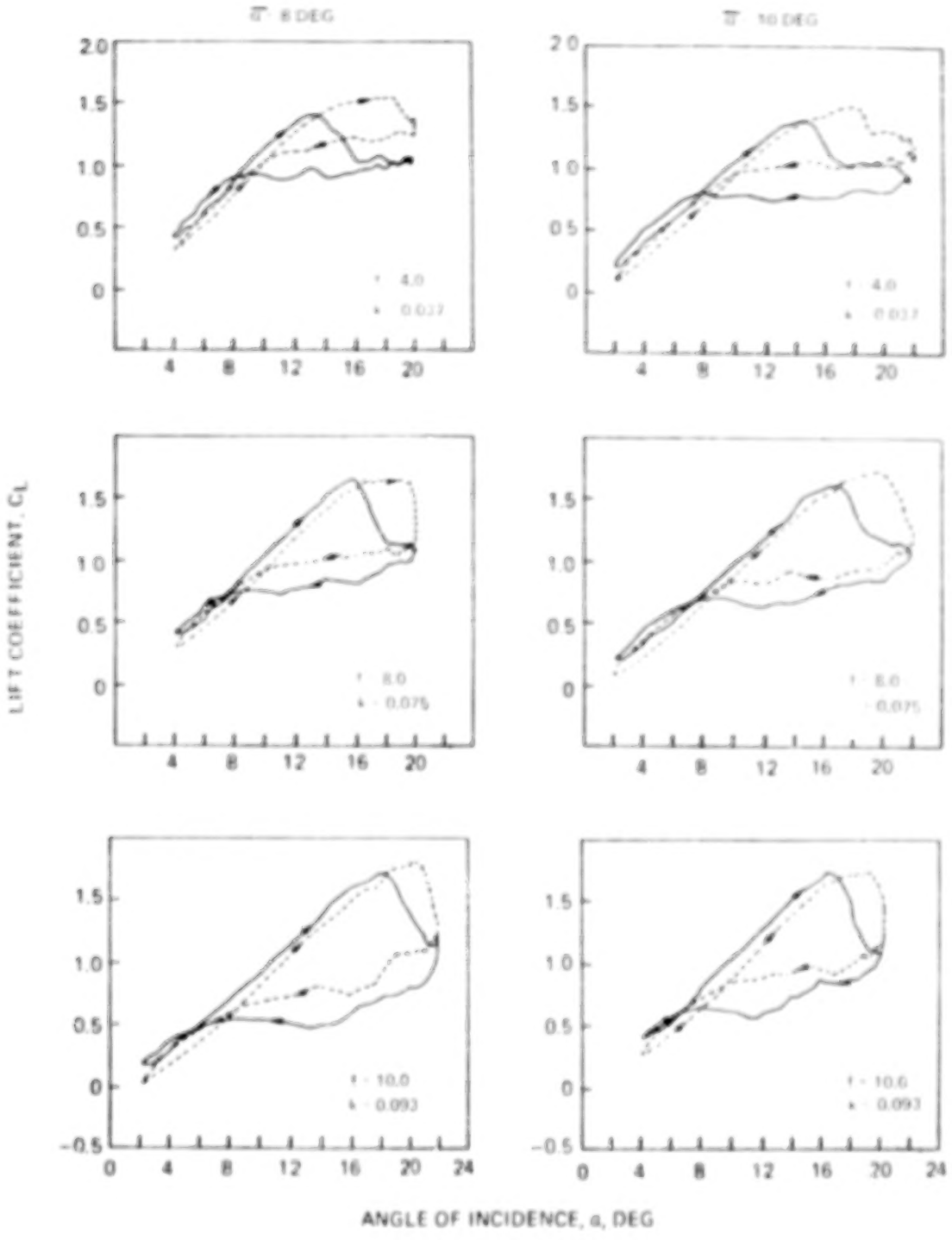

Figure 25 Effect of Sweep, Amplitude and Frequency on the Induced Lift Response for M_c = 0.40 and α_M = 12 deg. —— Λ = 0 deg; - - - - Λ = 30 deg.

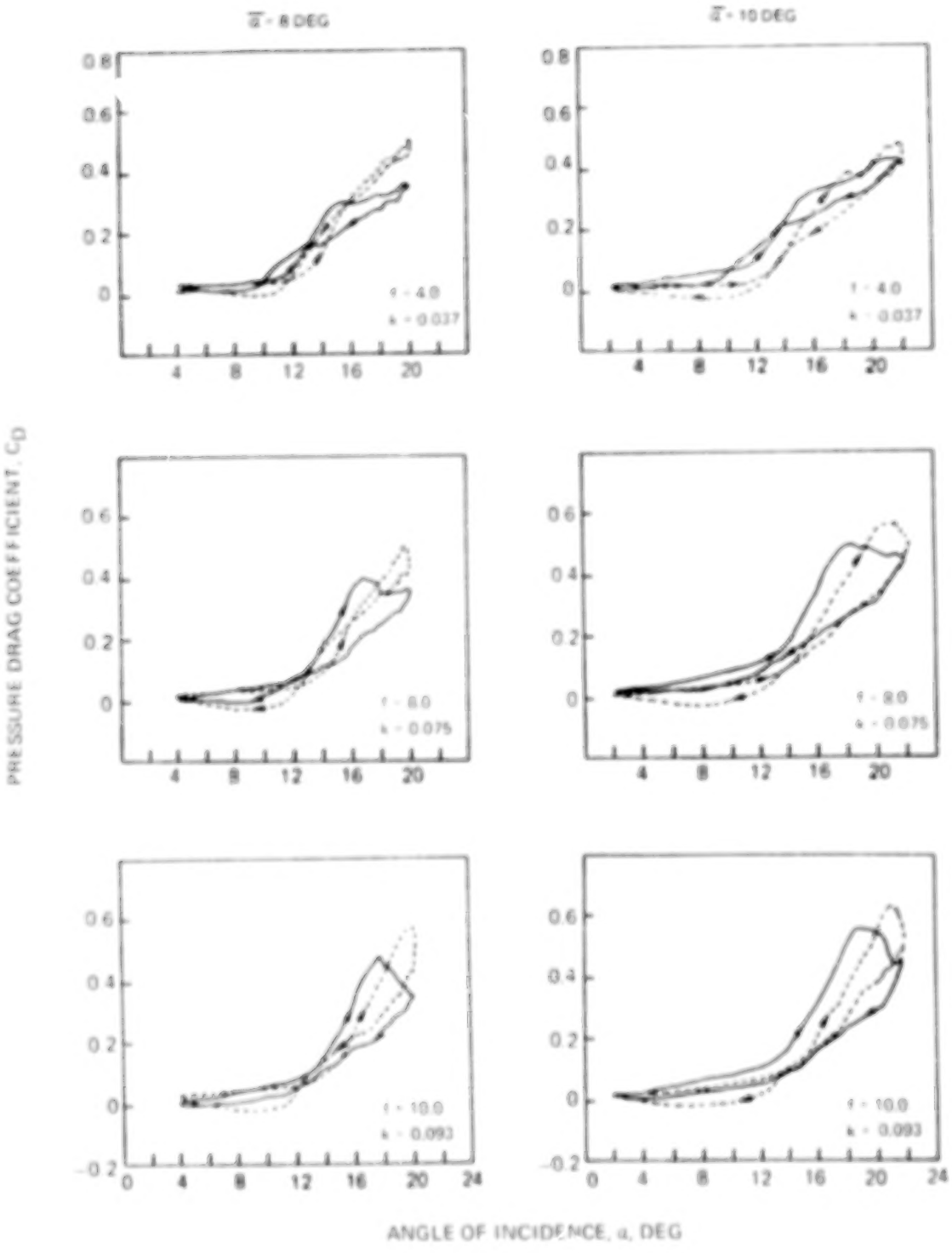

Figure 26 Effect of Sweep, Amplitude and Frequency on the Induced Pressure Response for M_c = 0.40 and α_M = 12 Deg—— Λ = 0 Deg;– – – Λ = 30 Deg

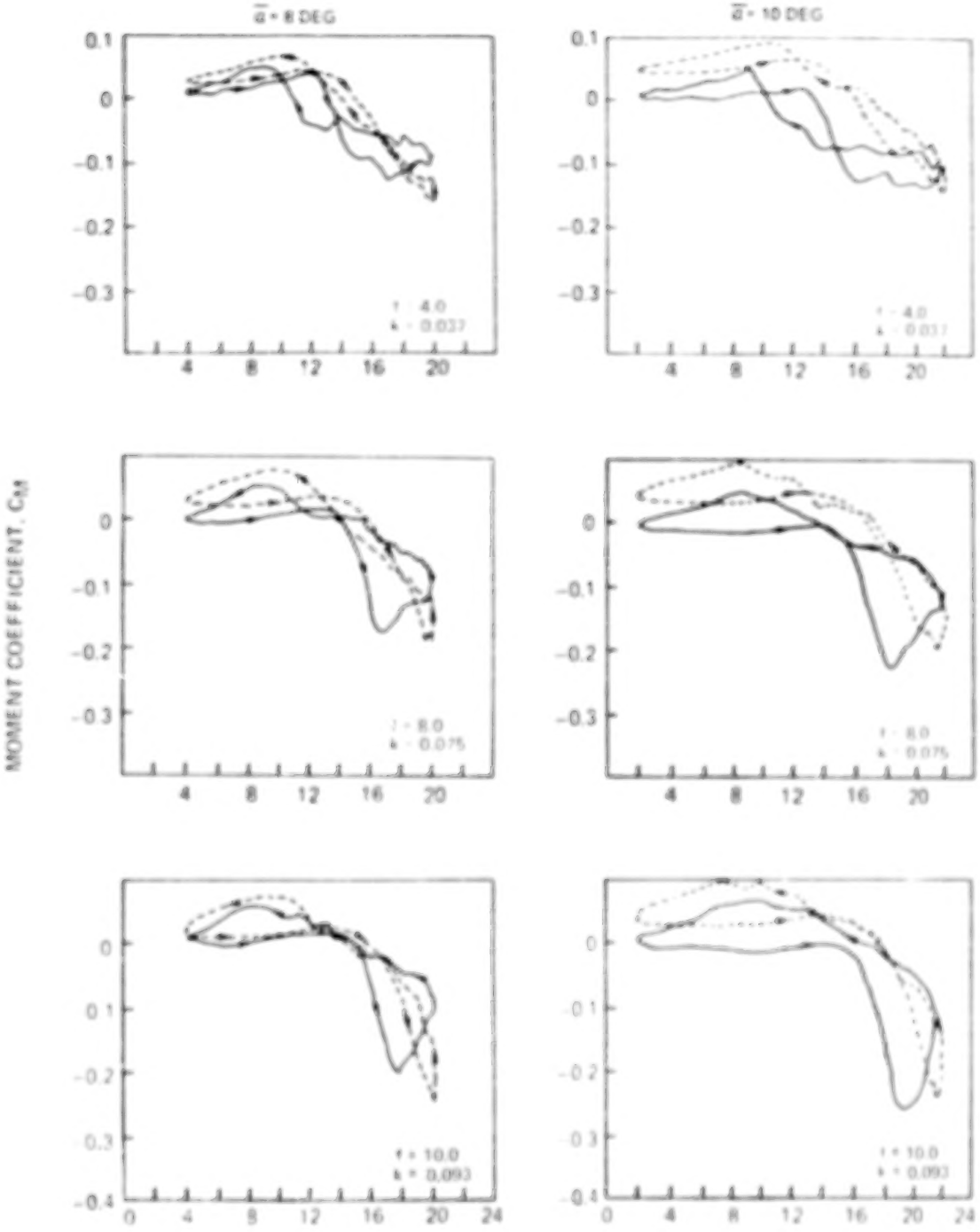

Figure 27 Effect of Sweep, Amplitude and Frequency on the Induced Moment Response for M_c = 0.40 and α_M = 12 Deg.—— Λ = 0 Deg; - - - - - - Λ = 30 Deg

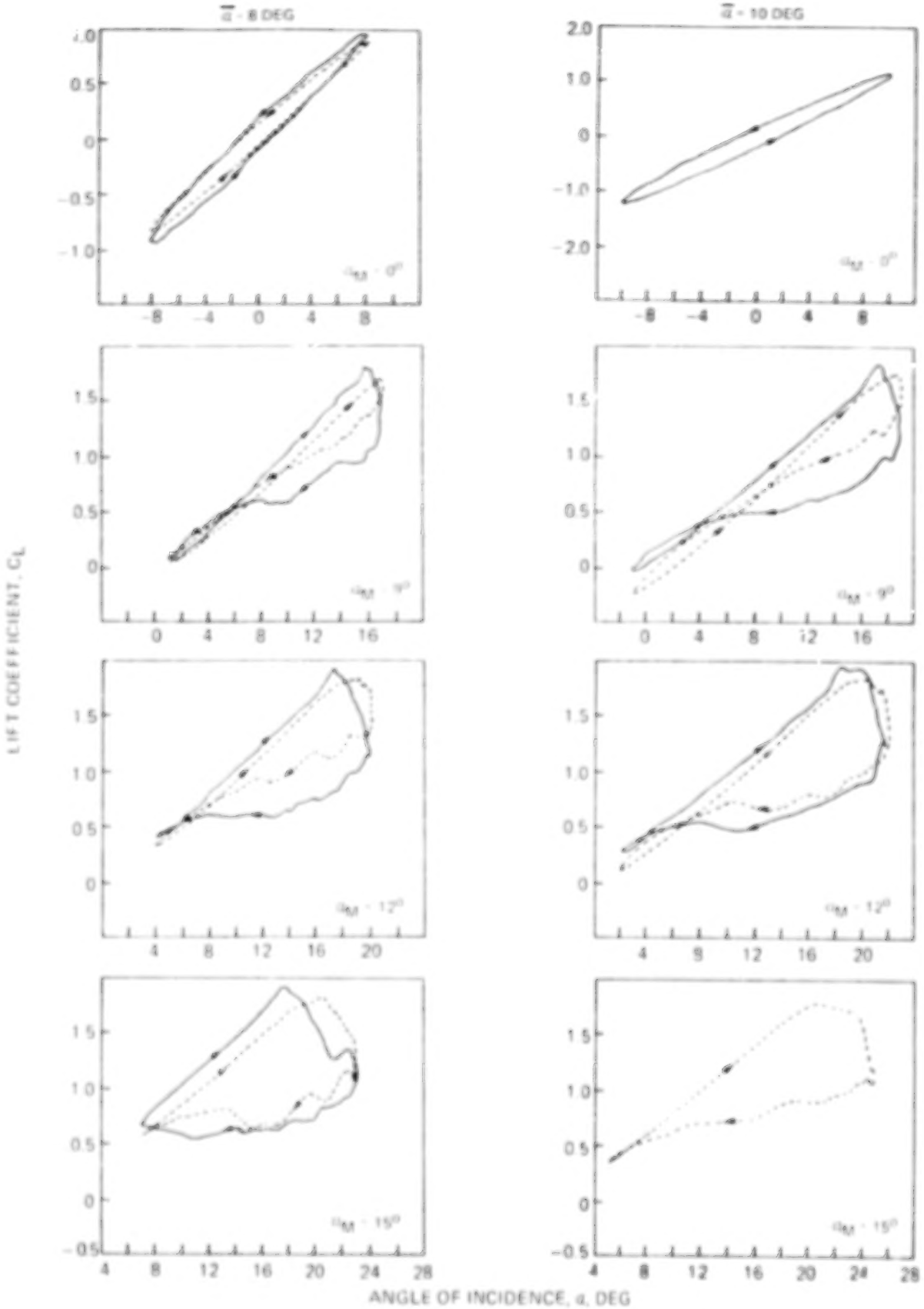

Figure 28 Effect of Sweep, Amplitude and Mean Incidence Angle on the Induced Lift Response for M_c = 0.30 and f = 8 cps, (k = 0.099), ——— Λ = 0 Deg; ------ Λ = 30 Deg

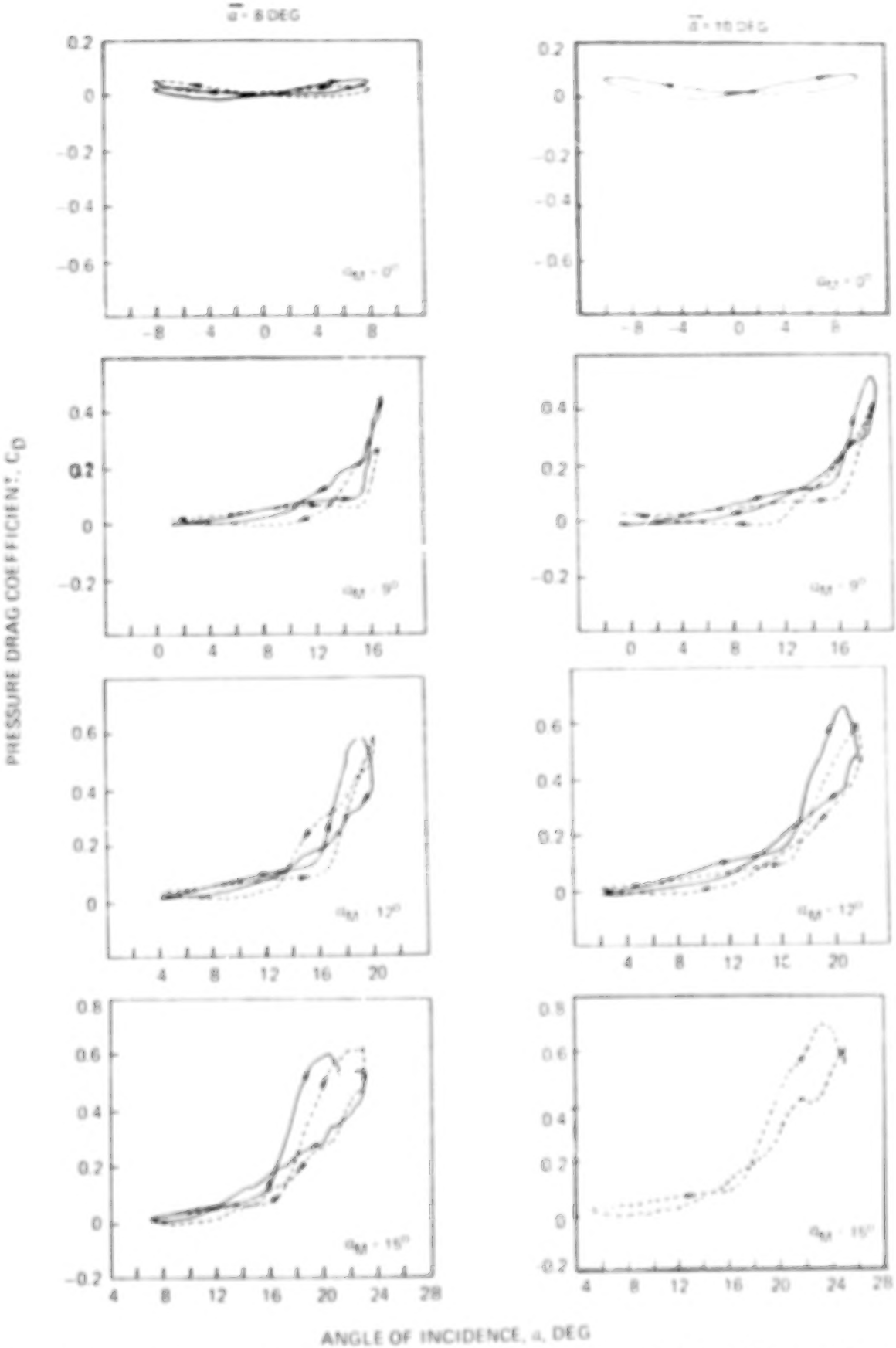

Figure 29 Effect of Sweep, Amplitude and Mean Incidence Angle on the Induced Pressure Drag Response for M_C = 0.30 and f = 8 cps, (k = 0.099), ——— Λ = 0 Deg; – – – – Λ = 30 Deg

TABLE OF CONTENTS

	Page No.	
SUMMARY	1	1/A8
INTRODUCTION	2	1/A9
LIST OF SYMBOLS	3	1/A10
WIND TUNNEL AND EXPERIMENTAL EQUIPMENT	7	1/A14
Wind Tunnel	7	1/A14
Tunnel Spanning Wing and Drive System	7	1/A14
Test Airfoil and Instrumentation	8	1/B1
TEST PROGRAM AND COMPUTATIONAL PROCEDURES	11	1/B4
Calibration Procedures	11	1/B4
Test Plan	11	1/B4
Unsteady Data Acquisition	12	1/B5
Force and Moment Computation Procedure	13	1/B6
Aerodynamic Damping Computation Procedure	16	1/B9
STEADY STATE RESULTS	17	1/B10
Wind Tunnel Wall Corrections	17	1/B10
Steady State Respons	18	1/B11
UNSTEADY RESULTS	20	1/B13
Pressure Time Histories	20	1/B13
Force and Pitching Moment Loops	20	1/B13
Discussion of Unsteady Response	21	1/B14
Discussion of Simple Sweep Theory	24	1/C3
Discussion of Aerodynamic Damping and Stability	25	1/C4
FLUCTUATING PRESSURES ON STEADY AIRFOIL	27	1/C6
Background Information	27	1/C6
Time Histories - Unswept Airfoil	27	1/C6
Time Histories - Swept Airfoil	36	1/D1
CONCLUSIONS AND OBSERVATIONS	40	1/D5
RECOMMENDATIONS	42	1/D7

TABLE OF CONTENTS (Cont'd)

		Page No.	
APPENDIXES			
I.	NUMERICAL INTEGRATION ESTIMATE OF UNSTEADY LOAD	43	1/D8
II.	NUMERICAL INTEGRATION METHODS	46	1/D11
III.	WIND TUNNEL WALL CORRECTIONS DUE TO A LIFTING SURFACE IN OBLIQUE FLOW	47	1/D12
REFERENCES		51	1/E2
TABLES		54	1/E4
FIGURES		57	1/E8

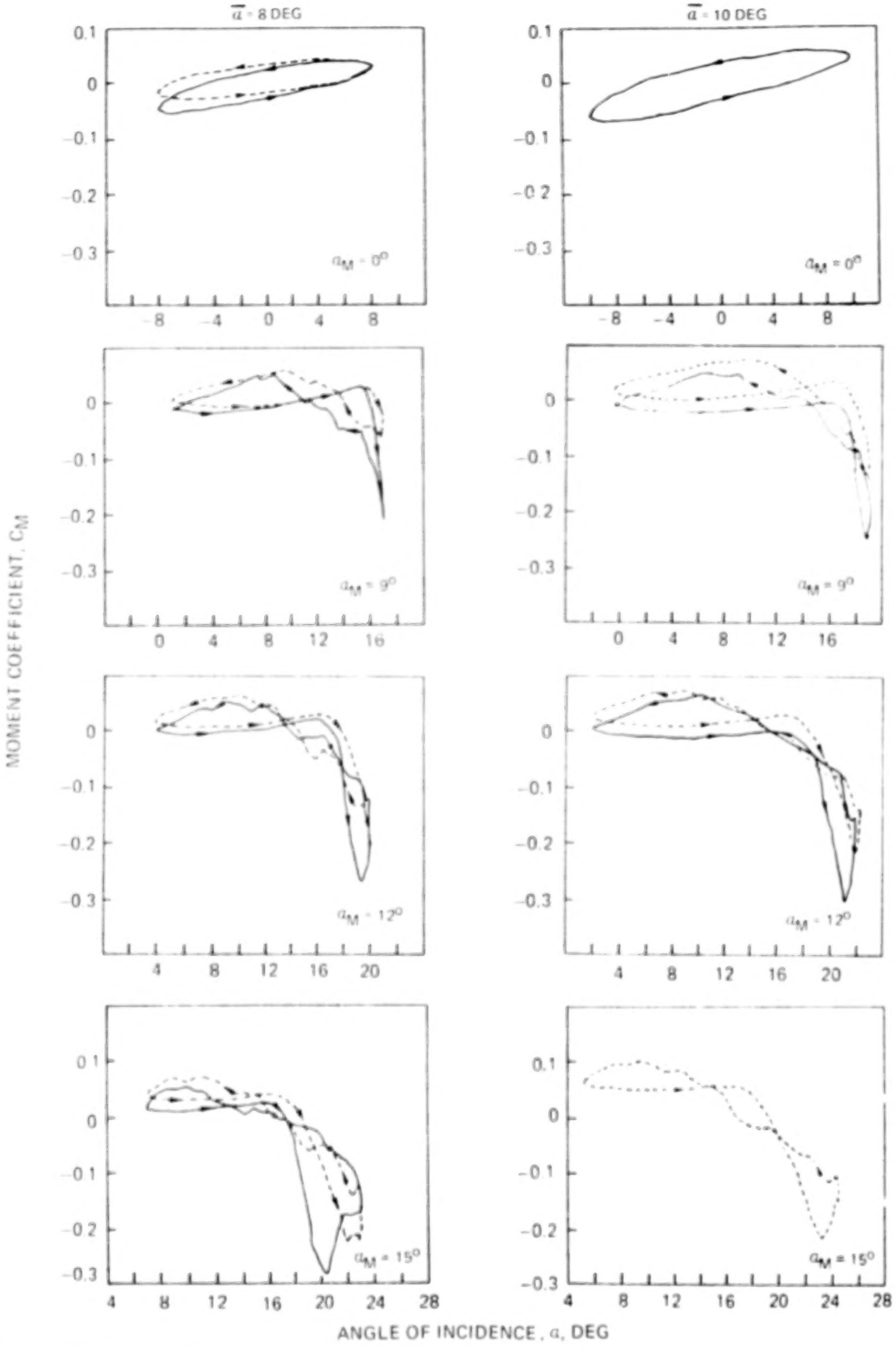

Figure 30 Effect of Sweep, Amplitude and Mean Incidence Angle on the Induced Moment Response for $M_c = 0.30$ and f = 8 cps (k = 0.099), ——— Λ = 0 Deg; - - - - Λ = 30 Deg

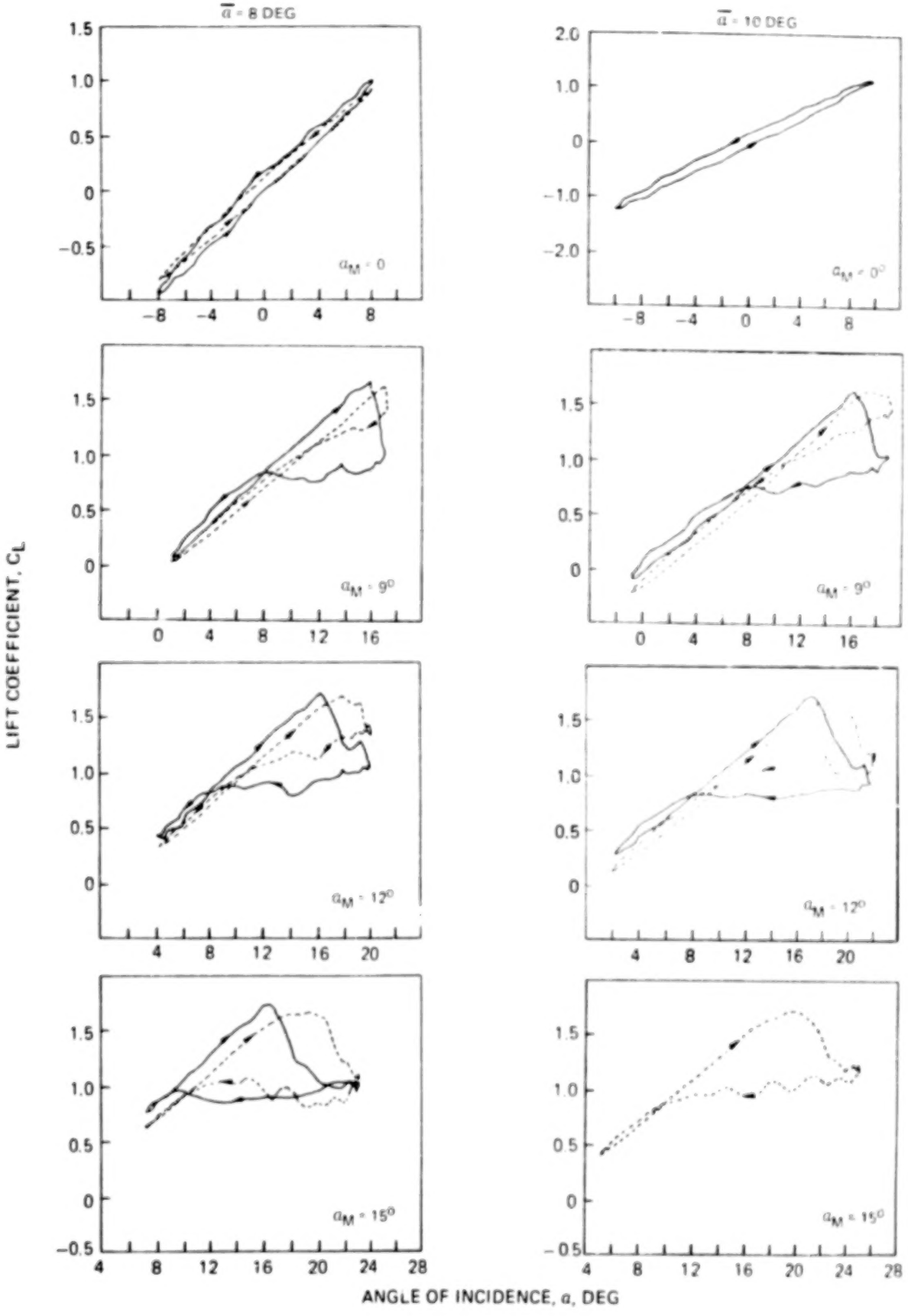

Figure 31 Effect of Sweep, Amplitude and Mean Incidence Angle on the Induced Lift Response for M_c = 0.30 and f = 4 cps (k = 0.049), —— Λ = 0 Deg; - - - - Λ = 30 Deg

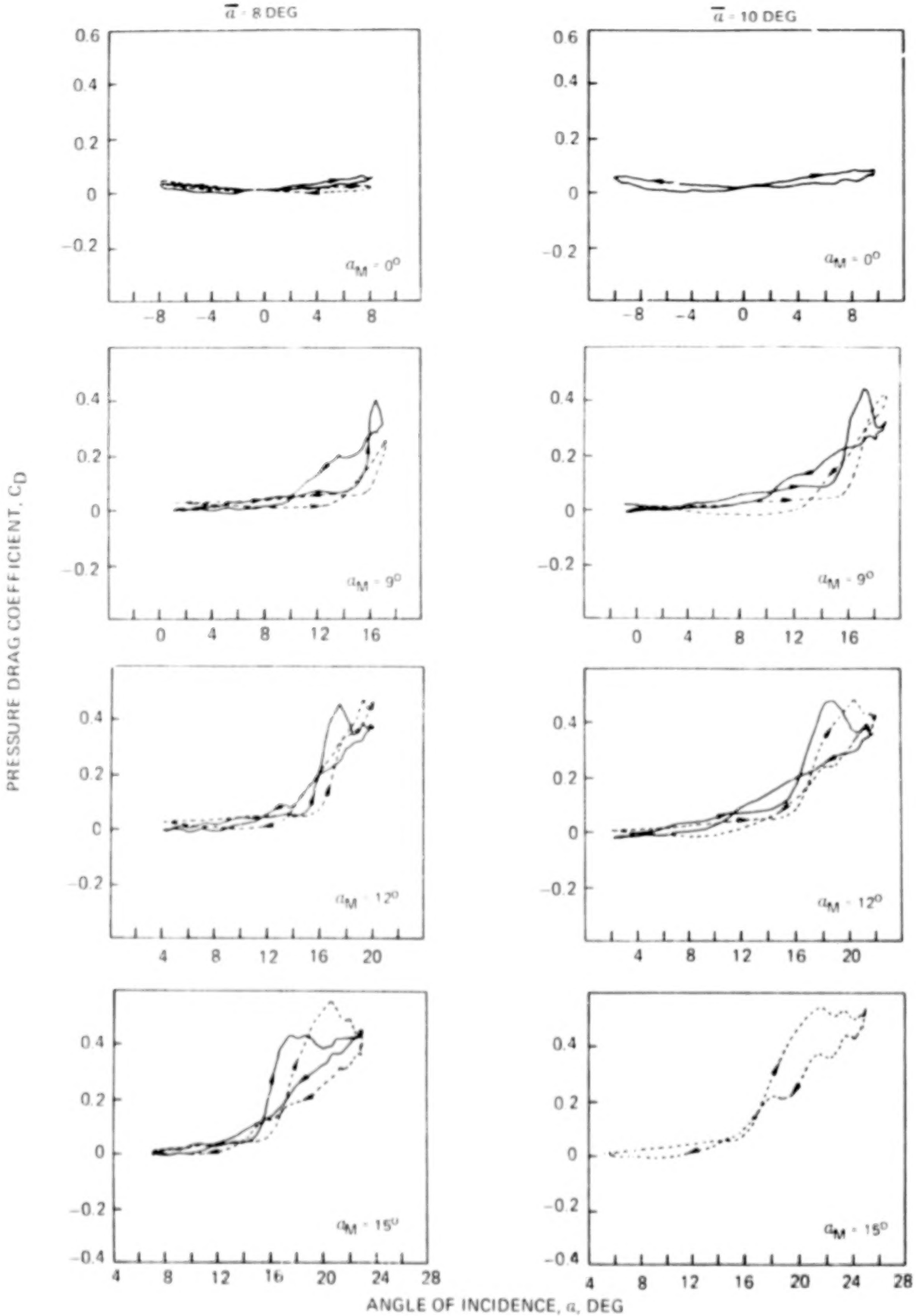

Figure 32 Effect of Sweep, Amplitude and Mean Incidence Angle on the Induced Pressure Drag Response for M_c = 0.30 and f = 4 cps (k = 0.049), —— Λ = 0 Deg; – – – – Λ = 30 Deg

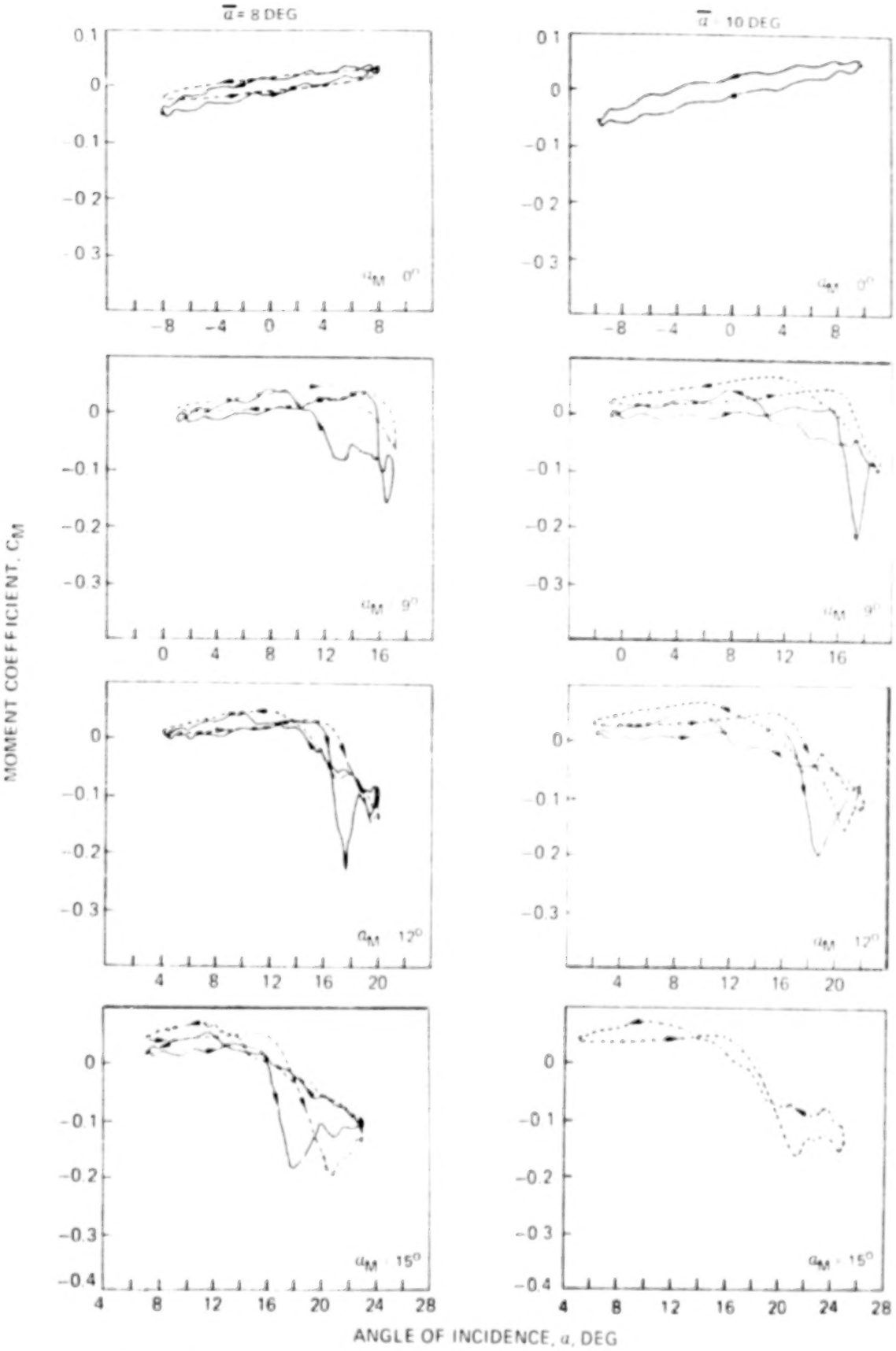

Figure 33 Effect of Sweep, Amplitude and Mean Incidence Angle on the Induced Moment Response for M_C = 0.30 and f = 4 cps (k = 0.049), —— Λ = 0 Deg; - - - Λ = 30 Deg

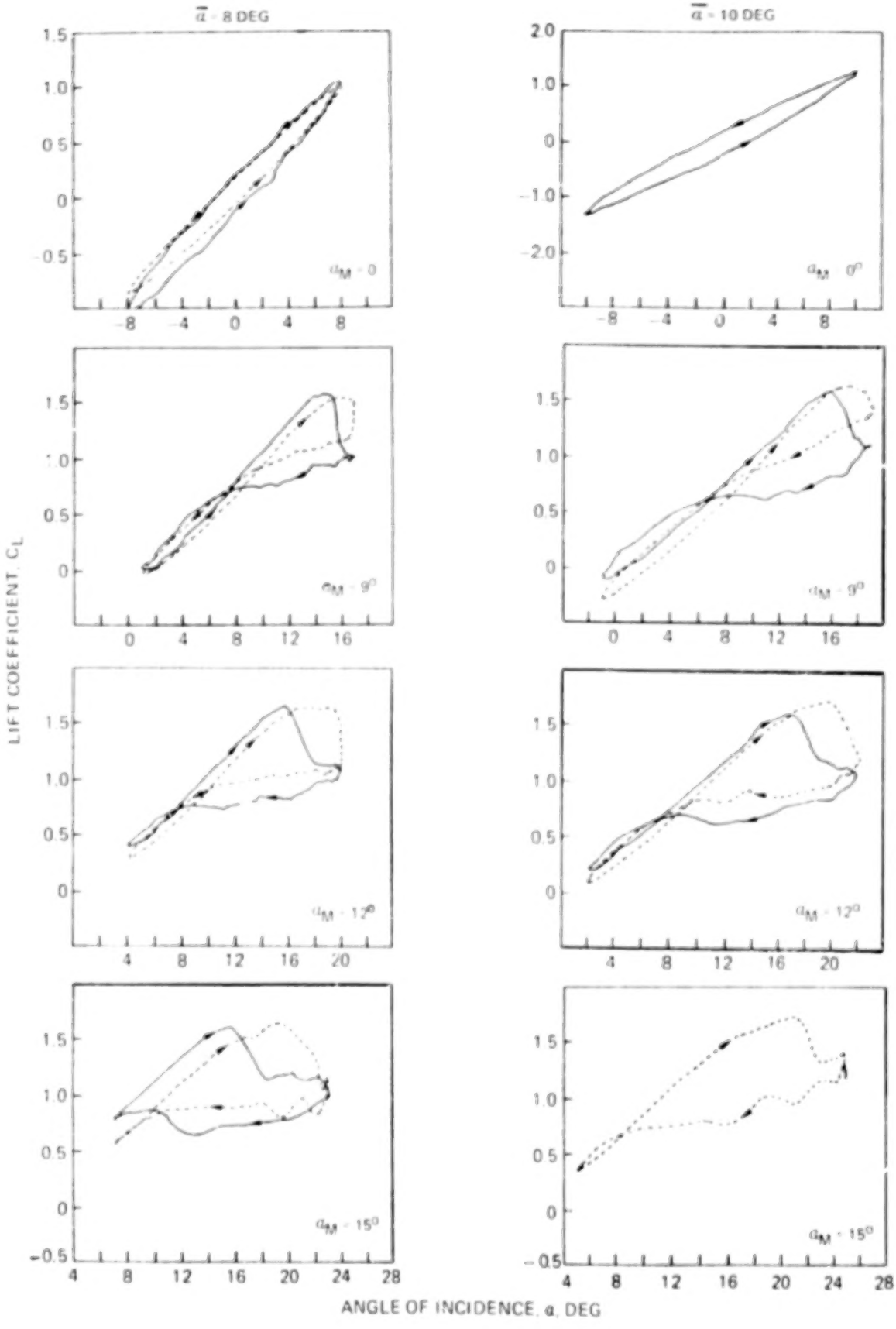

Figure 34 Effect of Sweep, Amplitude and Mean Incidence Angle on the Induced Lift Response for M_c = 0.40 and f = 8 cps, (k = 0.075), —— Λ = 0 Deg; ------ Λ = 30 Deg

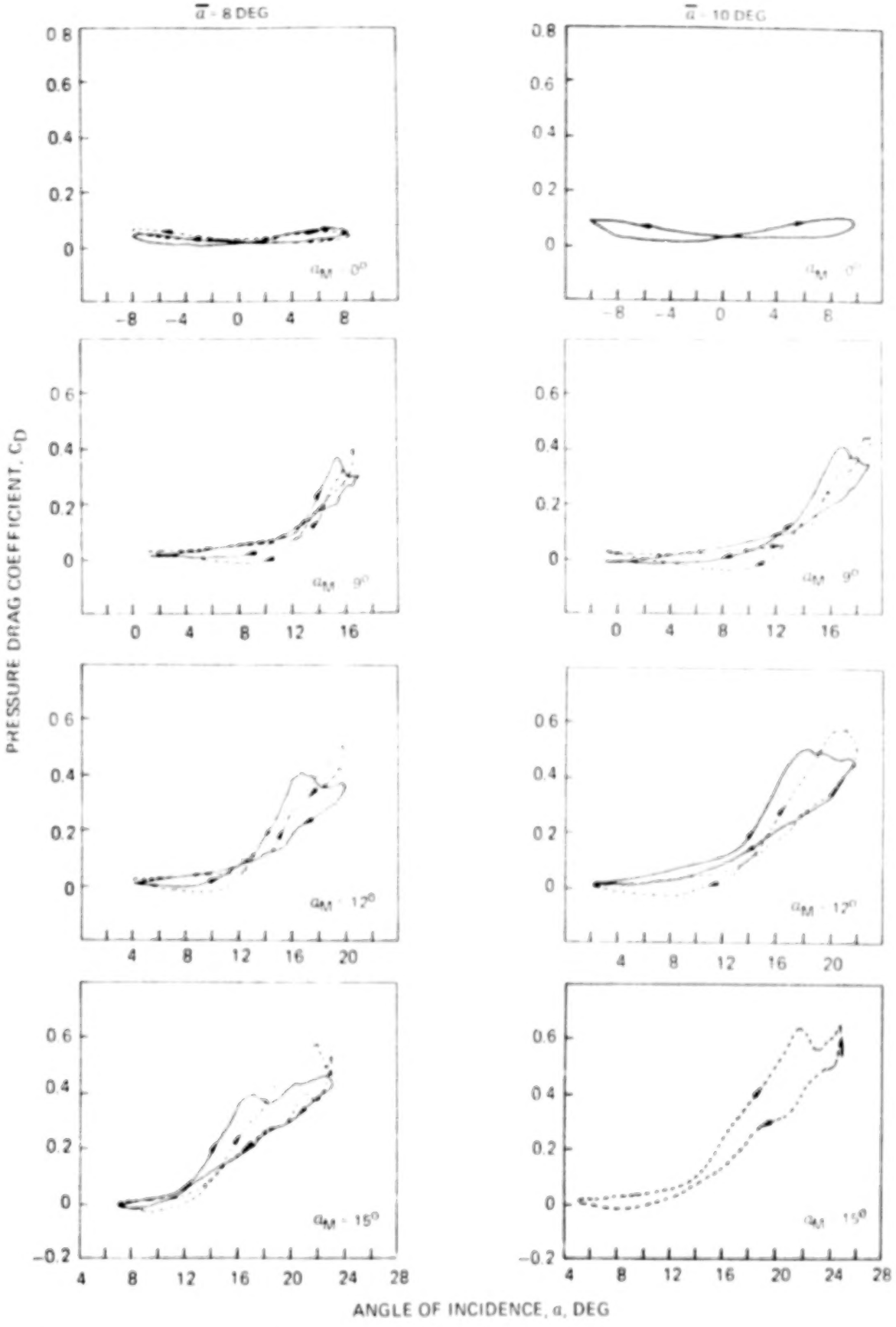

Figure 35 Effect of Sweep, Amplitude and Mean Incidence Angle on the Induced Pressure Drag Response for M_c = 0.40 and f = 8 cps, (k = 0.075), —— Λ = 0 Deg; - - - - Λ = 30 Deg

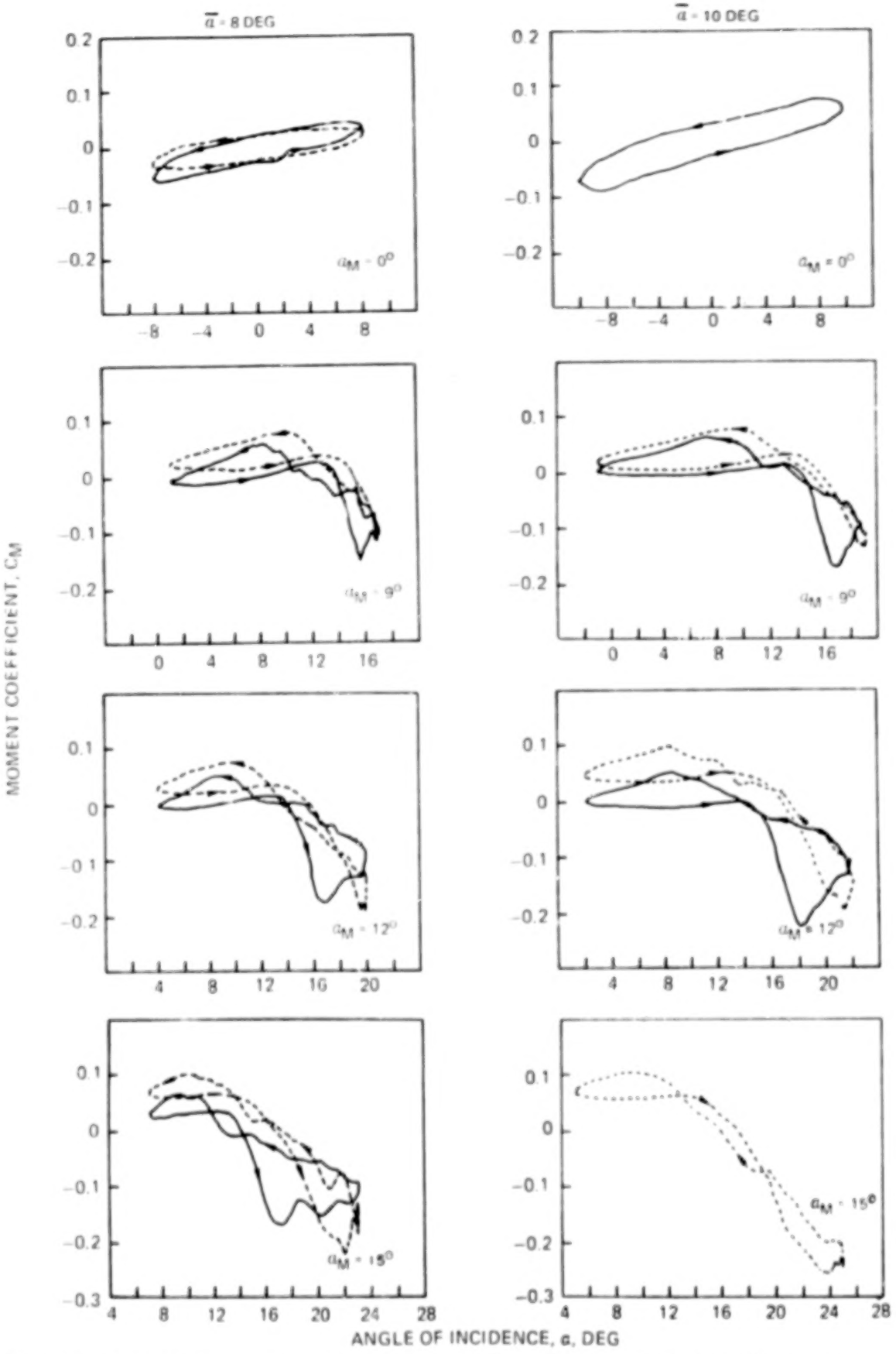

Figure 36 Effect of Sweep, Amplitude and Mean Incidence Angle on the Induced Moment Response for M_c = 0.40 and f = 8 cps, (k = 0.075), ——— Λ = 0 Deg; – – – – Λ = 30 Deg

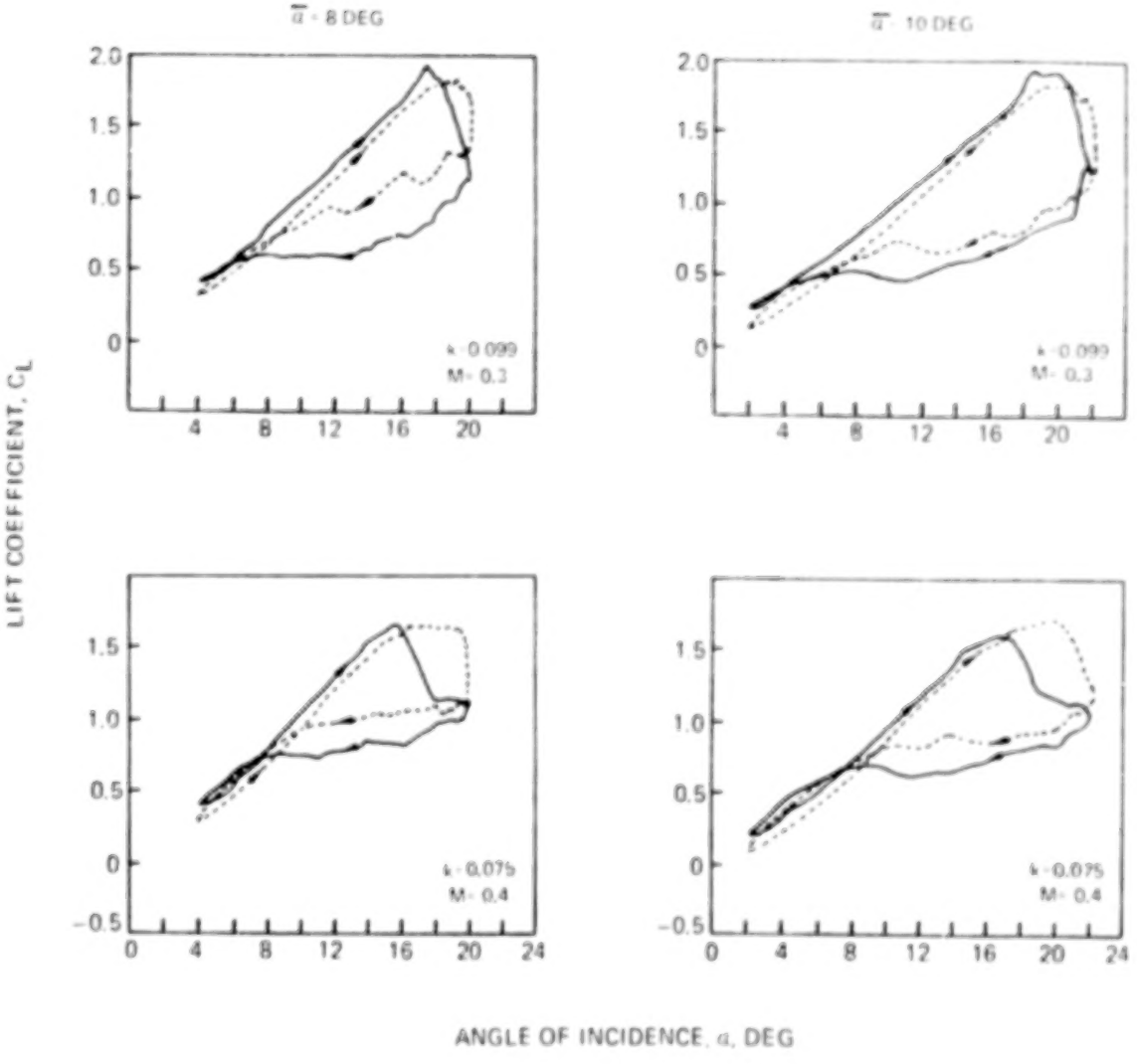

Figure 37 Effect of Sweep, Amplitude and Mach Number on the Induced Lift Response for α_M = 12 Deg and f = 8 cps, ——— Λ = 0 Deg; - - - - - Λ = 30 Deg

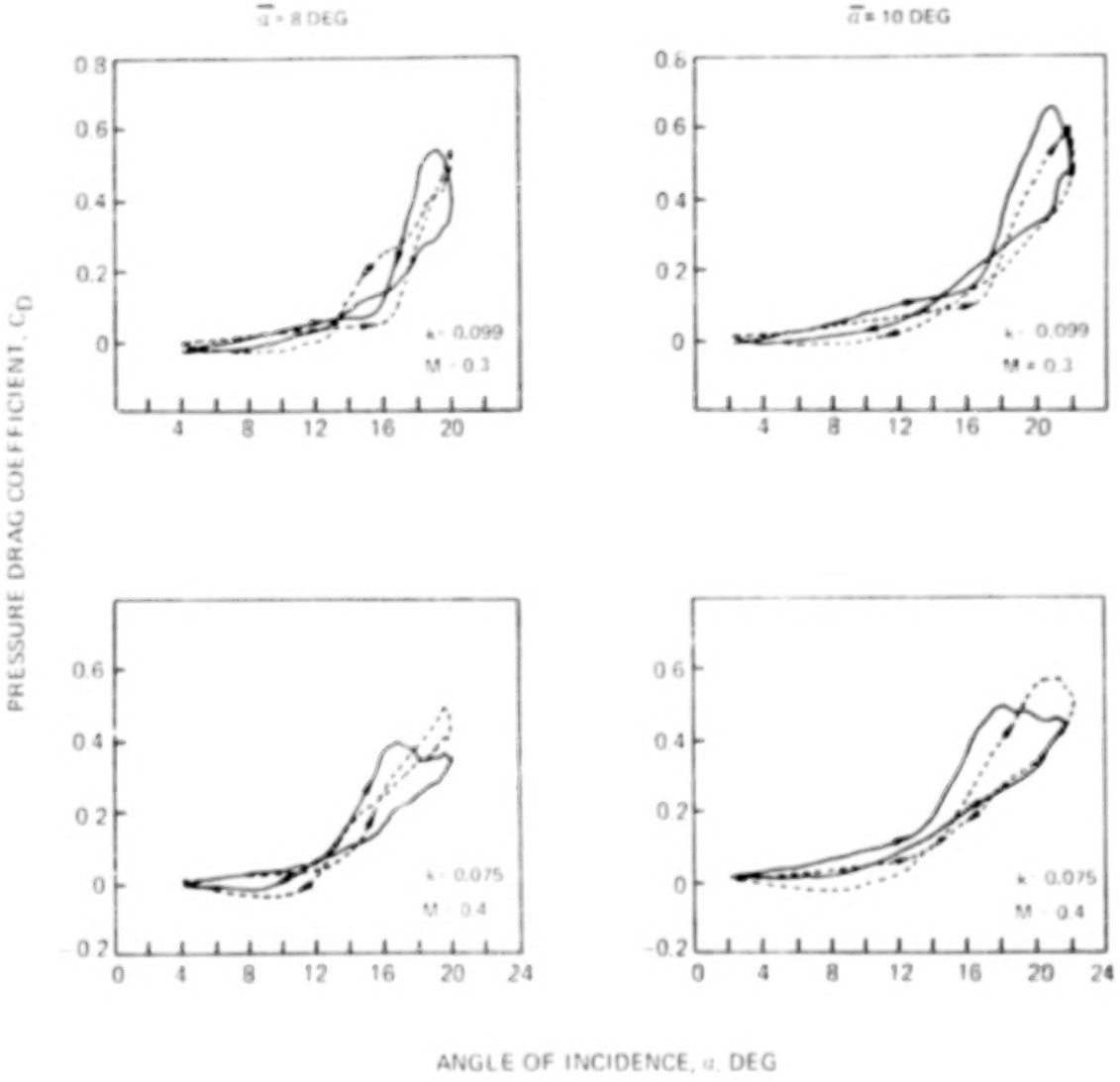

Figure 38 Effect of Sweep, Amplitude and Mach Number on the Induced Pressure Drag Response for α_M = 12 Deg and f = 8 cps , —— Λ = 0 Deg; - - - Λ = 30 Deg

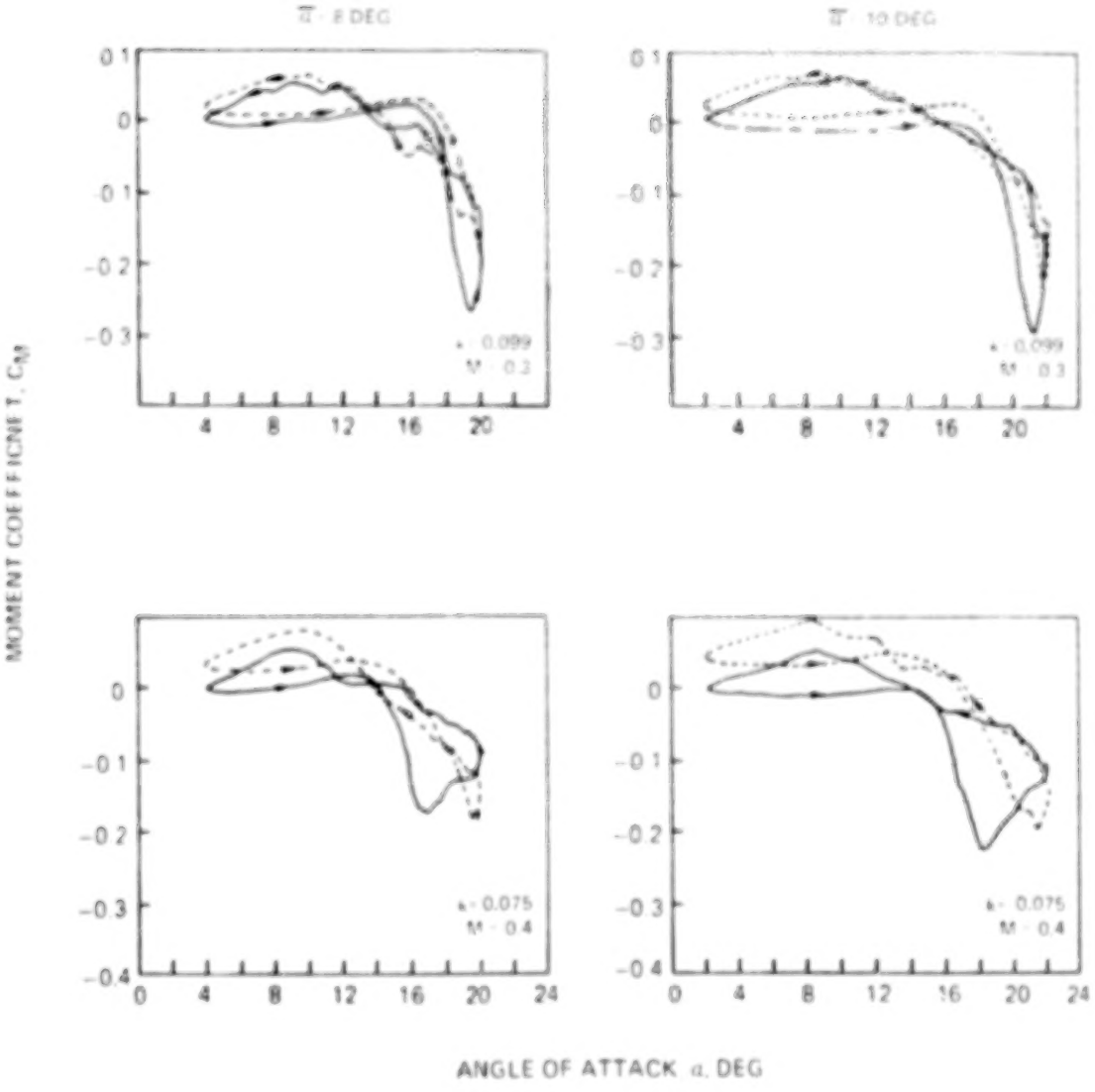

Figure 39 Effect of Sweep, Amplitude and Mach Number Induced Moment Response for α_M = 12 Deg and f = 8 cps, ——— Λ = 0 Deg; - - - Λ = 30 Deg

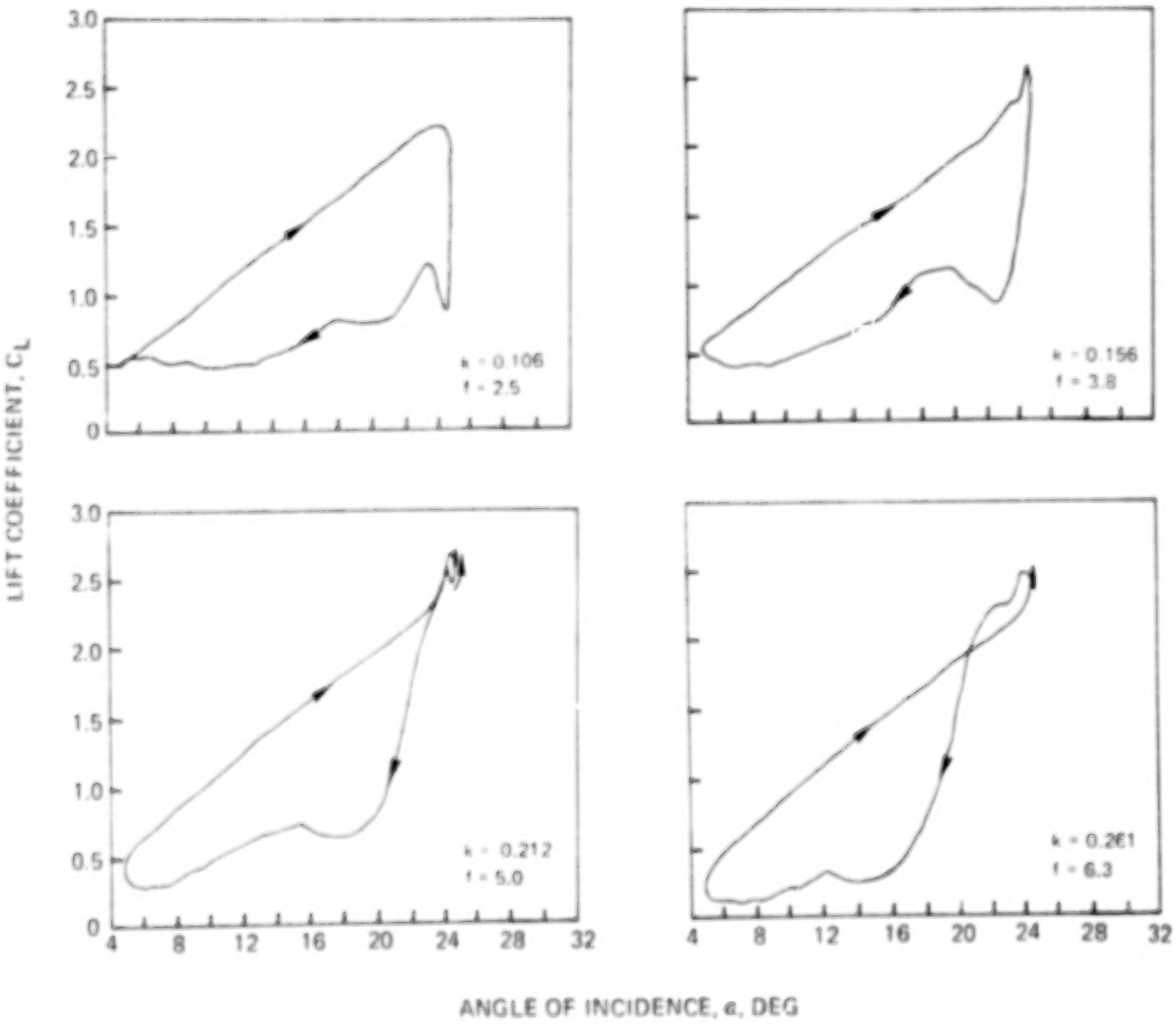

Figure 40 Effect of Frequency on the Induced Lift Response for $M_c = 0.1$, $\alpha_M = 15$ Deg, $\bar{\alpha} = 10$ Deg, $\Lambda = 30$ Deg

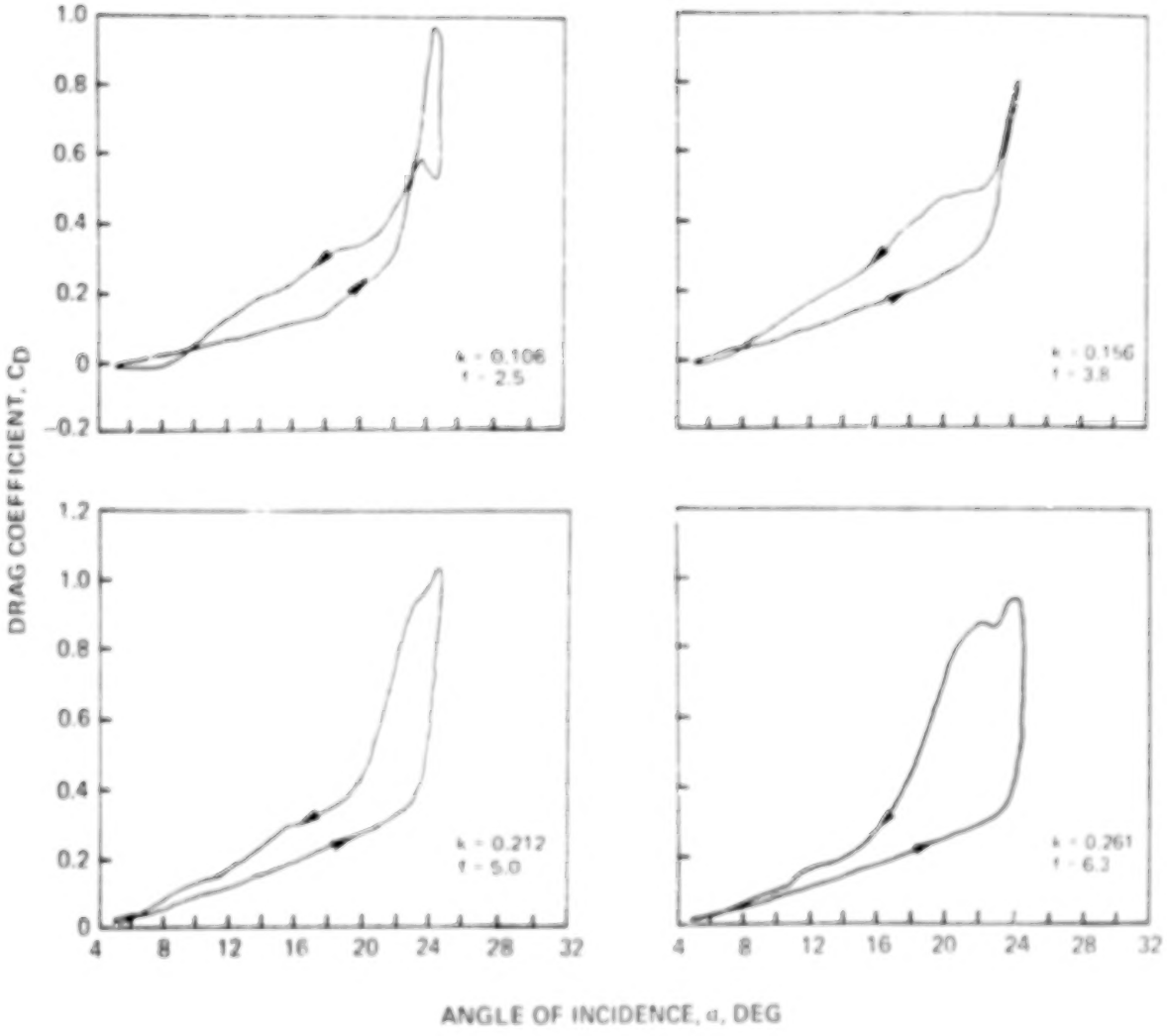

Figure 41 Effect of Frequency on the Induced Pressure Drag Response for $M_C = 0.1$, $\alpha_M = 15$ Deg, $\bar{\alpha} = 10$ Deg, $\Lambda = 30$ Deg

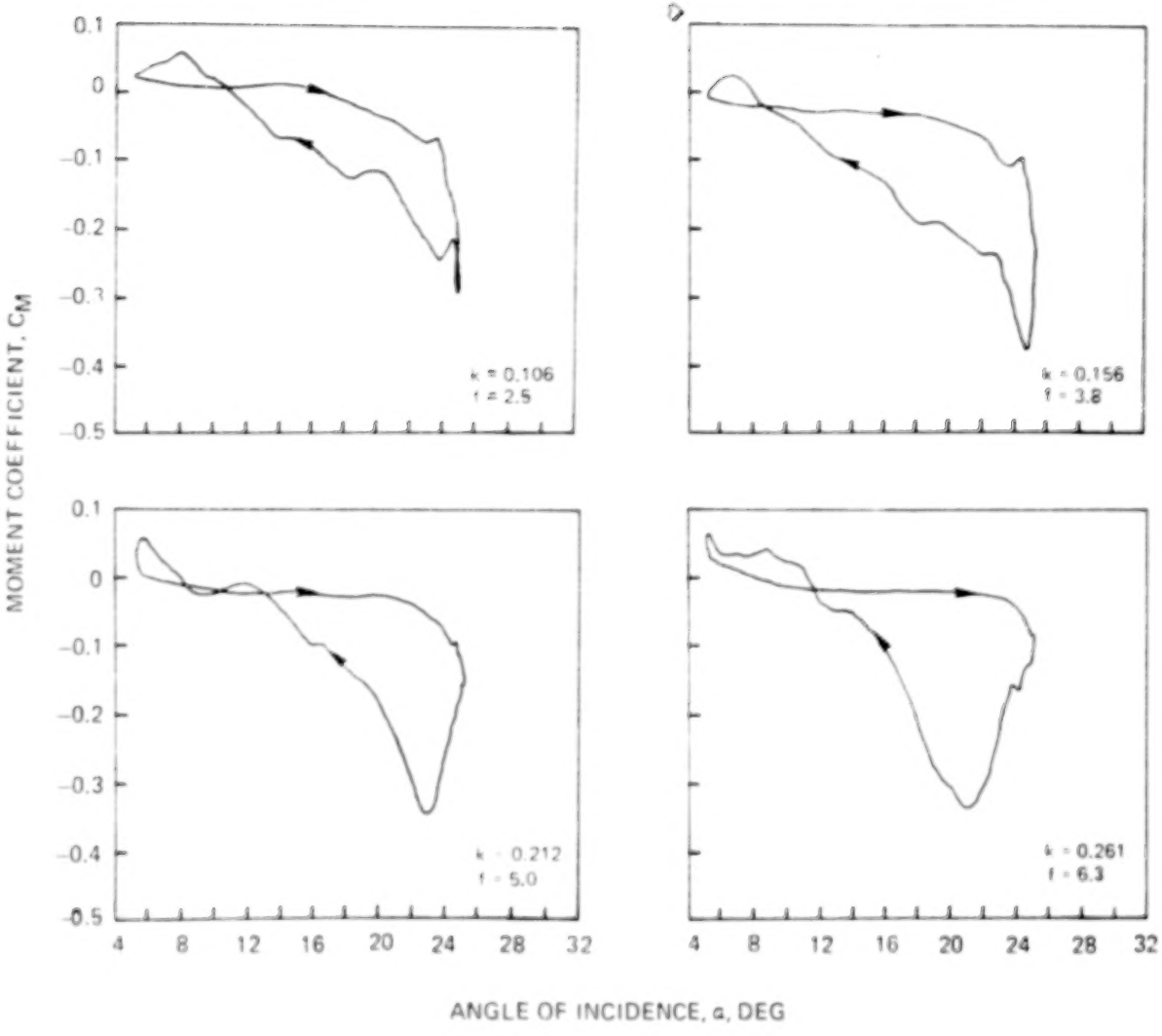

Figure 42 Effect of Frequency on the Induced Moment Response for $M_C = 0.1$, $\alpha_M = 15$ Deg, $\bar{\alpha} = 10$ Deg, $\Lambda = 30$ Deg

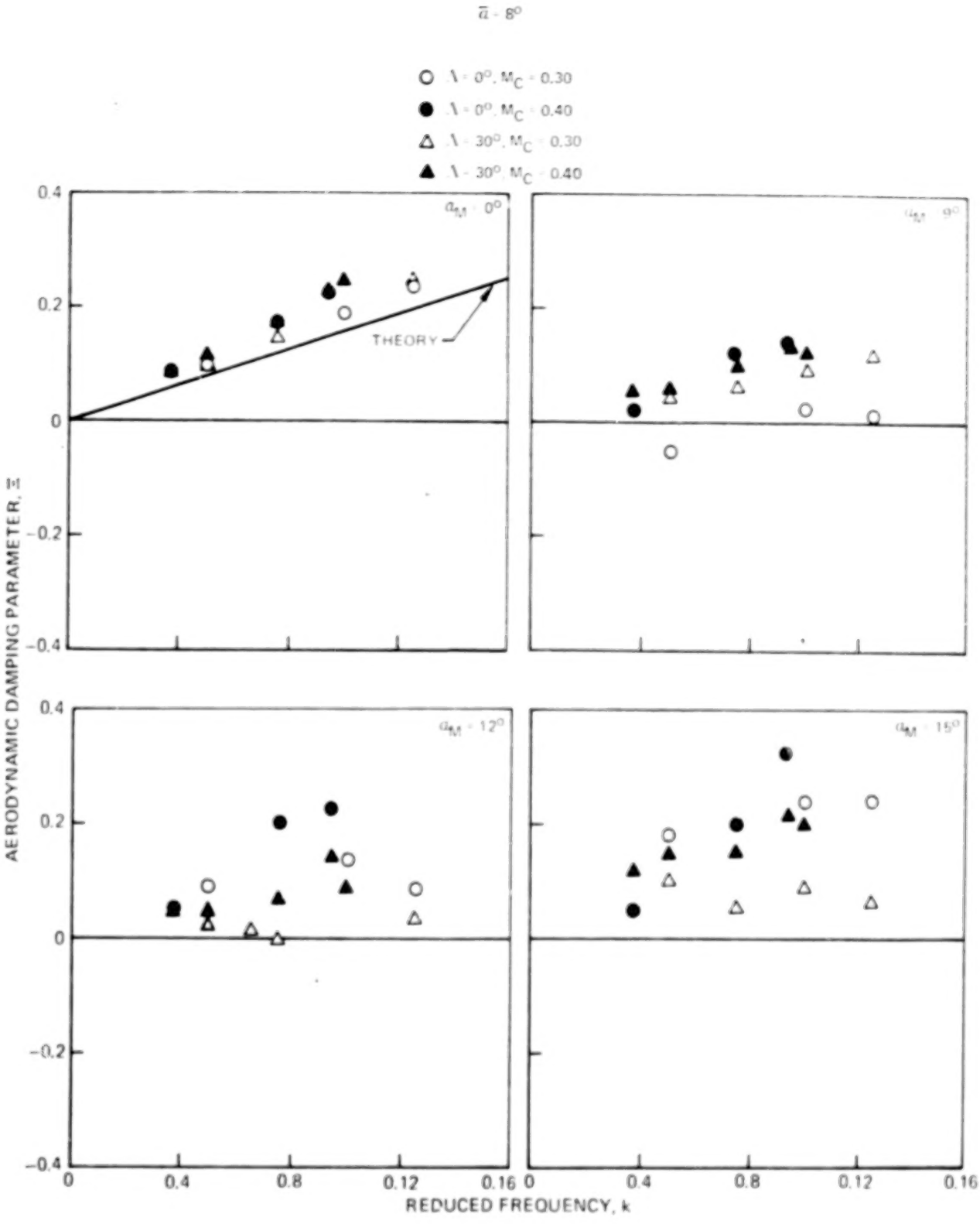

Figure 43 Variation of aerodynamic damping parameter with reduced frequency

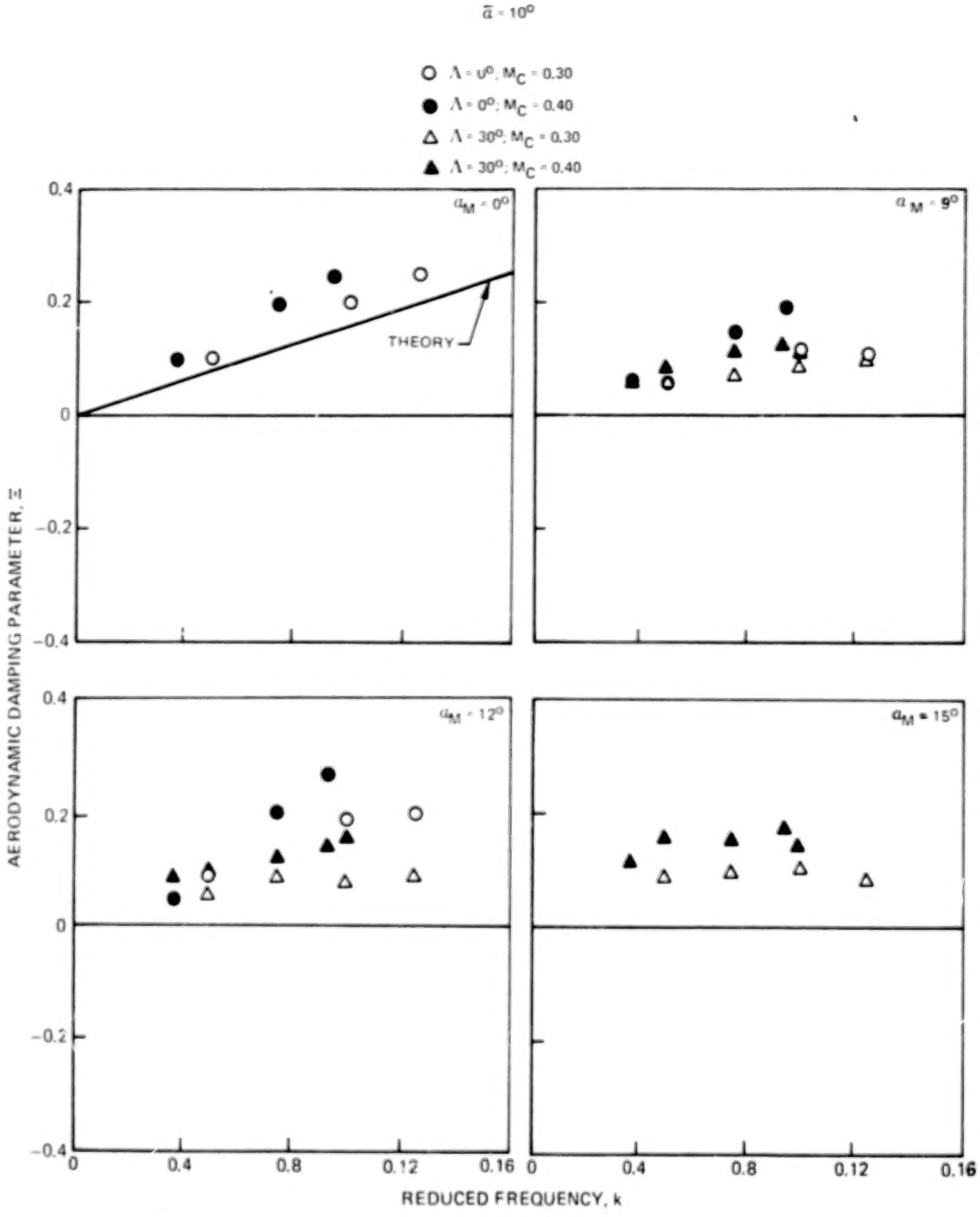

Figure 44 Variation of aerodynamic damping parameter with reduced frequency

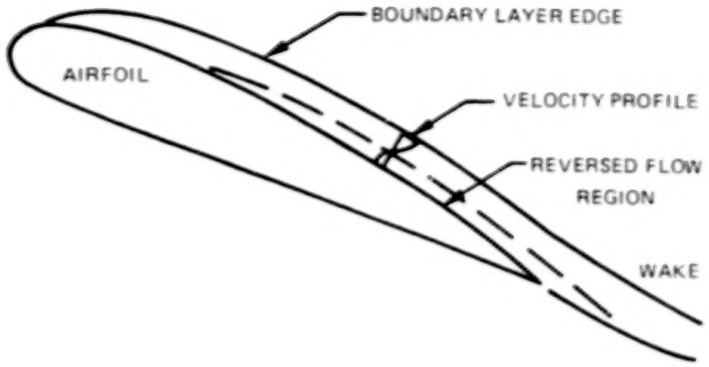

(a) UNSTEADY FLOW, INCREASING ANGLE OF ATTACK

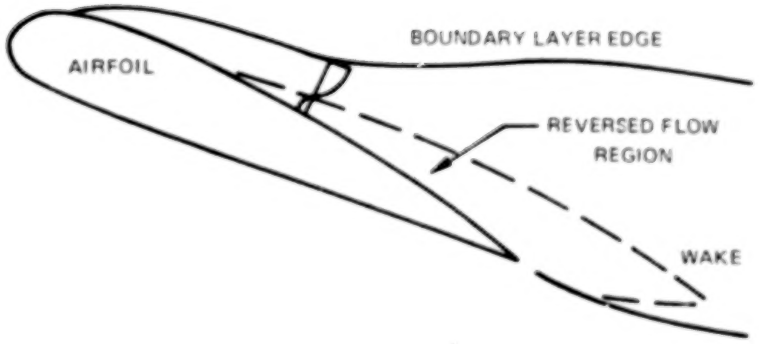

(b) STEADY MEAN FLOW, SAME ANGLE OF ATTACK

Figure 45 Flow Fields Near an Airfoil at Steady and Unsteady Angle of Attack

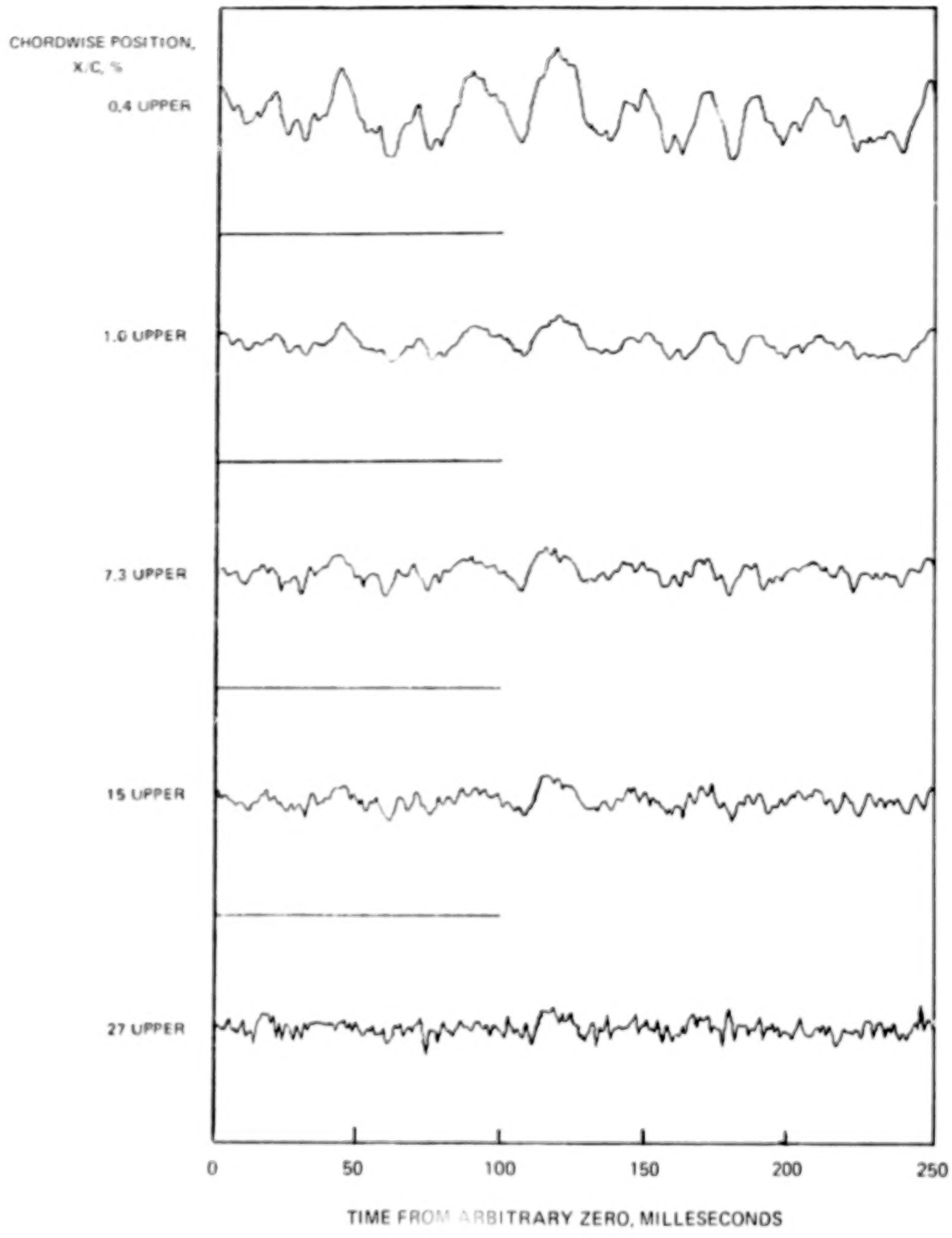

Figure 46 Absolute-Level Pressure Fluctuations on a Chordwise Line Along a Steady Unswept NACA 0012 Airfoil at 0.30 Mach Number and 15° Angle of Attack. (a) Forward Upper Surface

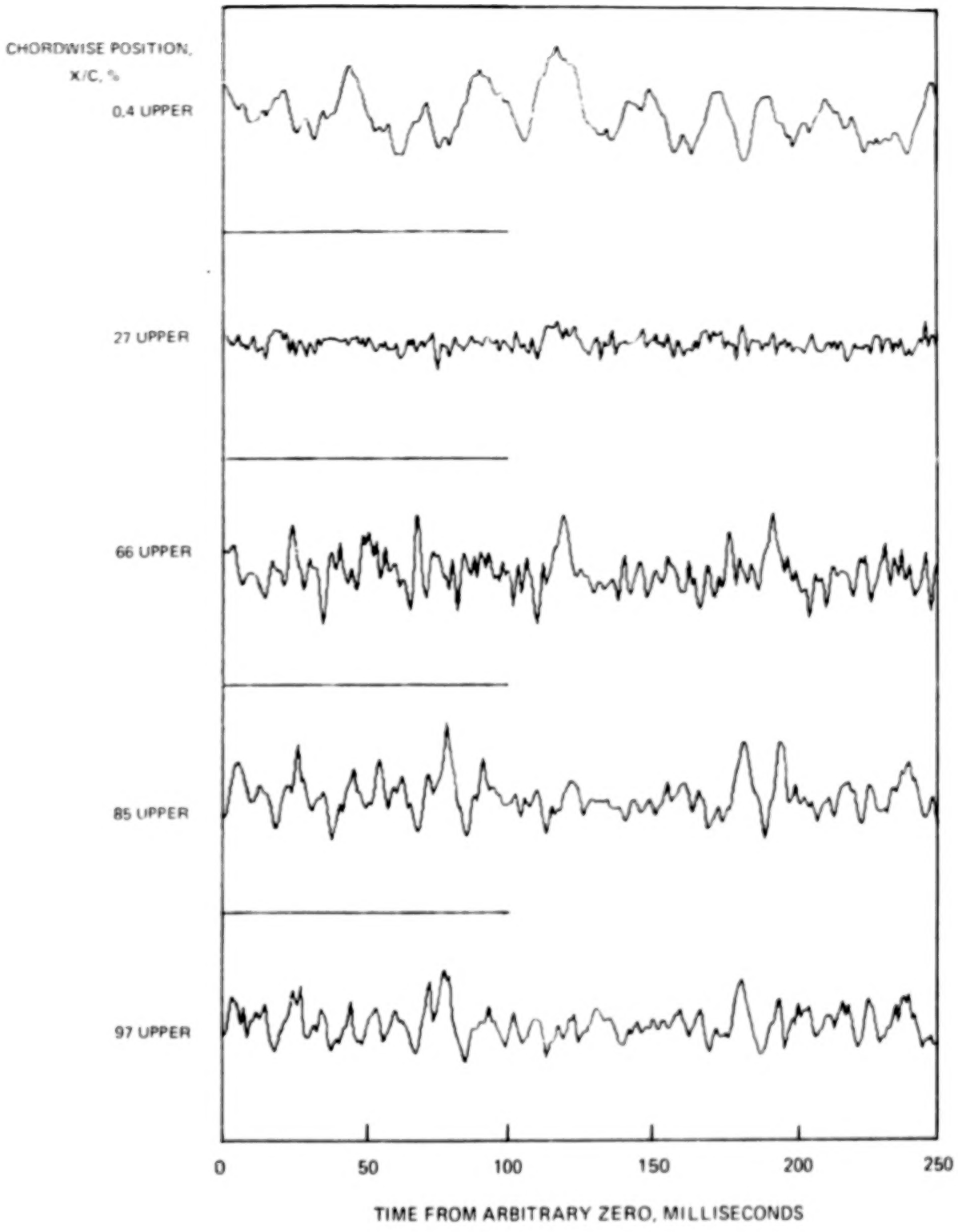

Figure 46 (Concluded) – (b) Forward and Aft Upper Surface

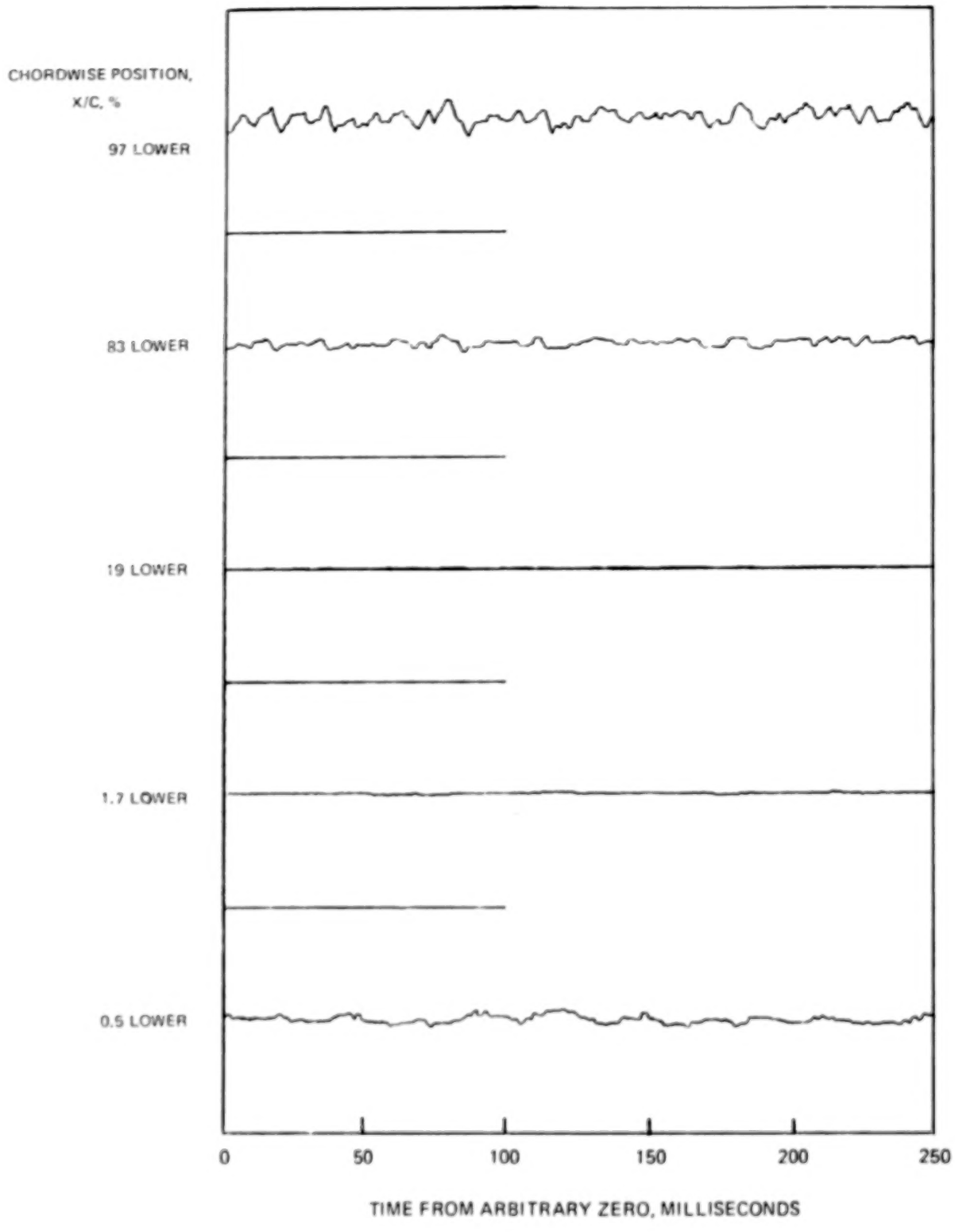

Figure 47 **Absolute–Level Pressure Fluctuations on a Chordwise Line Along the Lower Surface of a Steady Unswept NACA 0012 Airfoil at 0.30 Mach Number and 15° Angle of Attack.**

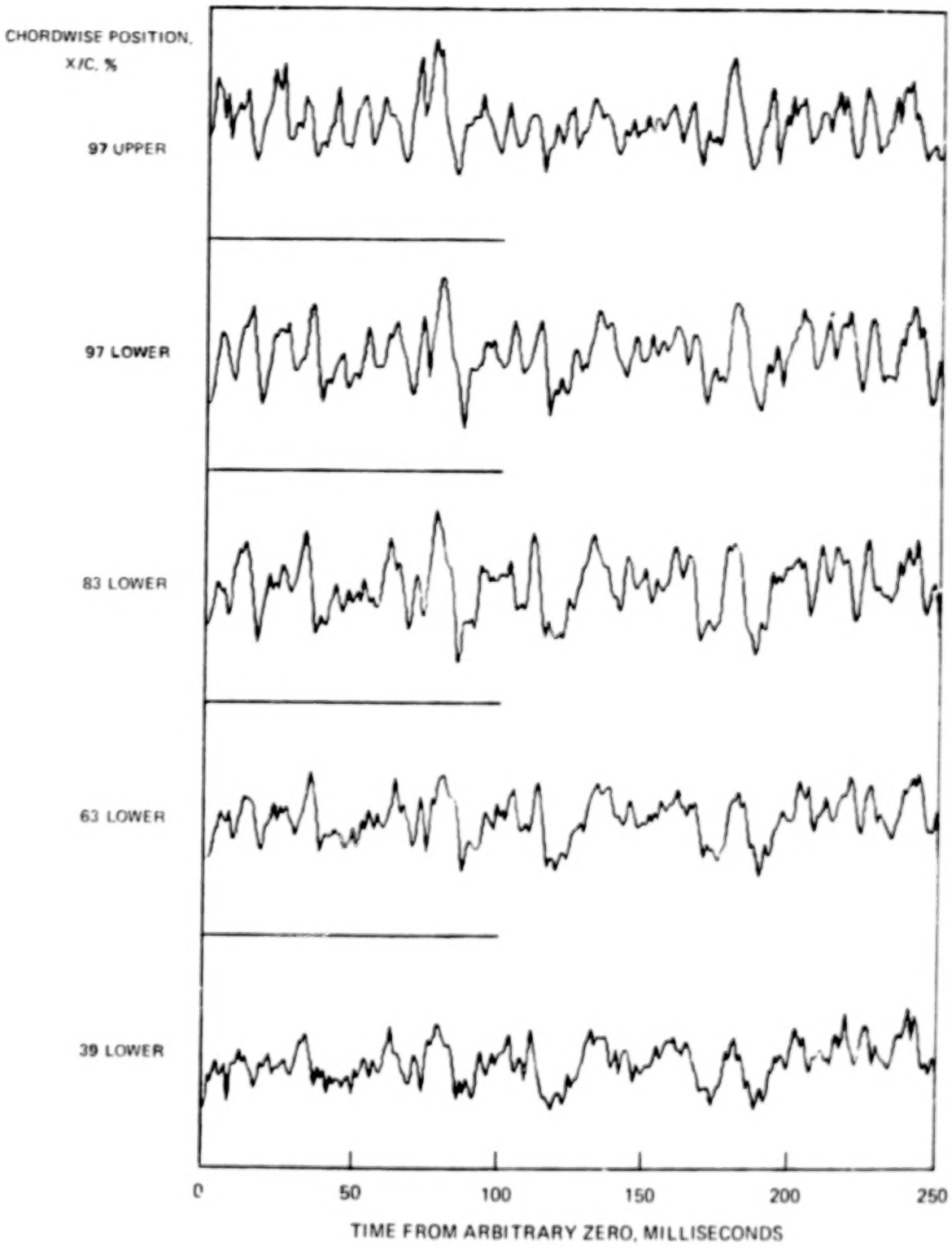

Figure 48 Self–Scaled Pressure Fluctuation on a Chordwise Line Along a Steady Unswept NACA 0012 Airfoil at 0.30 Mach Number and 15° Angle of Attack. (a) Aft Upper and Lower Surfaces

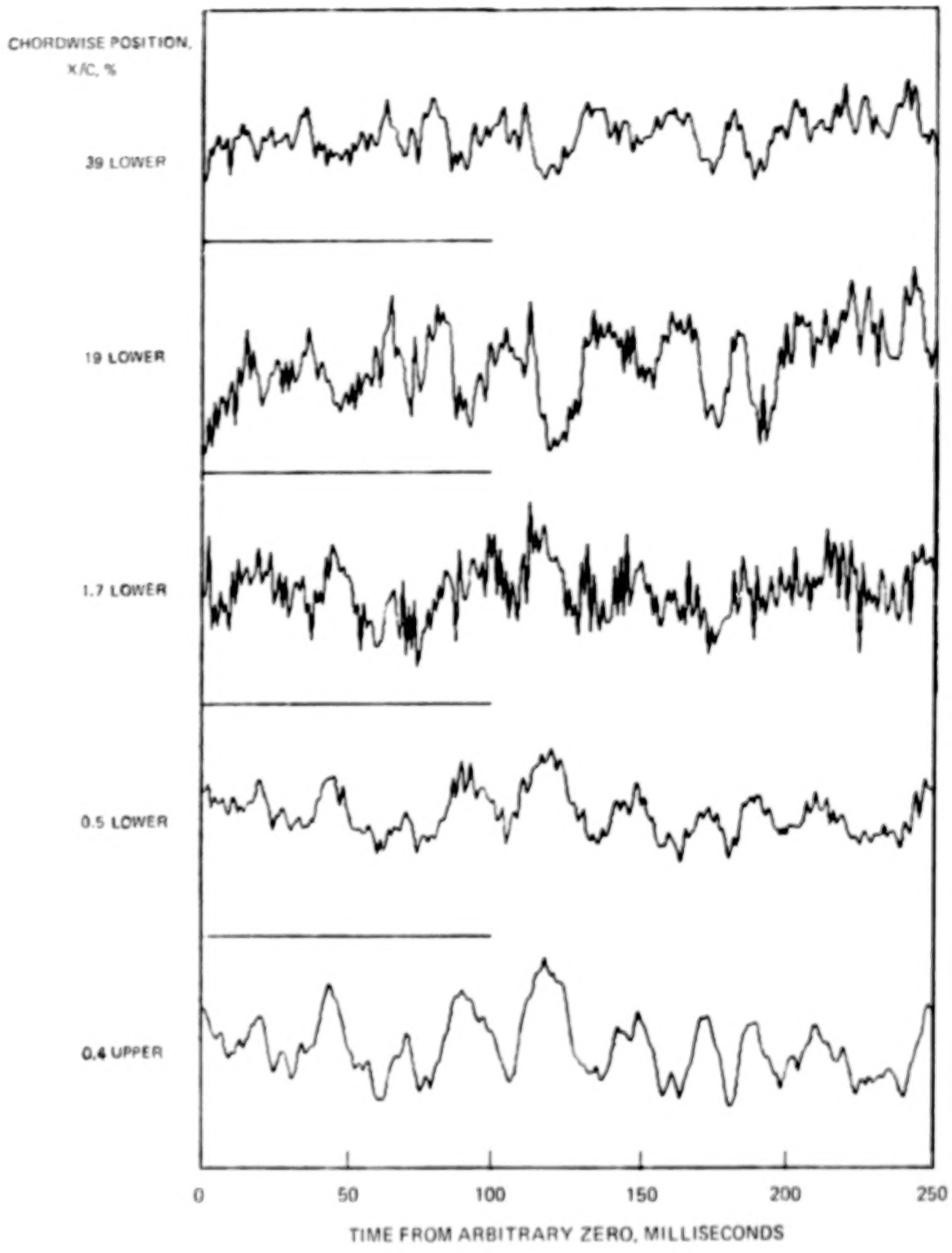

Figure 48 (Concluded)–(b) Forward Lower and Upper Surfaces

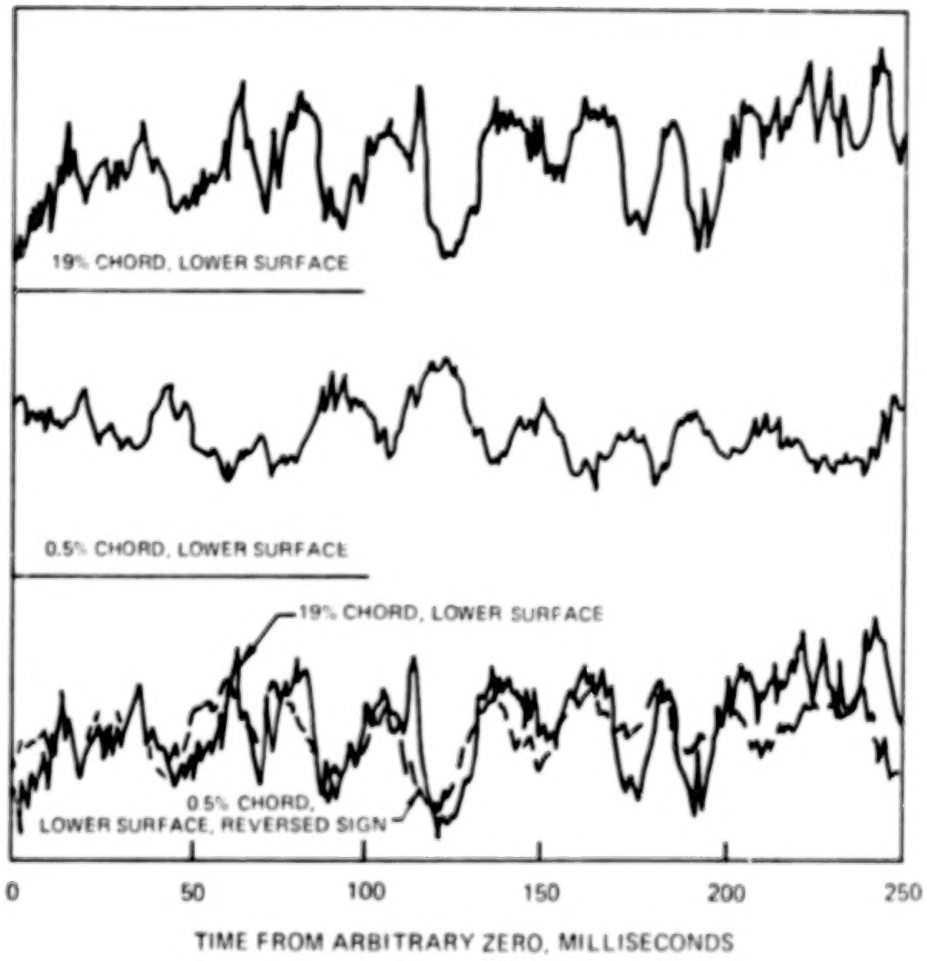

Figure 49 Phase Reversal of Self–Scaled Pressure Fluctuations on Forward Lower Surface of a Steady Unswept NACA 0012 Airfoil at 0.30 Mach Number and 15° Angle of Attack

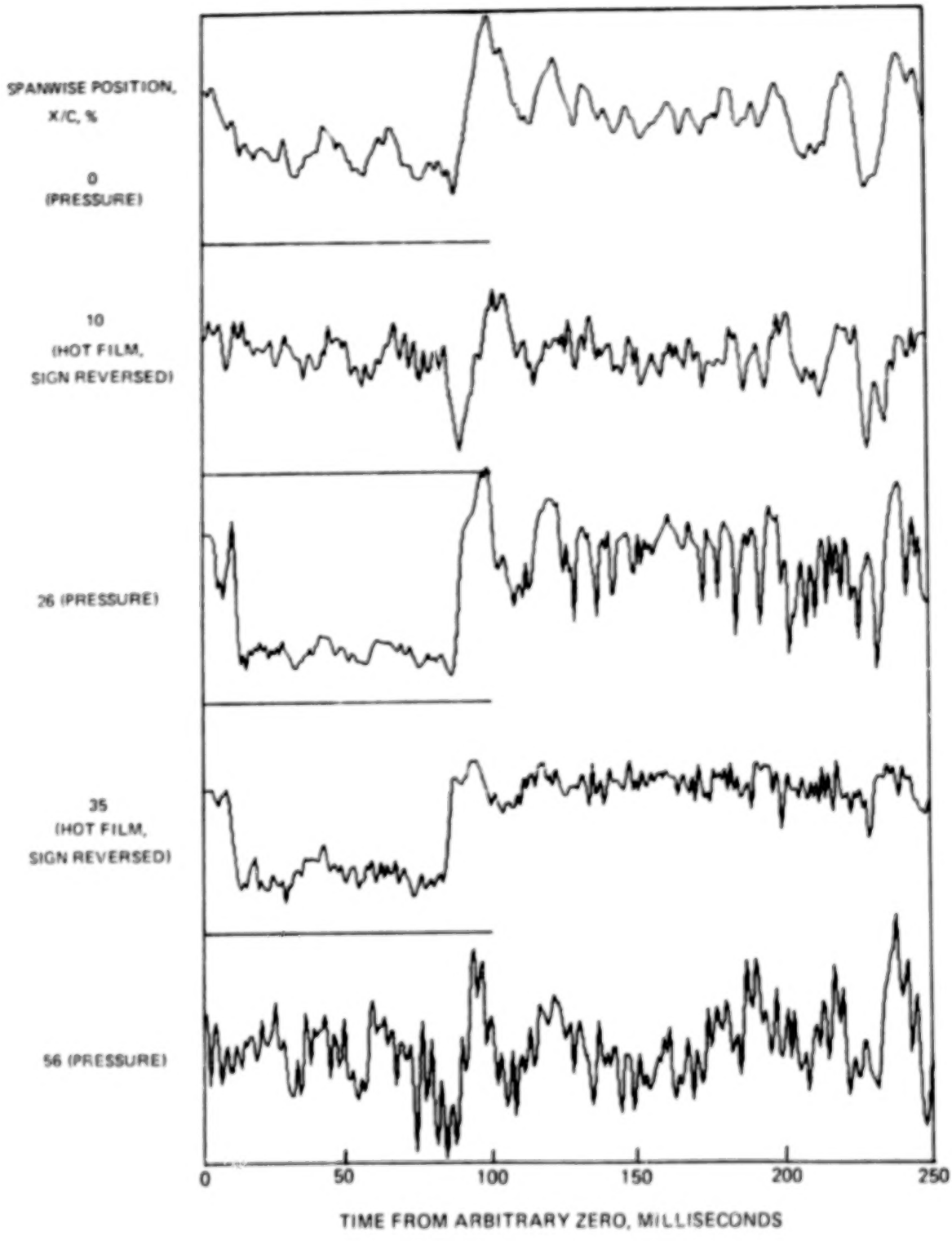

Figure 50 Self–Scaled Pressure and Heat Transfer Fluctuations on Spanwise Lines Along a Steady Unswept NACA 0012 Airfoil at 0.30 Mach Number and 15° Angle of Attack. Pressures at 0.4 % Chord, Hot Films at 2.1 % Chord, Upper Surface.

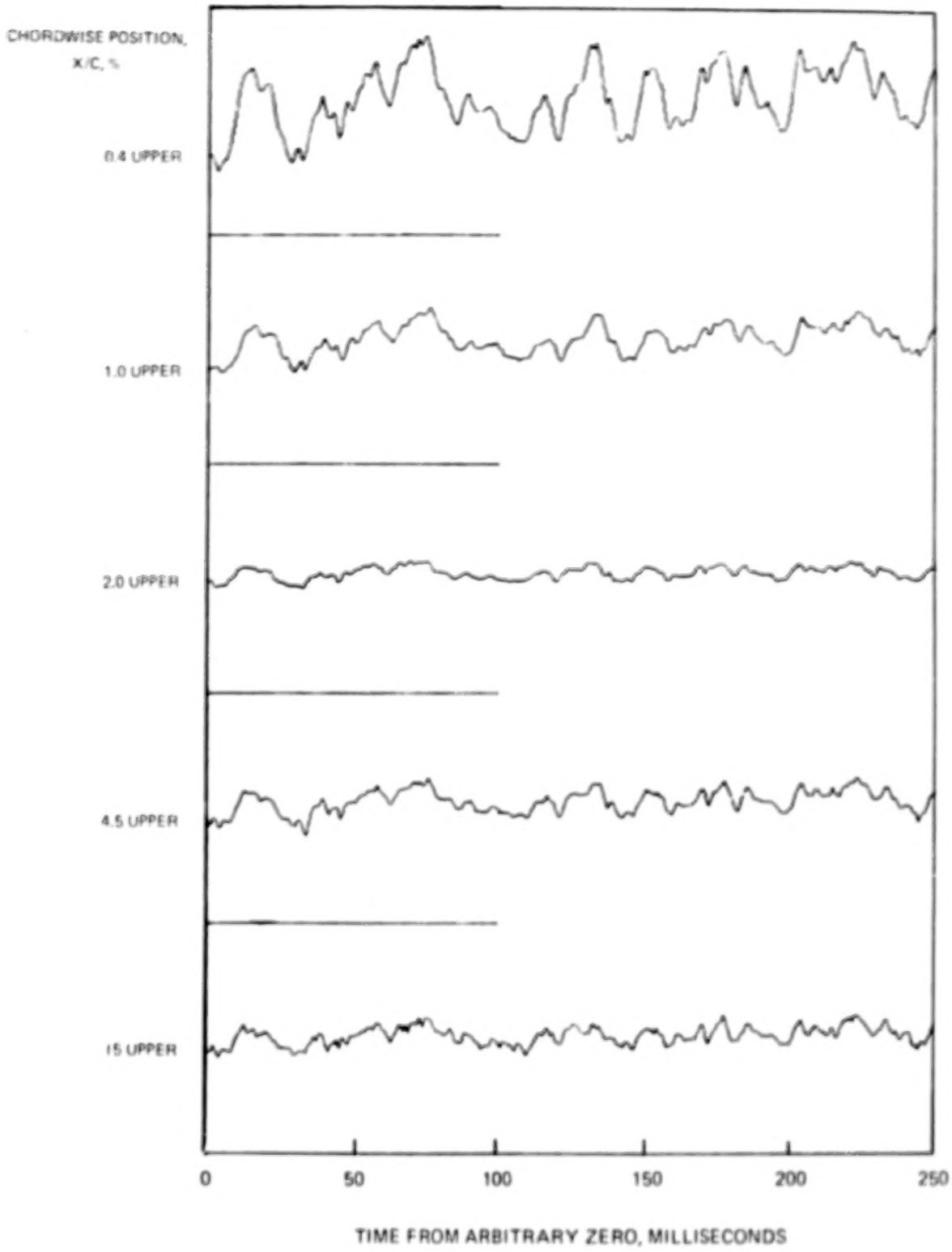

Figure 51 **Absolute–Level Pressure Fluctuations on a Chordwise Line Along a Steady Unswept NACA 0012 Airfoil at 0.30 Mach Number and 19° Angle of Attack. (a) Forward Upper Surface**

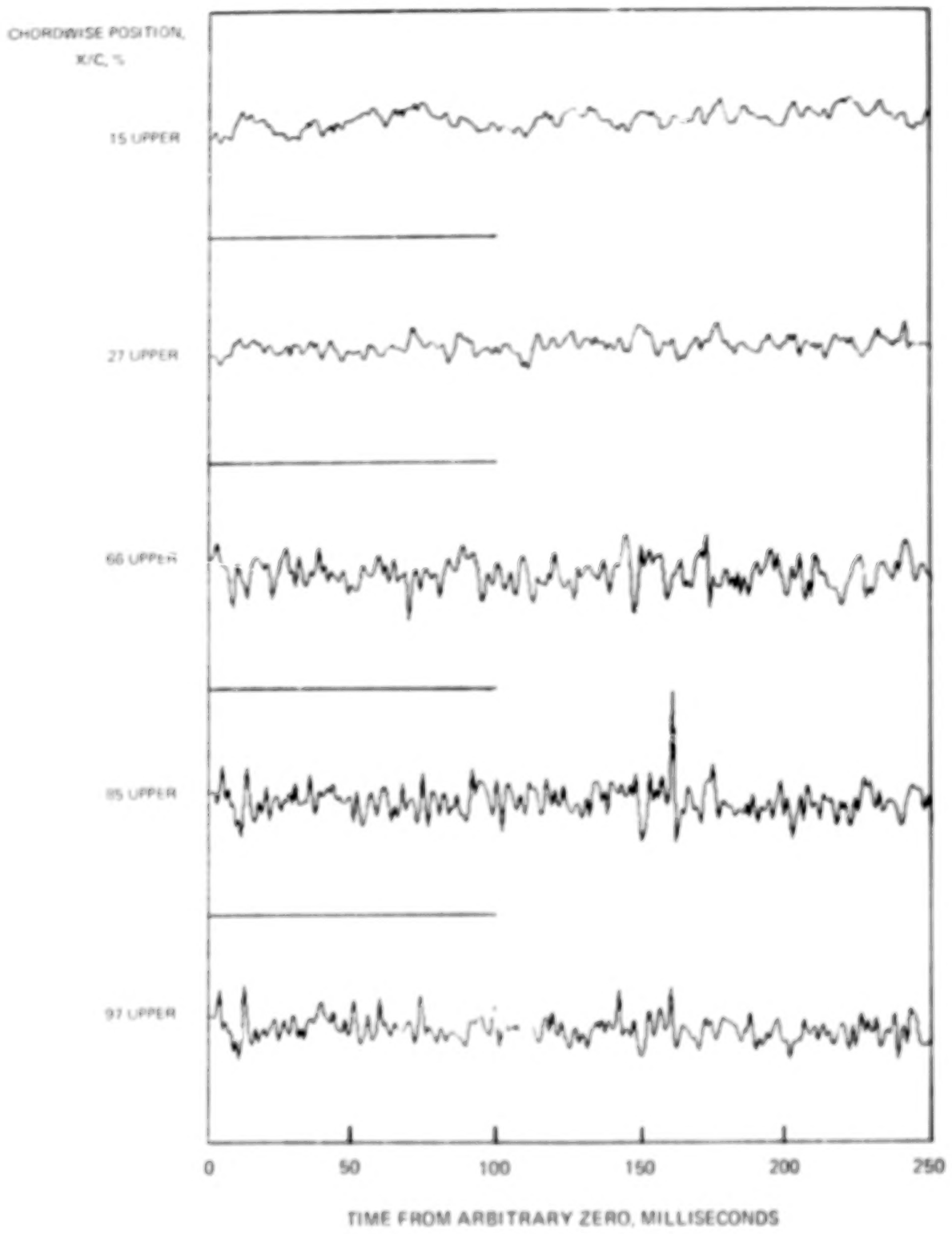

Figure 51 (Concluded) – (b) Aft Upper Surface

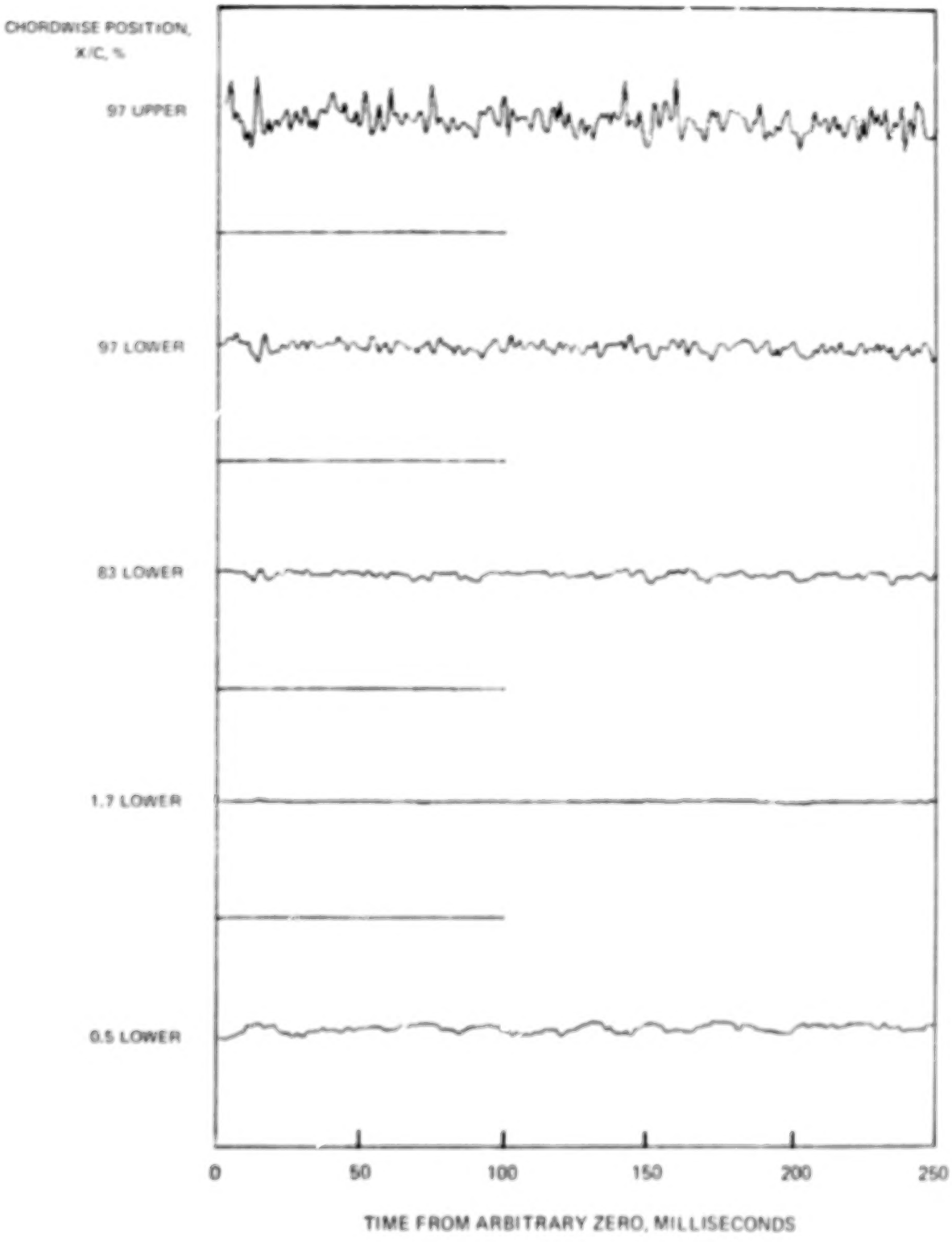

Figure 52 Absolute–Level Pressure Fluctuations on a Chordwise Line Along the Lower Surface of a Steady Unswept NACA 0012 Airfoil at 0.30 Mach Number and 19° Angle of Attack.

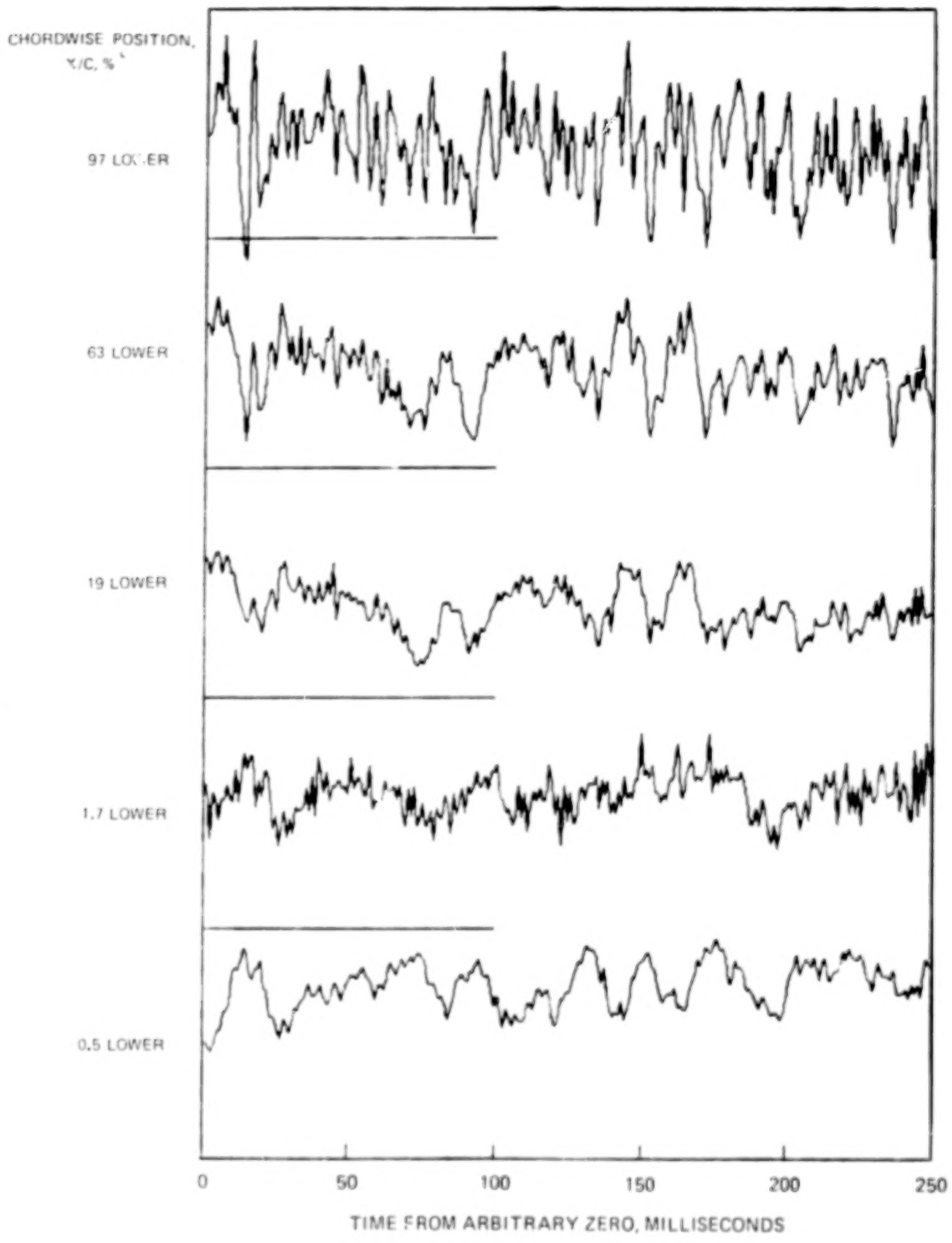

Figure 53 Self–Scaled Pressure Fluctuations on a Chordwise Line Along the Lower Surface of a Steady Unswept NACA 0012 Airfoil at 0.30 Mach Number and 19° Angle of Attack

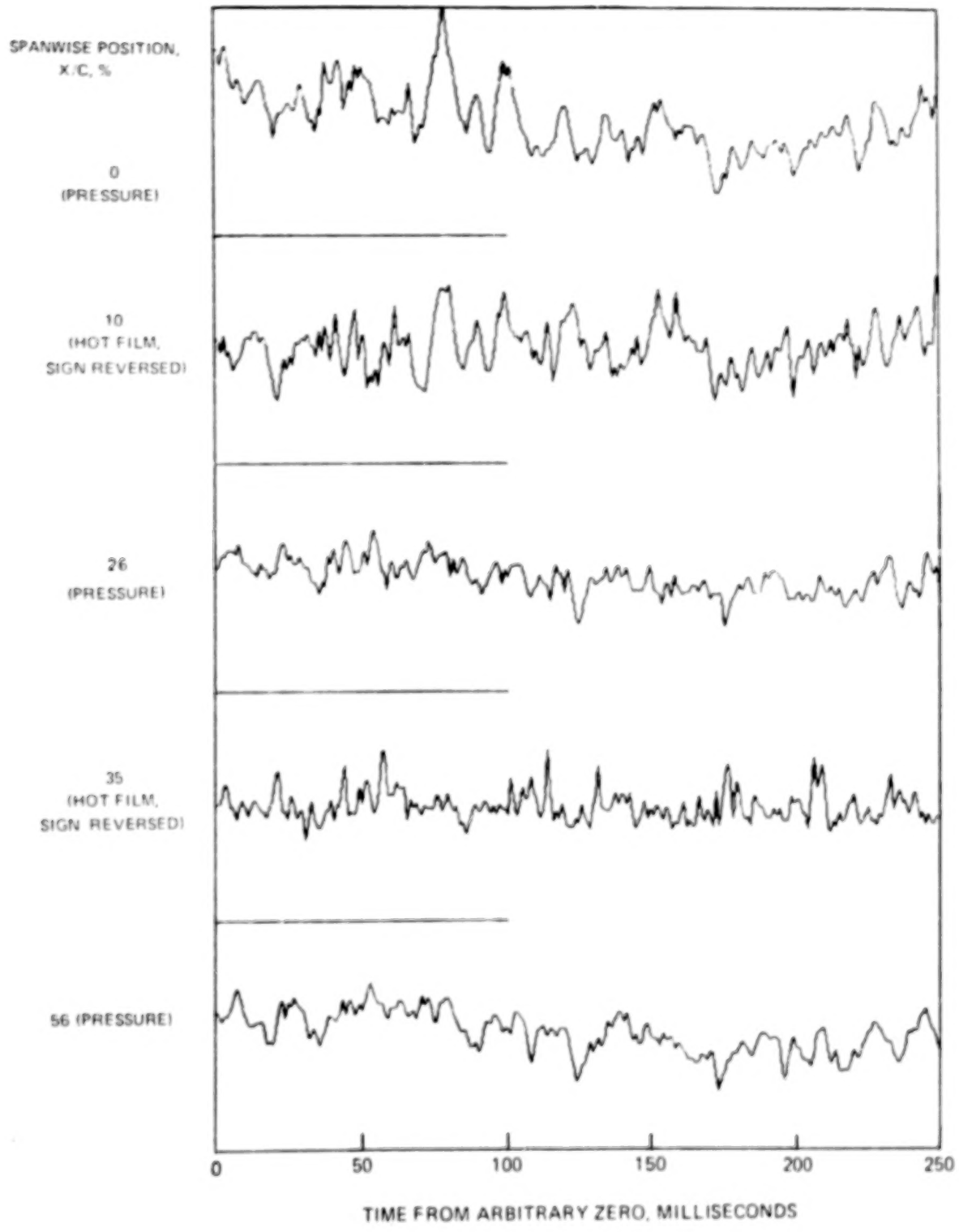

Figure 54 Self–Scaled Pressure and Heat Transfer Fluctuations on Spanwise Lines Along a Steady Unswept NACA 0012 Airfoil at 0.30 Mach Number and 19° Angle of Attack. Pressures at 0.4 % Chord, Hot Films at 2.1 % Chord, Upper Surface.

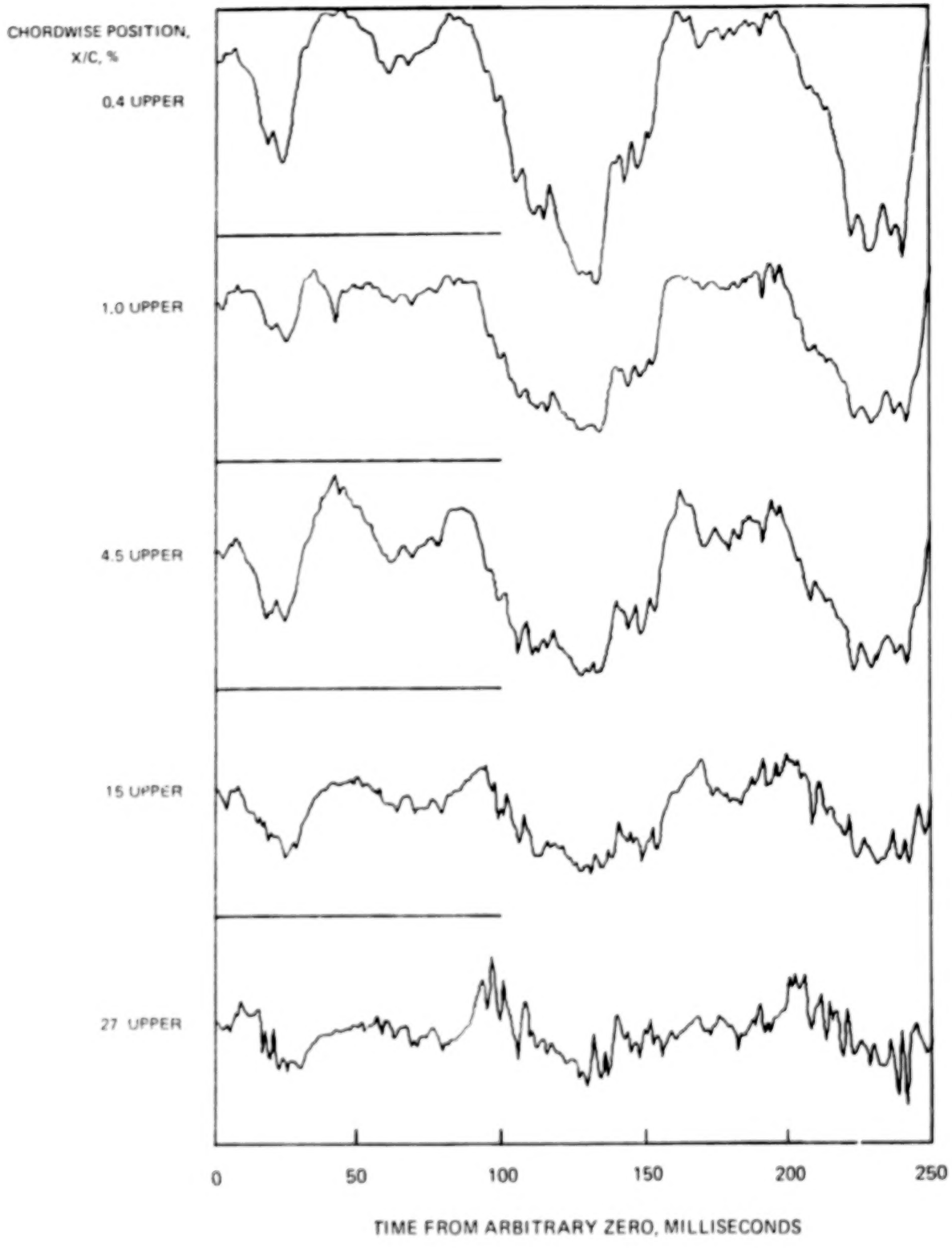

Figure 55 Absolute–Level Pressure Fluctuations on a Chordwise Line Along a Steady Unswept NACA 0012 Airfoil at 0.40 Mach Number and 12° Angle of Attack. (a) Forward Upper Surface

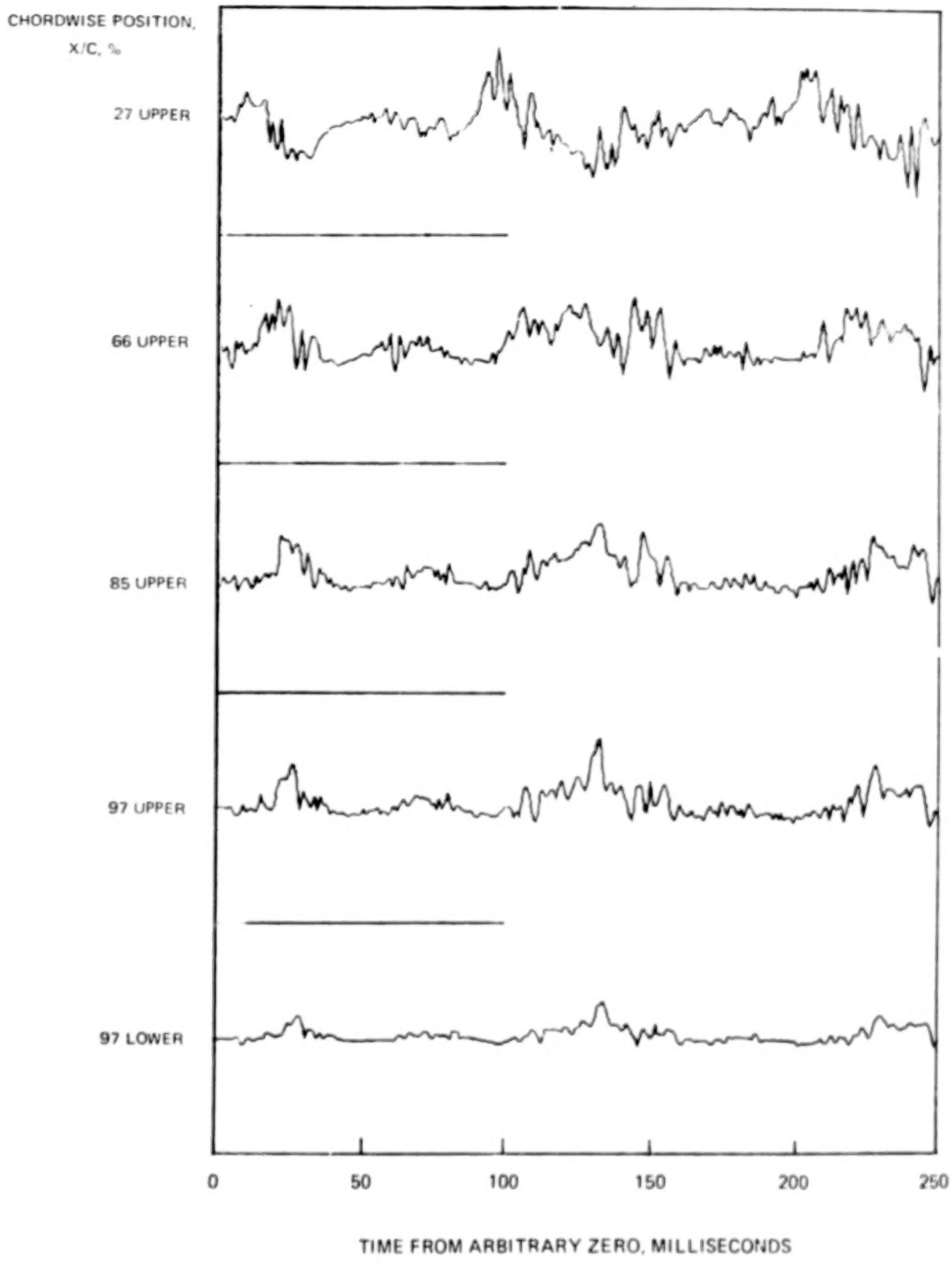

Figure 55 (Concluded) – (b) Aft Upper and Lower Surfaces

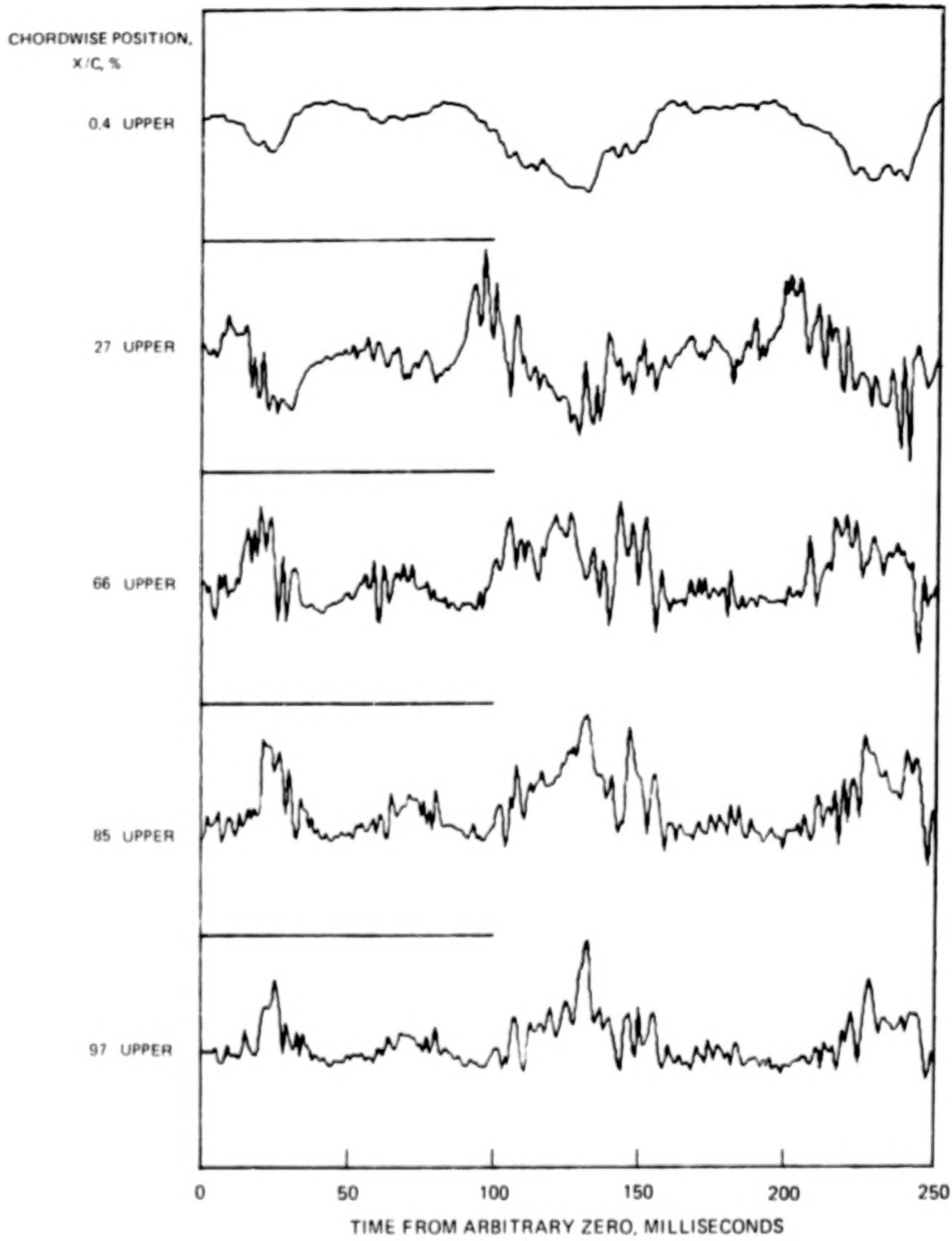

Figure 56 Self–Scaled Pressure Fluctuations on a Chordwise Line Along the Upper Surface a Steady Unswept NACA 0012 Airfoil at 0.40 Mach Number and 12° Angle of Attack.

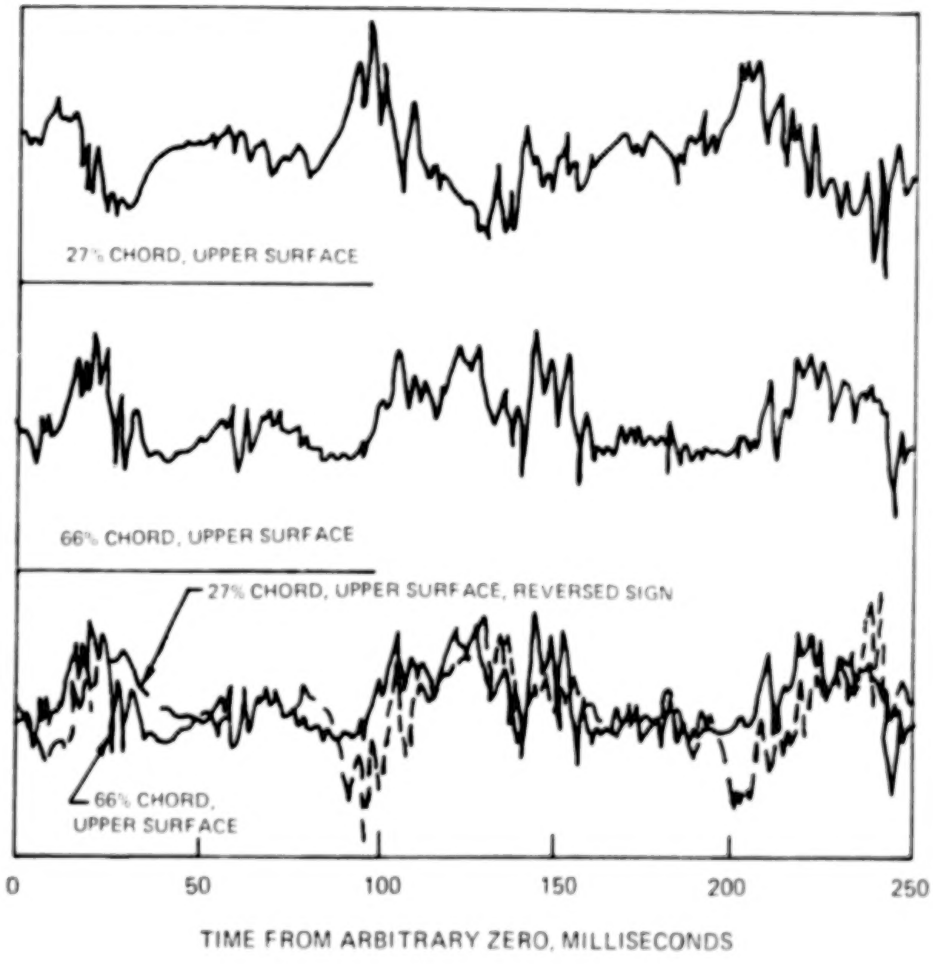

Figure 57 Phase Reversal of Self–Scaled Pressure Fluctuations on Mid–Chord Upper Surface of a Steady Unswept NACA 0012 Airfoil at 0.40 Mach Number and 12° Angle of Attack

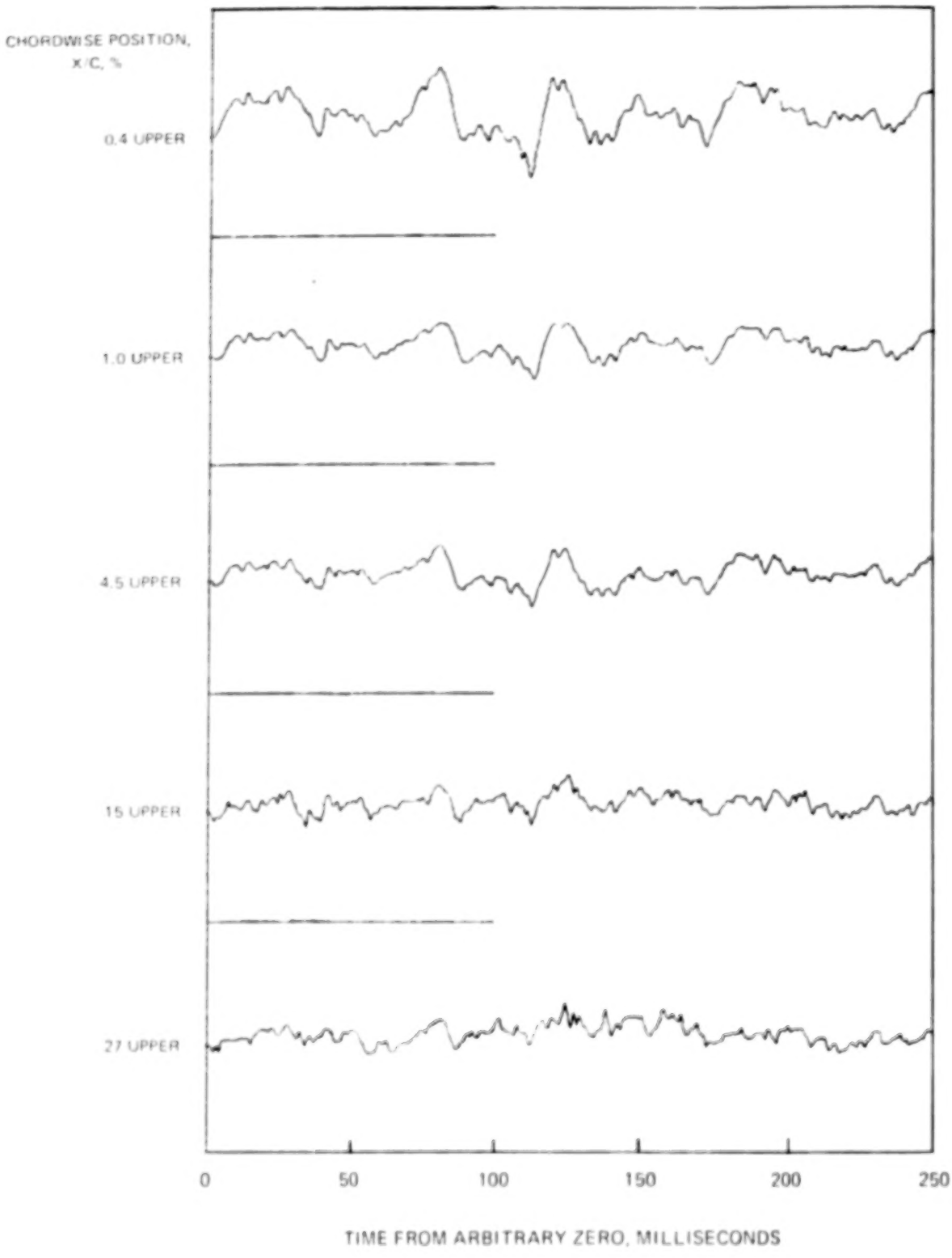

Figure 58 Absolute–Level Pressure Fluctuations on a Chordwise Line Along a Steady Unswept NACA 0012 Airfoil at 0.40 Mach Number and 14° Angle of Attack. (a) Forward Upper Surface

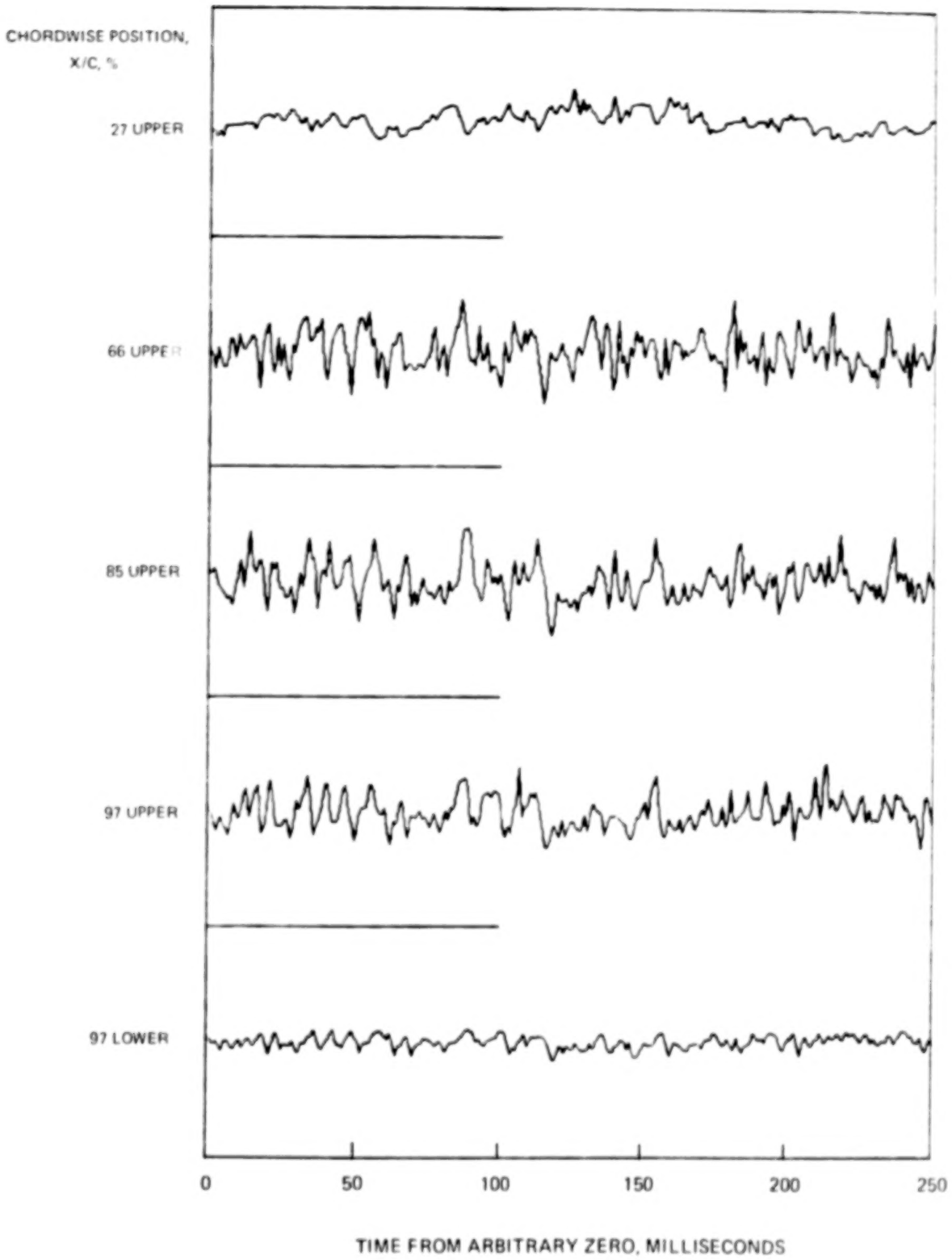

Figure 58 (Concluded)– (b) Aft Upper and Lower Surfaces

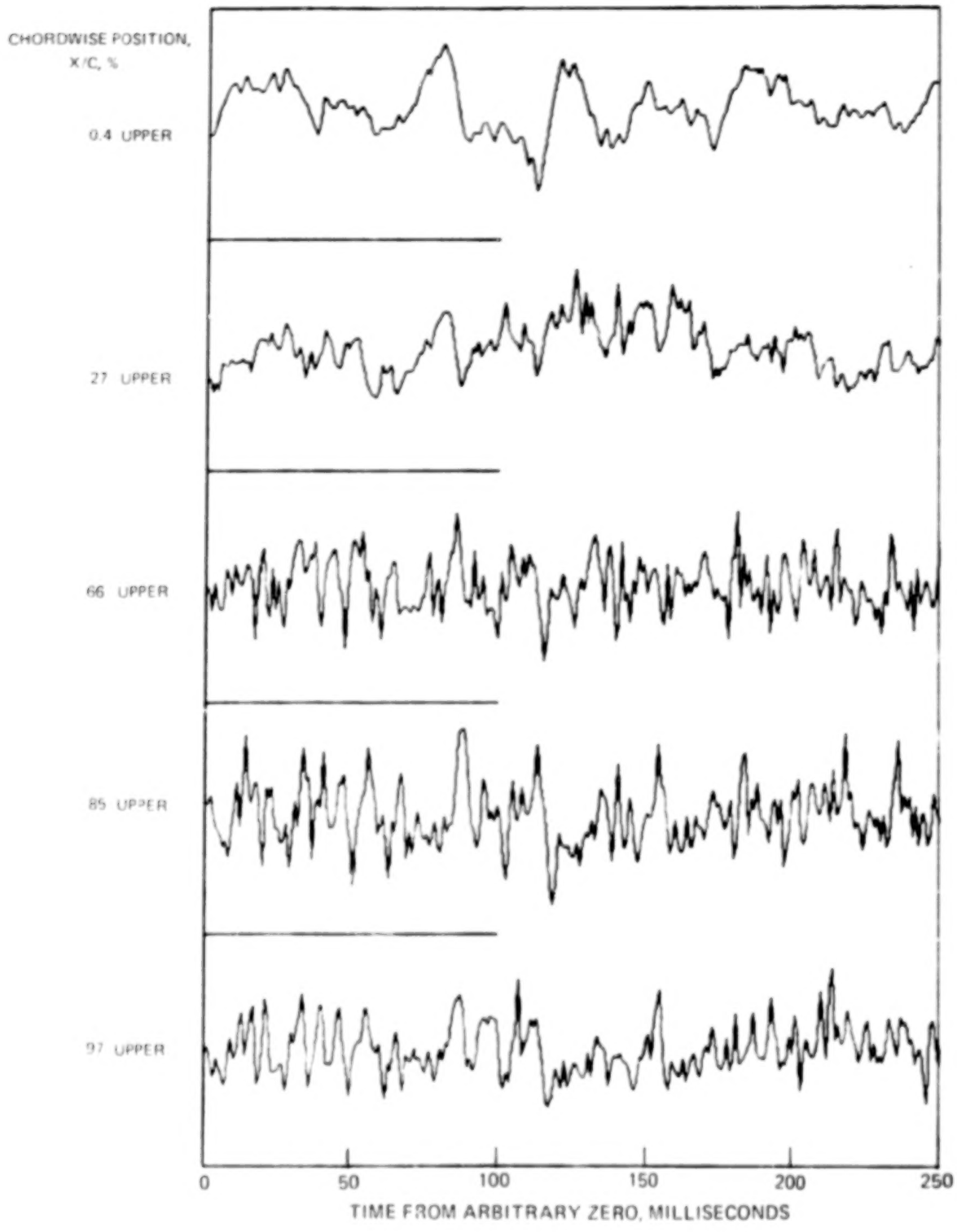

Figure 59 Self–Scaled Pressure Fluctuations on a Chordwise Line Along a Steady Unswept NACA 0012 Airfoil at 0.40 Mach Number and 14° Angle of Attack.
(a) Upper Surface

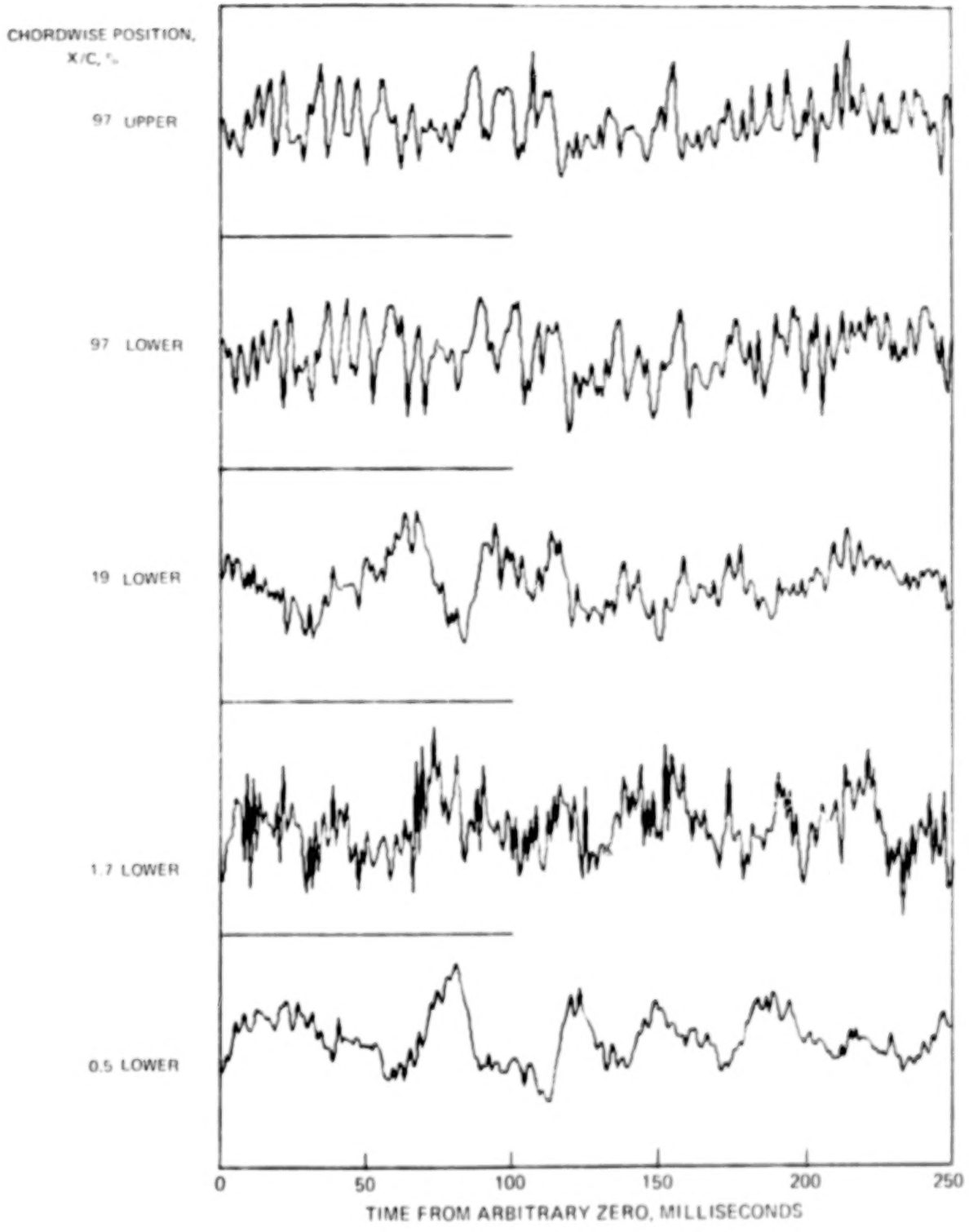

Figure 59 (Concluded)– (b) Lower and Aft Upper Surfaces

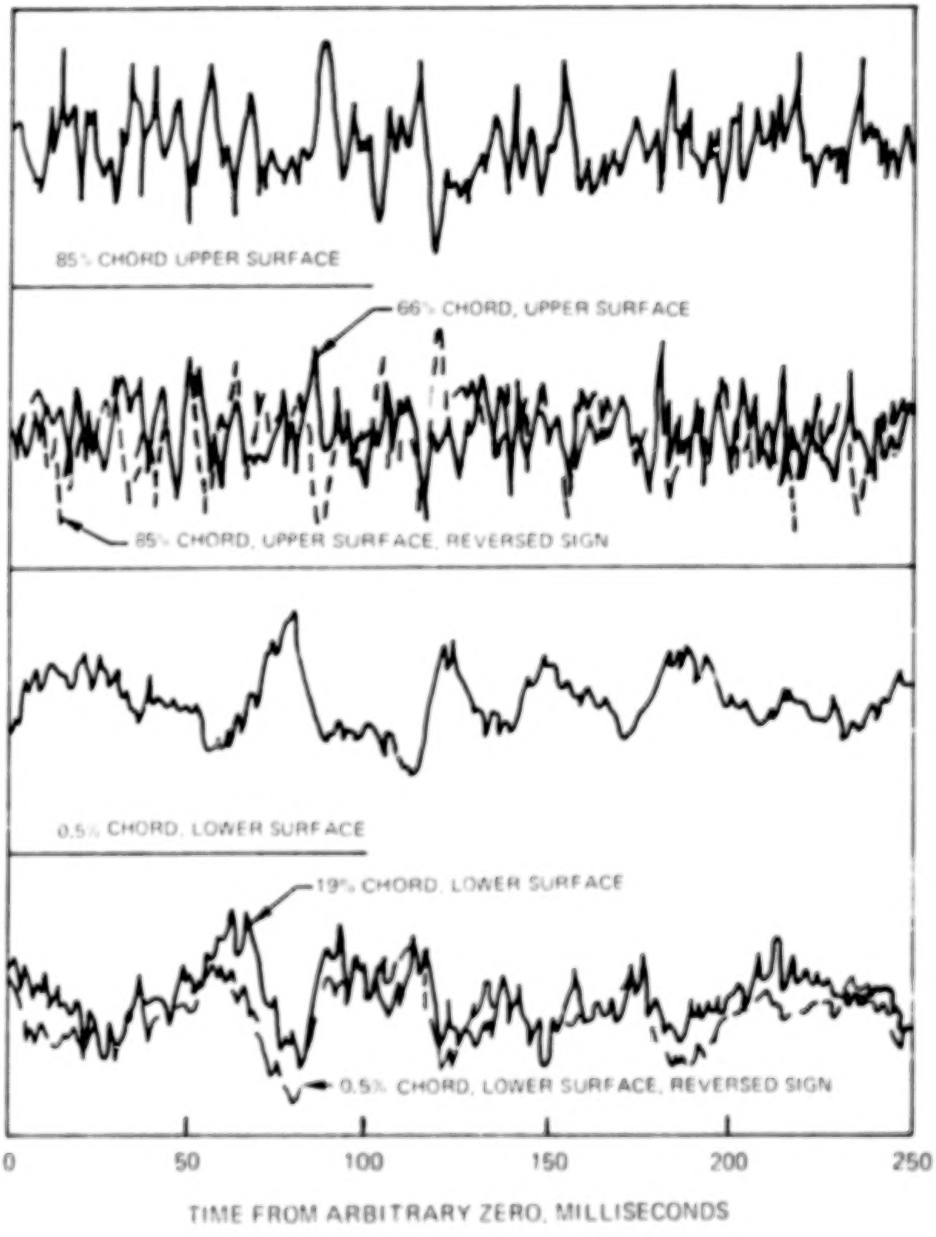

Figure 60 Phase Reversal of Self–Scaled Pressure Fluctuations on Aft Upper Surface and Forward Lower Surface of a Steady Unswept NACA 0012 Airfoil at 0.40 Mach Number and 14° Angle of Attack.

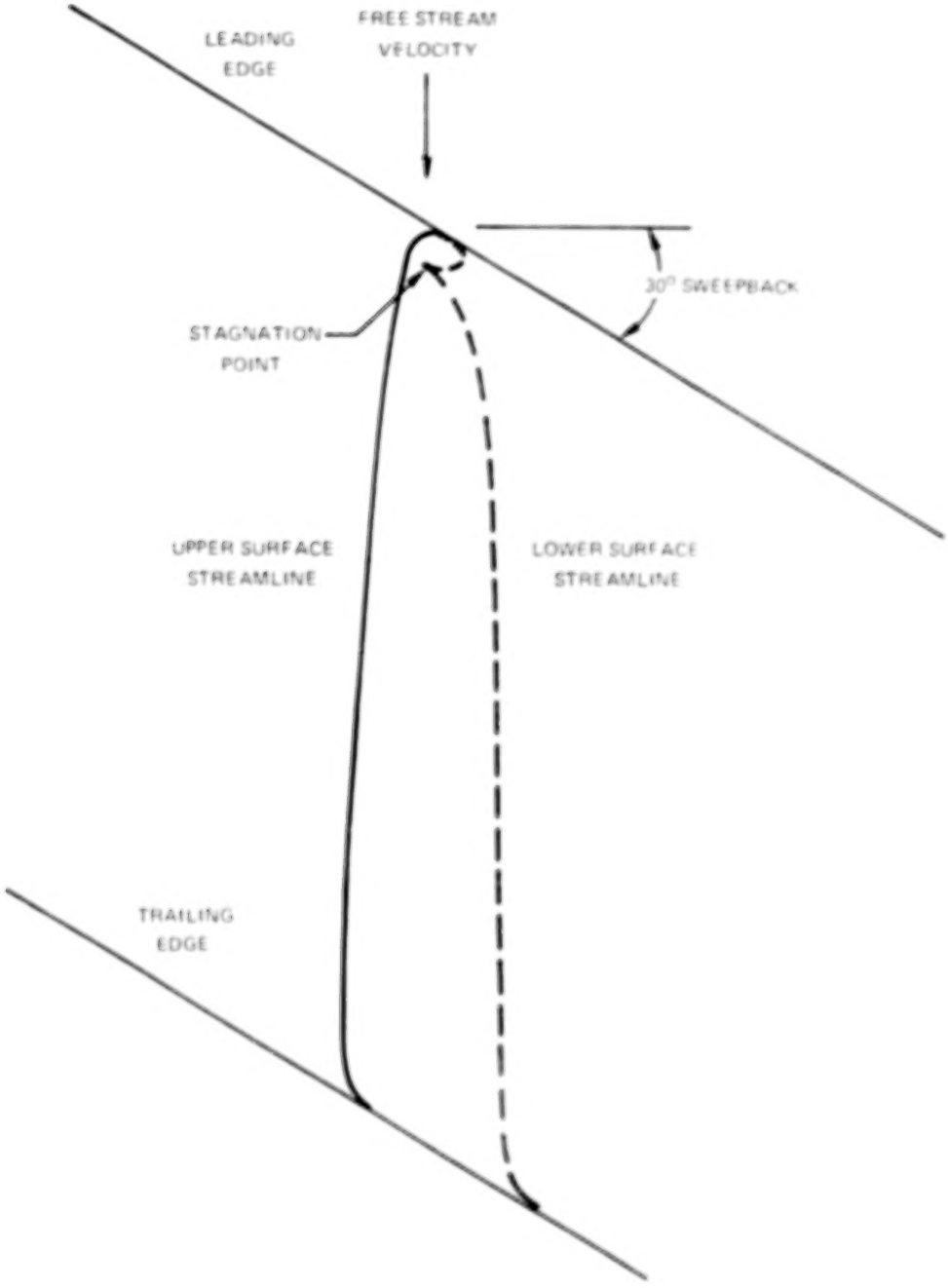

Figure 61 Calculated Streamline Shapes at Edge of Boundary Layer for NACA 0012 Airfoil with 30° Sweepback. Incompressible Flow, Lift Coefficient = 1.0 Referenced to Streamwise Flow.

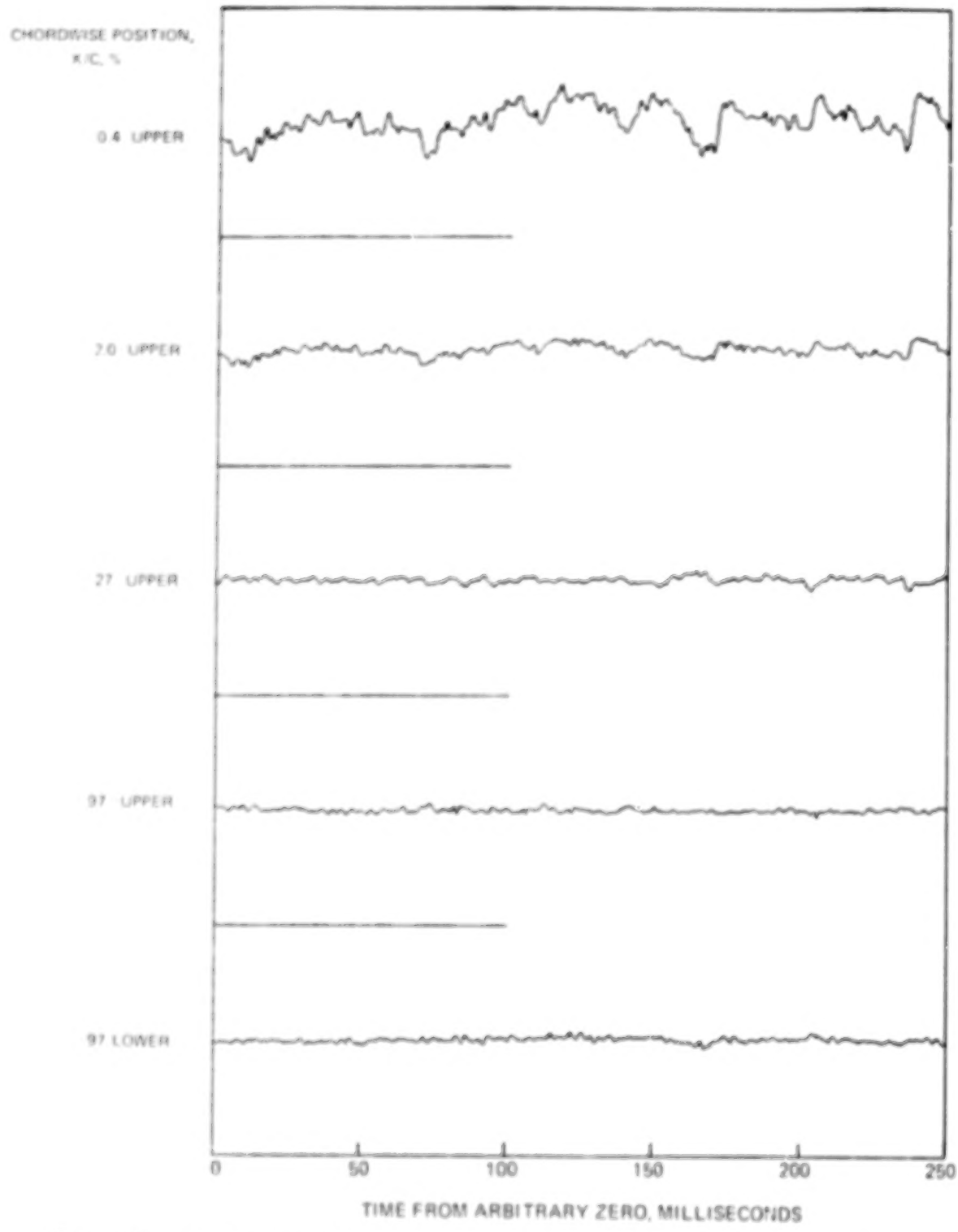

Figure 62 **Absolute–Level Pressure Fluctuations on a Line Normal to the Leading Edge of a Steady 30° Swept NACA 0012 Airfoil at 0.30 Mach Number and 15° Angle of Attack Normal to the Leading Edge.**

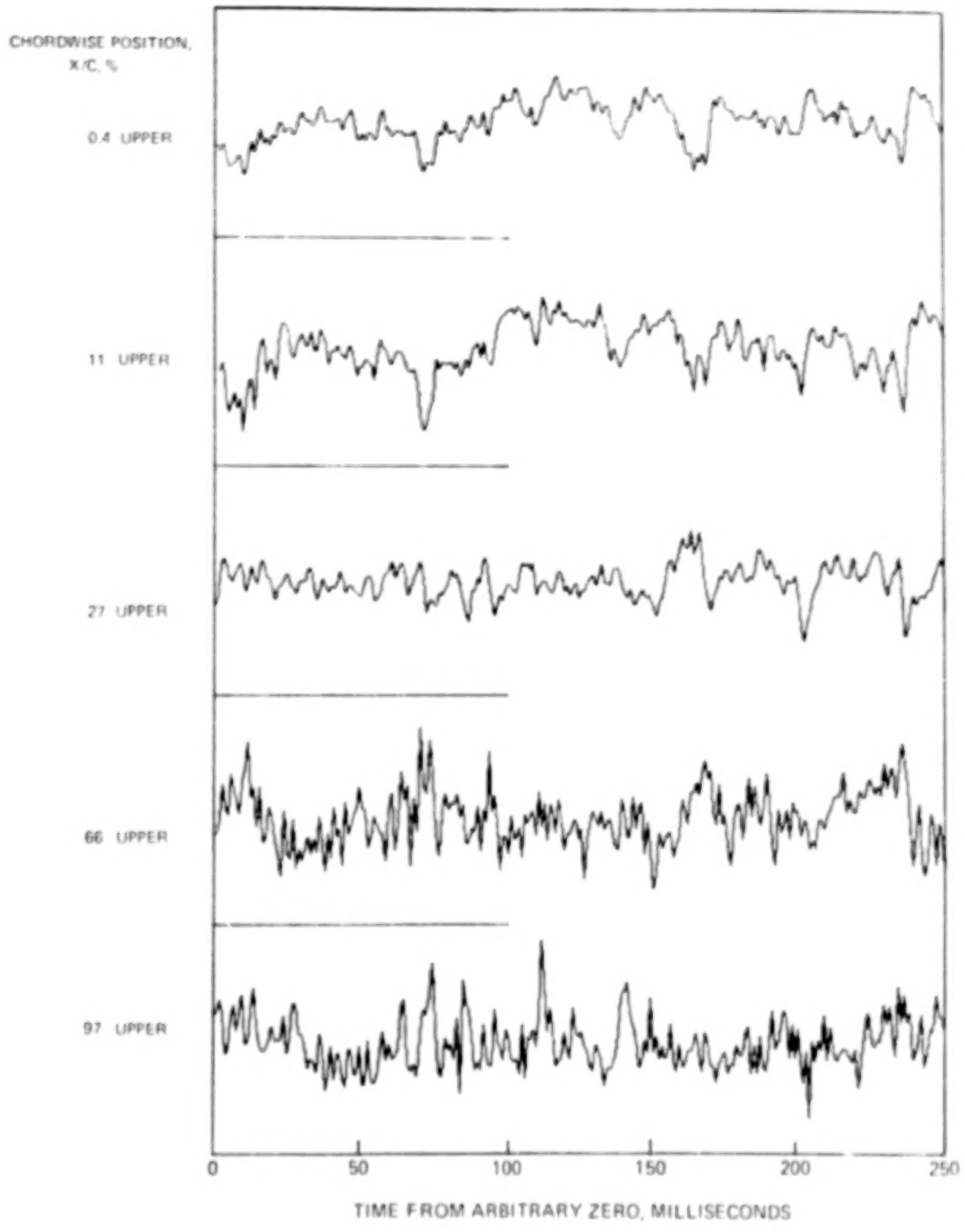

Figure 63 Self–Scaled Pressure Fluctuations on a Line Normal to the Leading Edge of a Steady 30° Swept NACA 0012 Airfoil at 0.30 Mach Number and 15° Angle of Attack Normal to Leading Edge. (a) Upper Surface

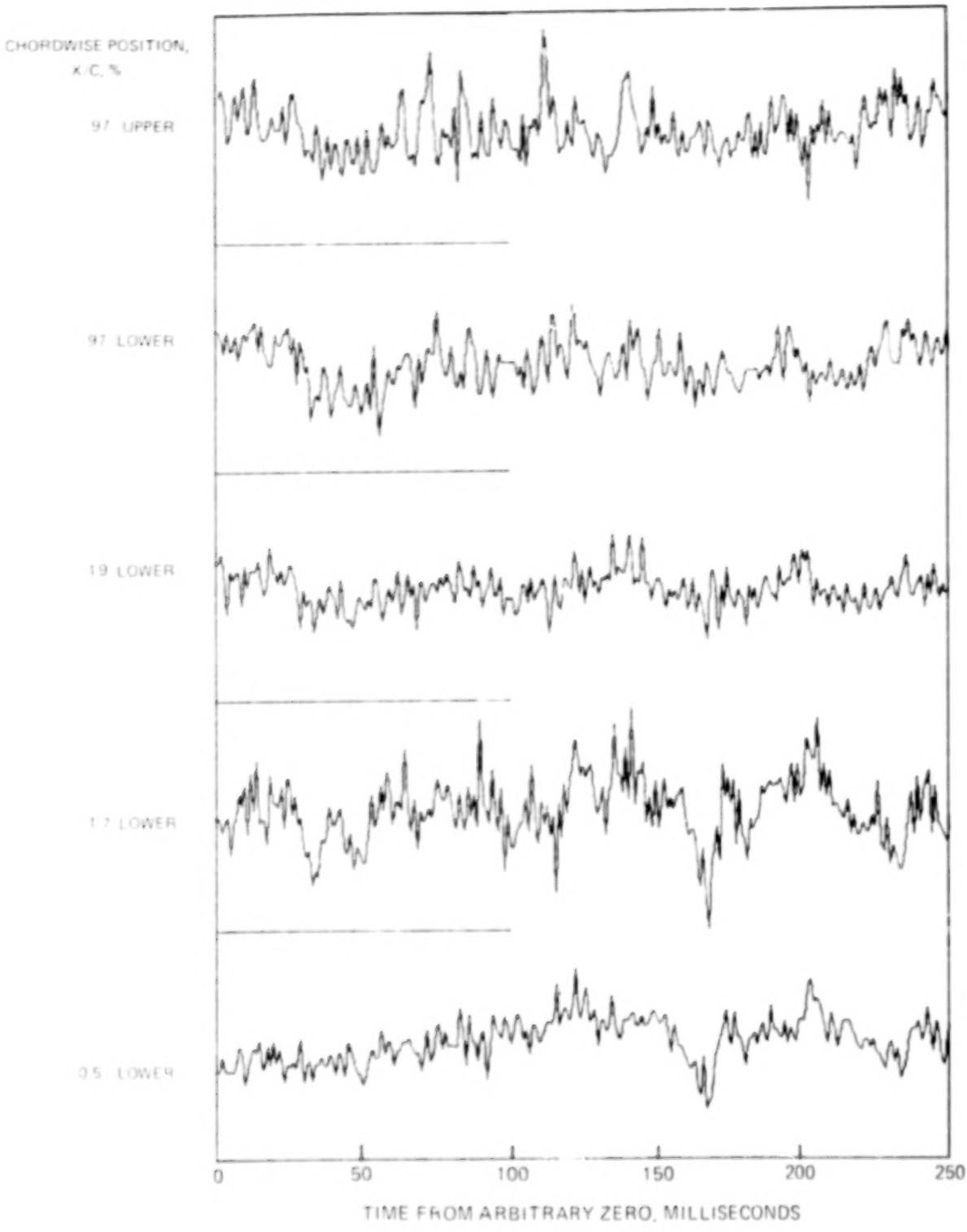

Figure 63 (Concluded) – (b) Lower and Aft Upper Surfaces

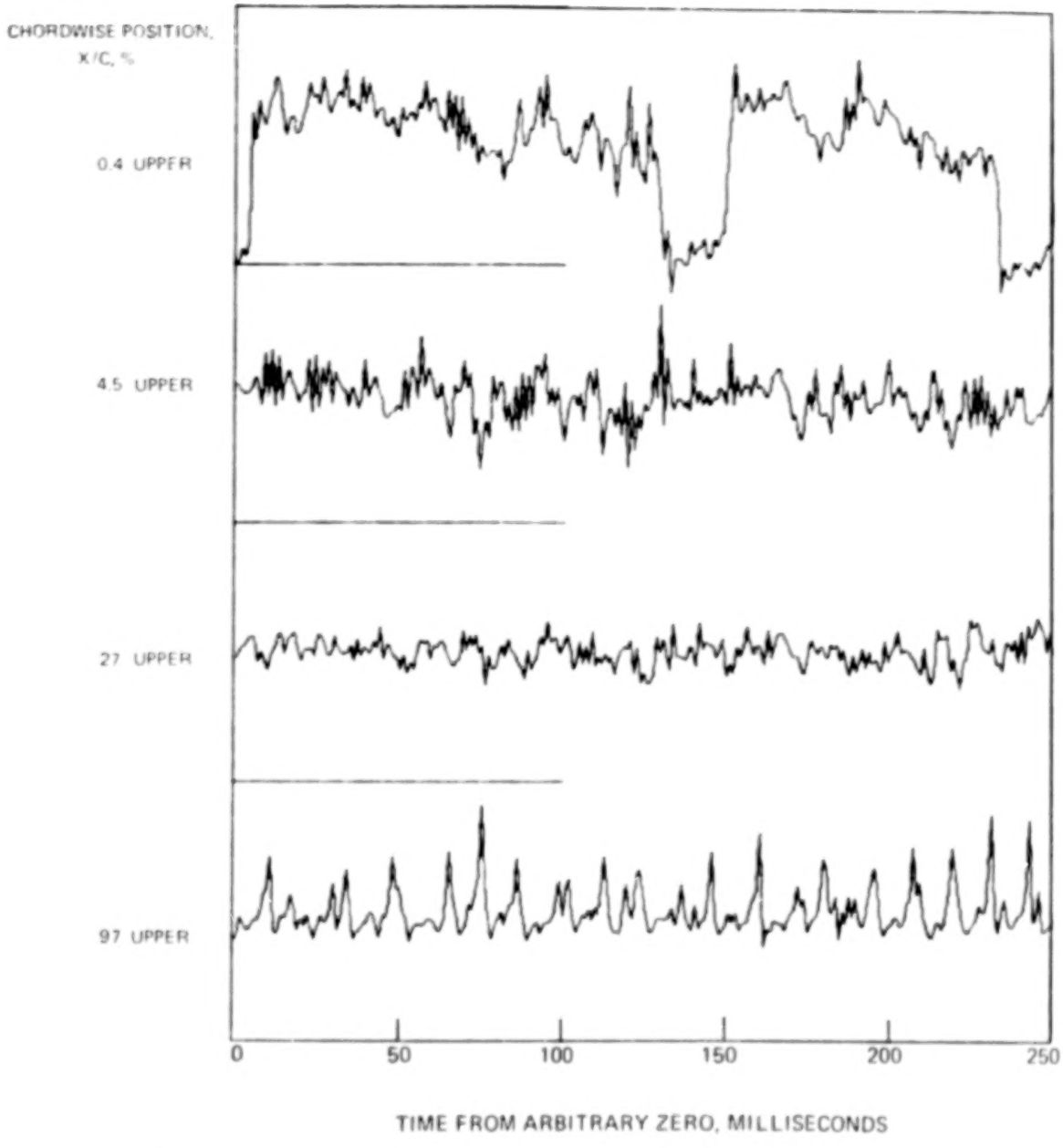

Figure 64 Absolute—Level Pressure Fluctuations on Lines Parallel to the Free Stream Along the Upper Surface of a 30° Swept NACA 0012 Airfoil at 0.30 Mach Number and 20° Angle of Attack Normal to the Leading Edge. (a) Full Chord Length

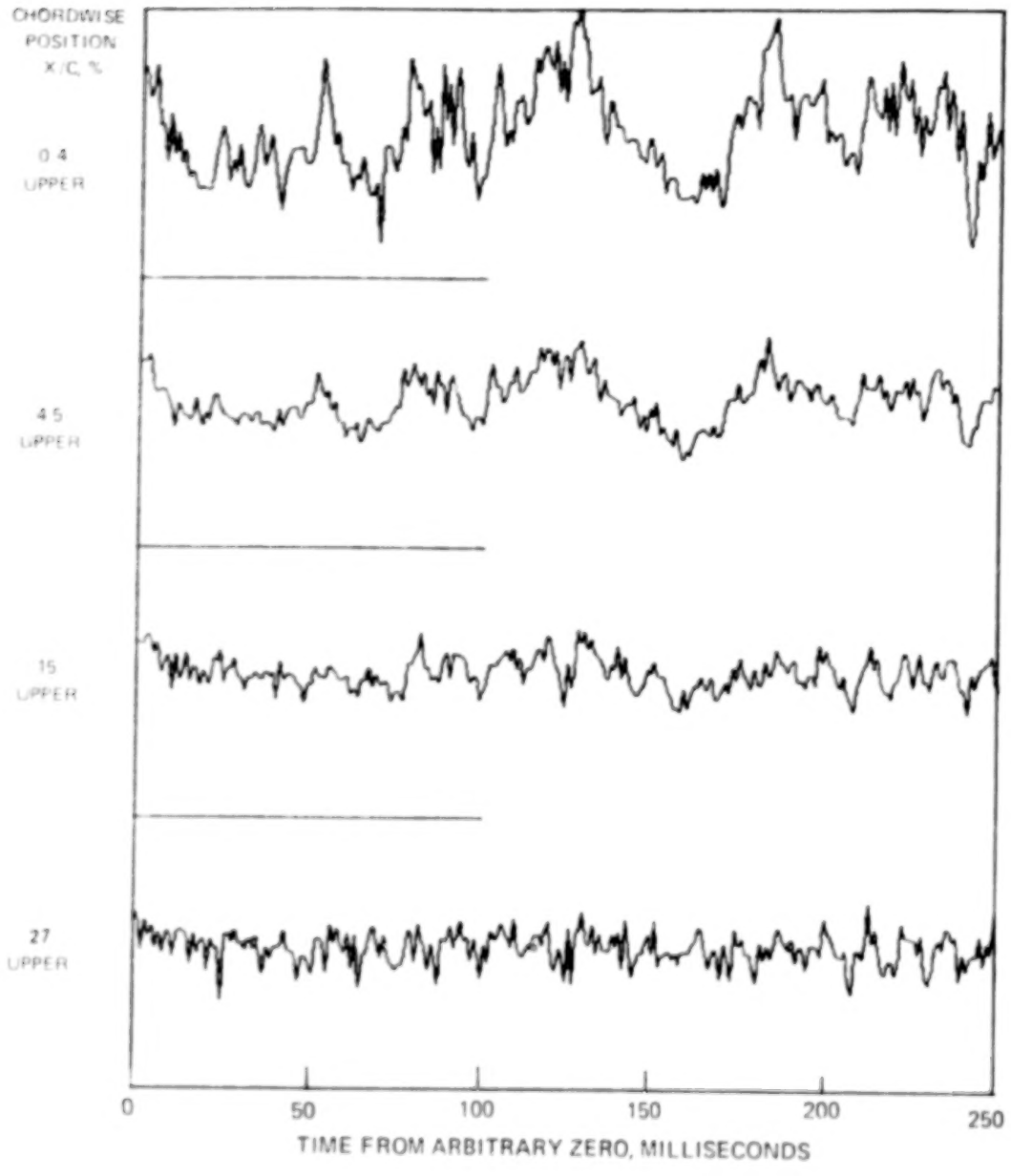

Figure 64 (Concluded) (b) Line Normal to Leading Edge

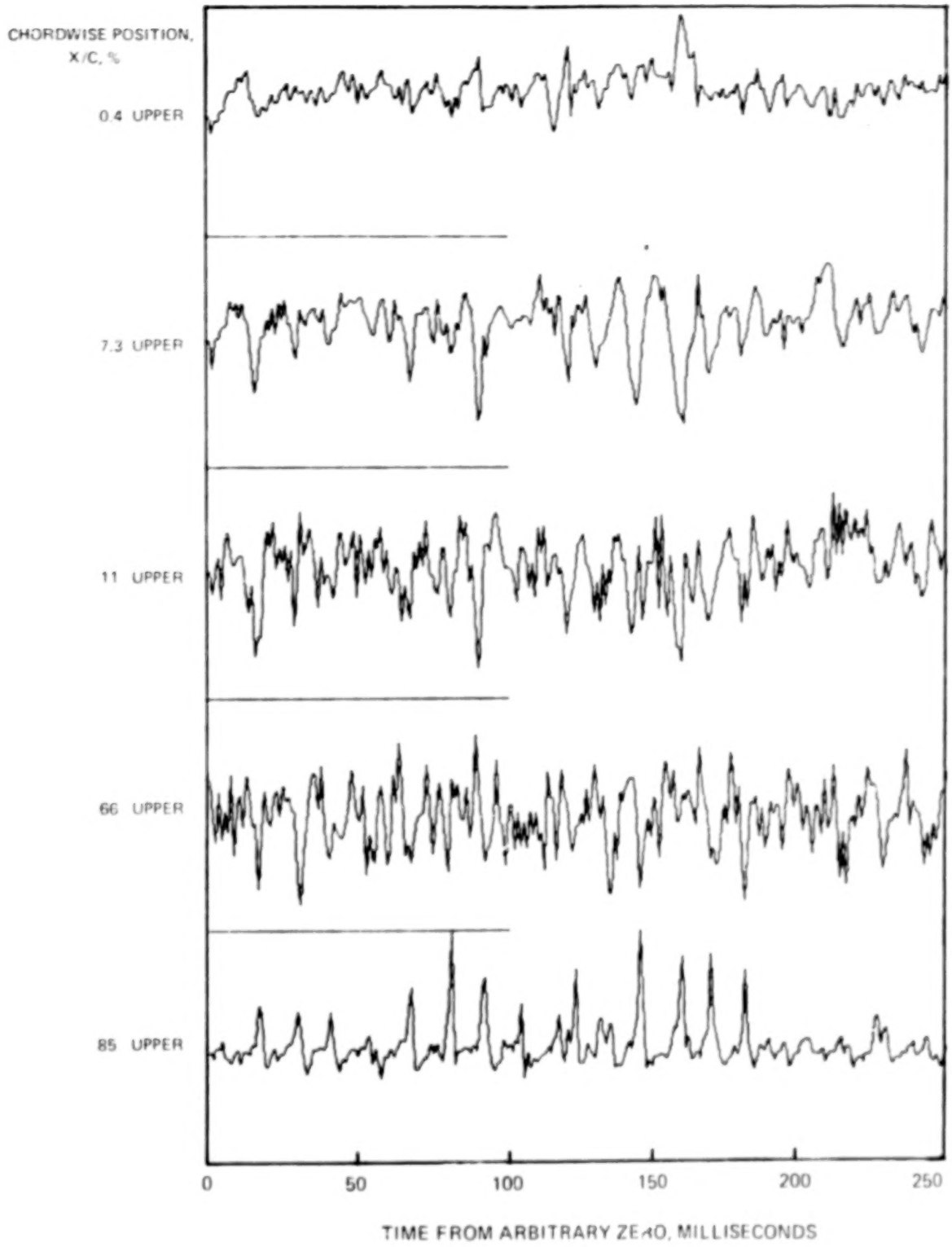

Figure 65 Self–Scaled Pressure Fluctuations on a Line Normal to the Leading Edge of a Steady 30° Swept NACA 0012 Airfoil at 0.30 Mach Number and 20° Angle of Attack Normal to the Leading Edge. (a) Upper Surface

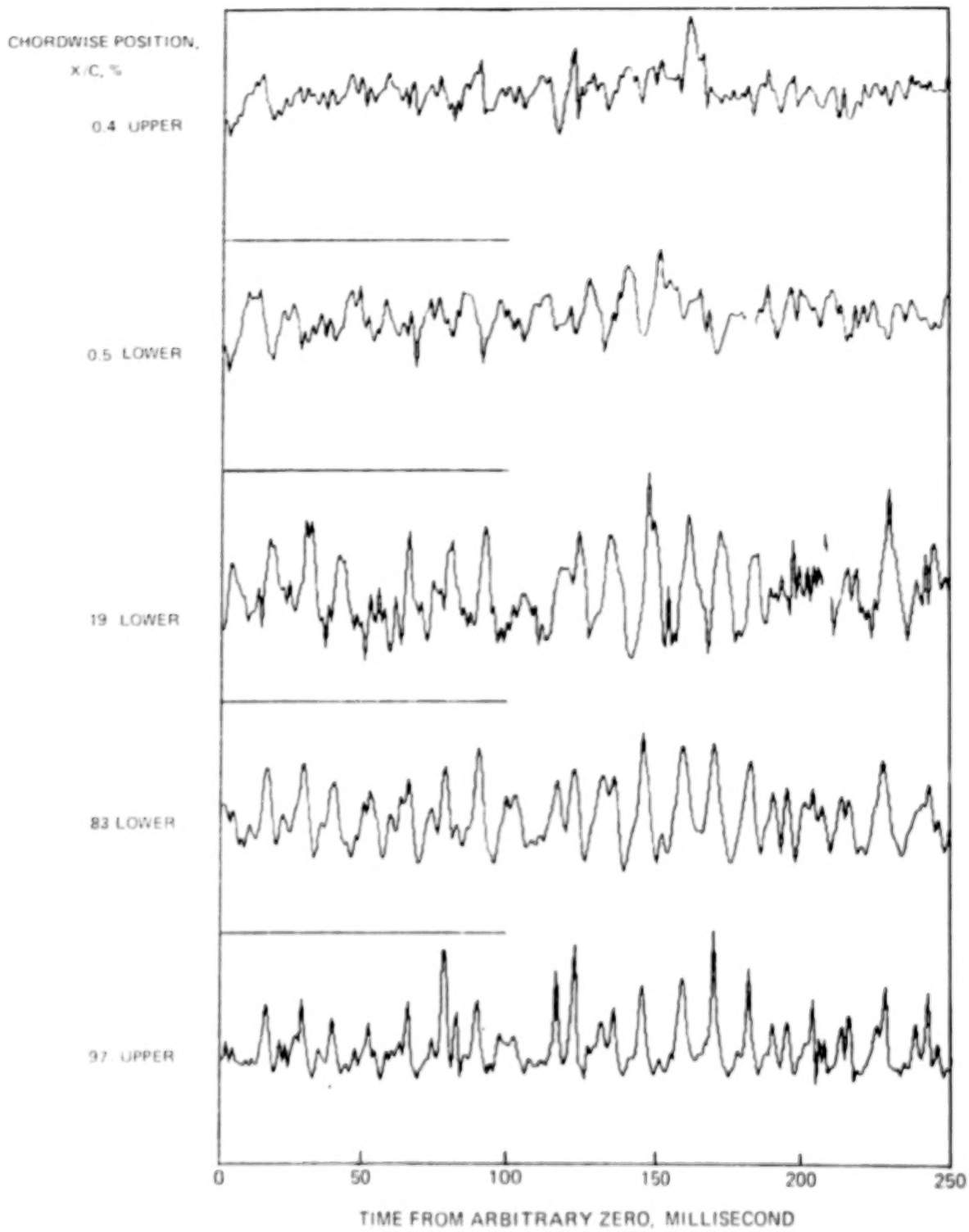

Figure 65 (Concluded) – (b) Lower Surface and Extremes of Upper Surface

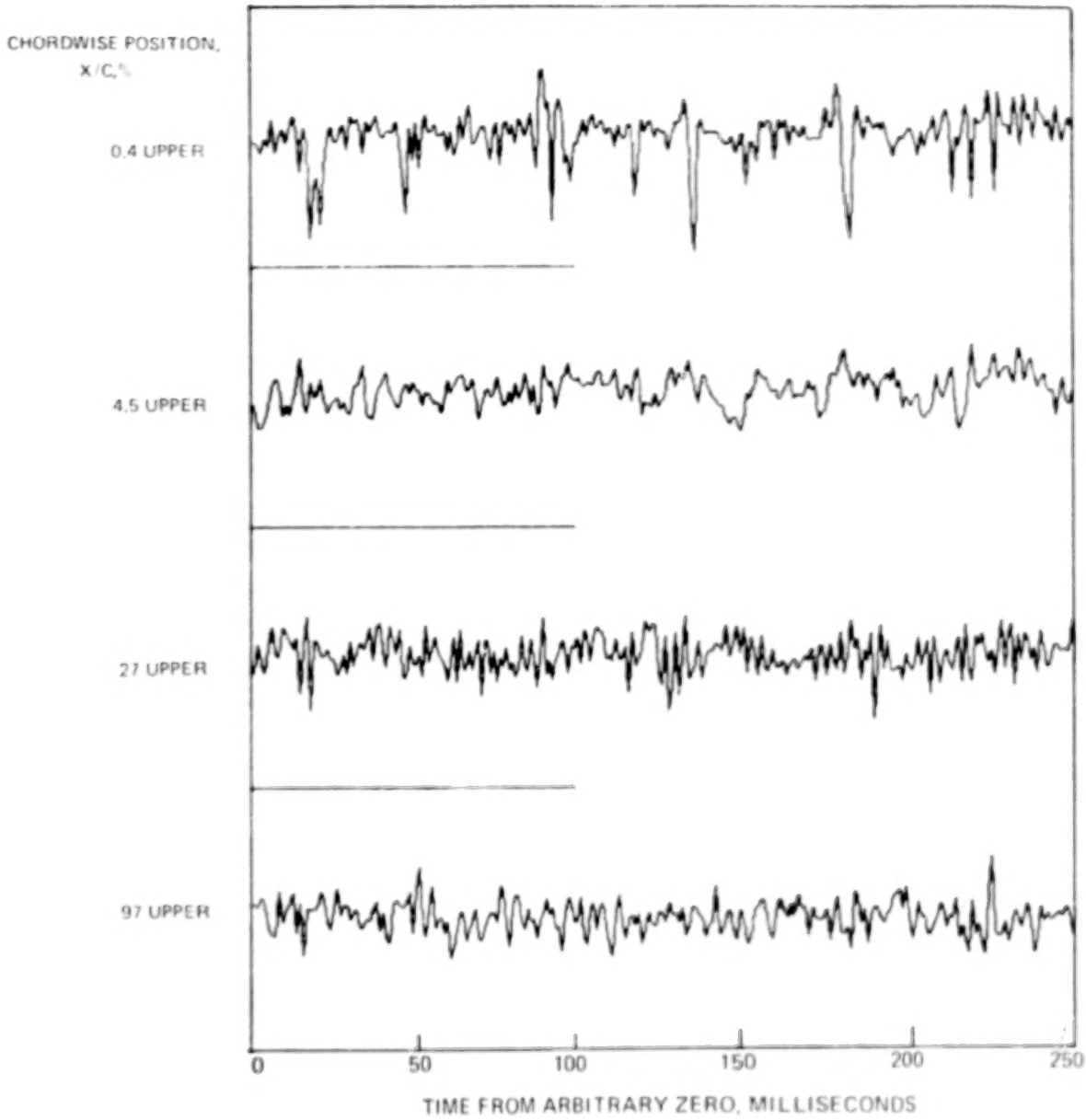

Figure 66 **Absolute–Level Pressure Fluctuations on a Line Parallel to the Free Stream Along the Upper Surface of a 30° Swept NACA 0012 Airfoil at 0.30 Mach Number and 16° Angle of Attack Normal to Leading Edge.**

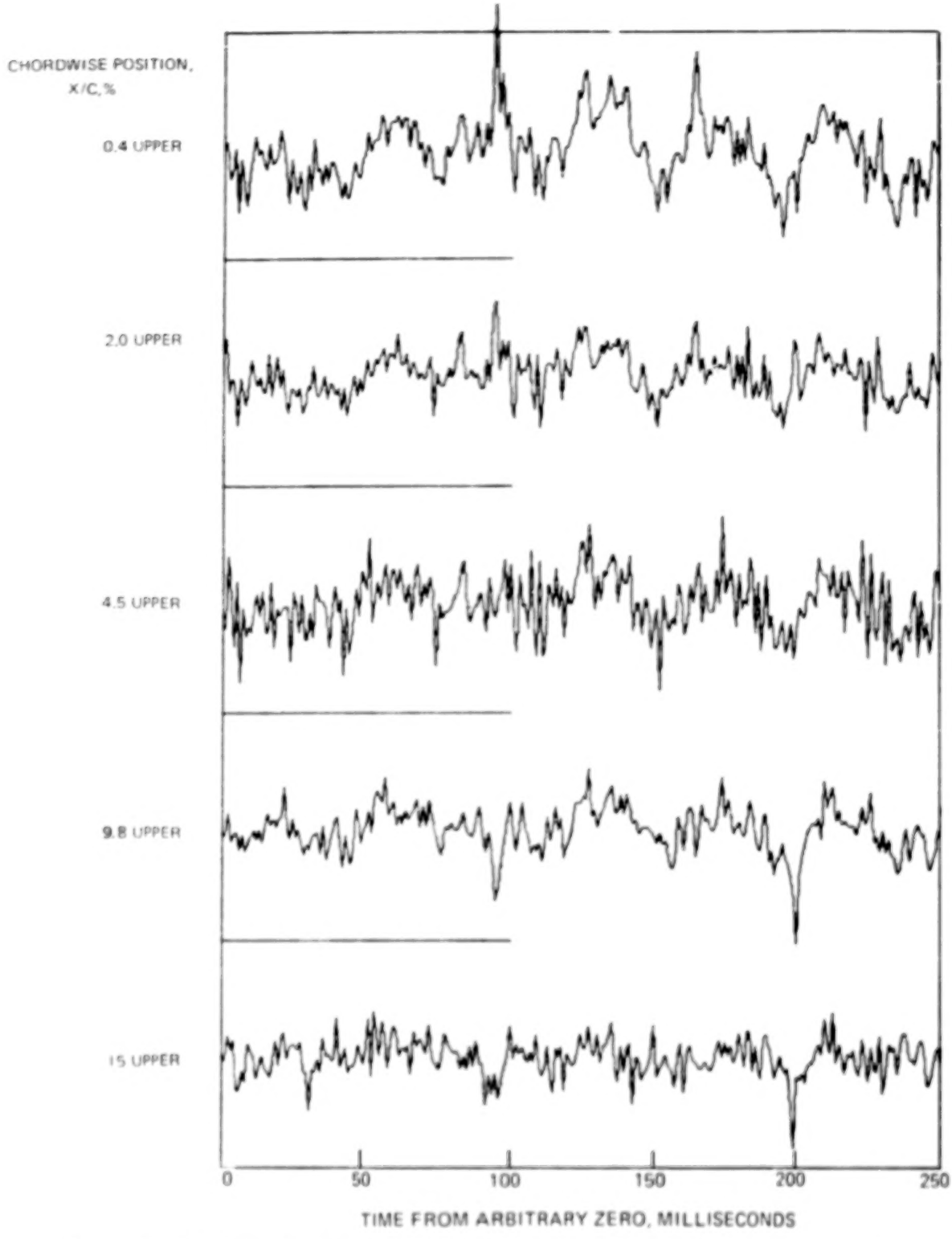

Figure 67 Absolute–Level Pressure Fluctuations on a Line Normal to the Leading Edge of a Steady 30° Swept NACA 0012 Airfoil at 0.40 Mach Number and 16° Angle of Attack Normal to the Leading Edge. (a) Forward Upper Surface

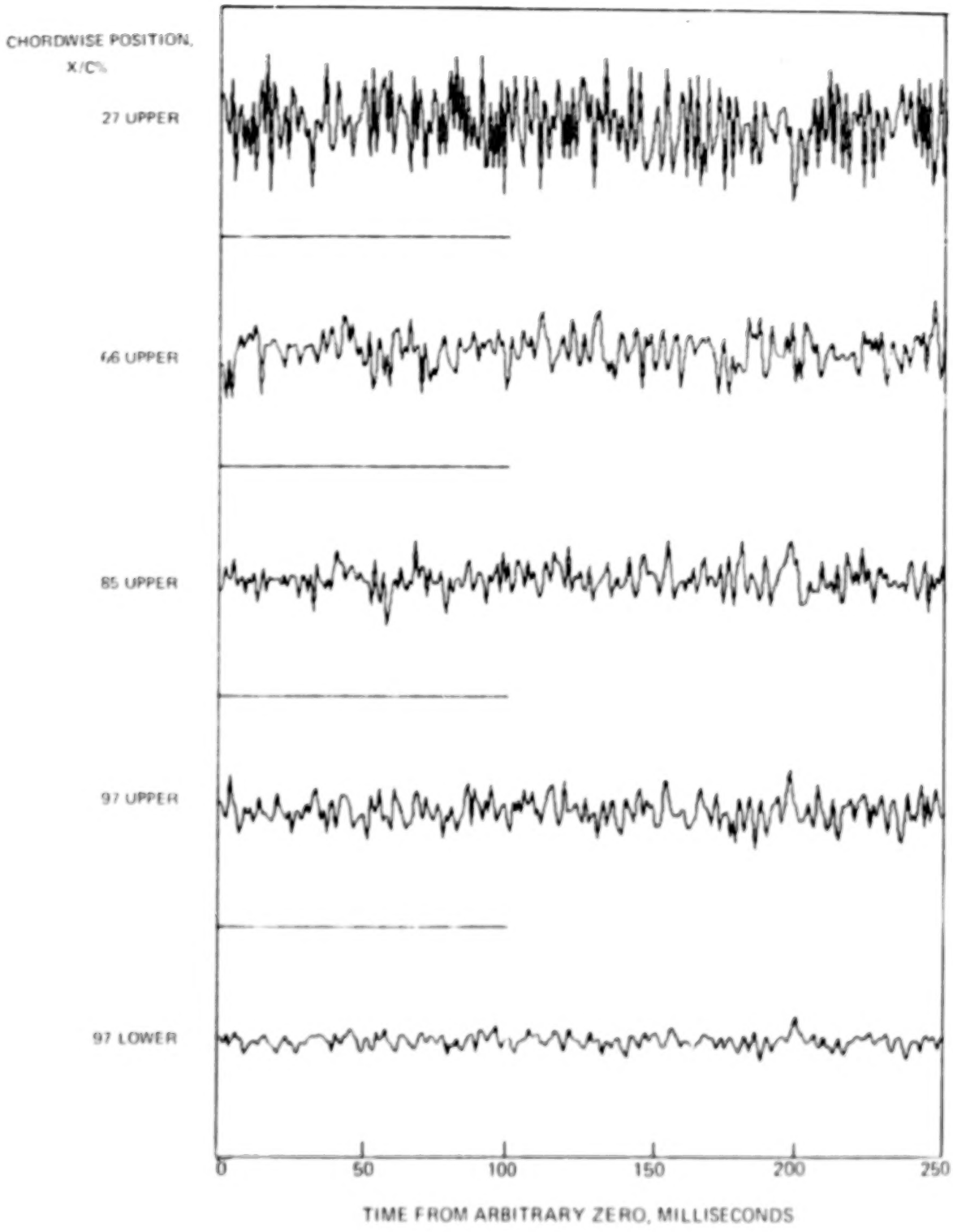

Figure 67 (Concluded)– (b)

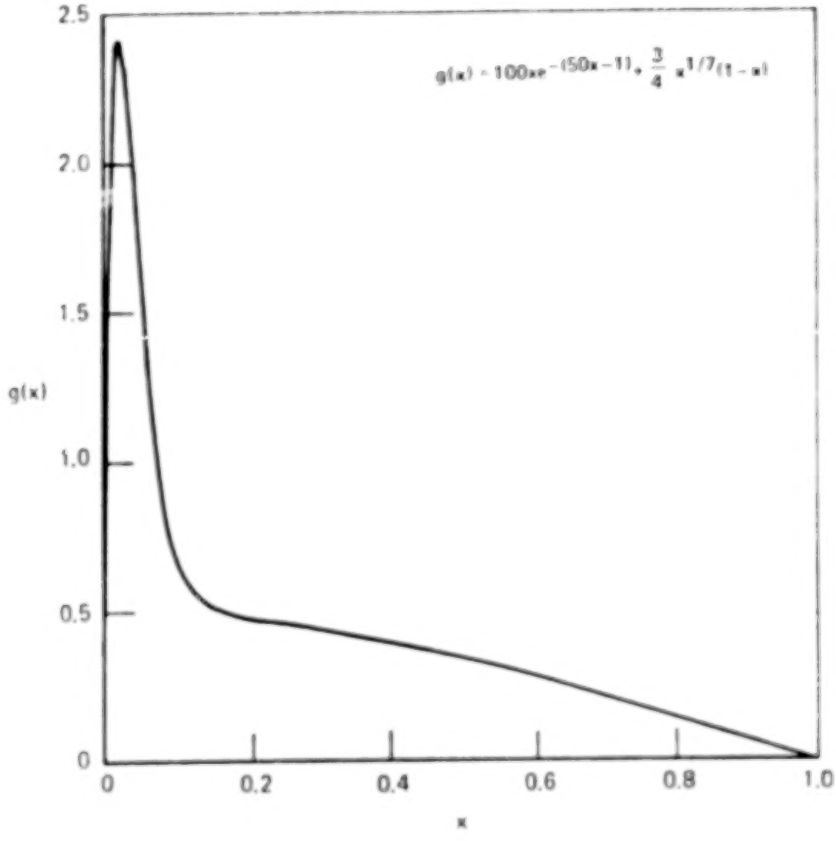

Figure 68 Analytical Simulation of Leading Edge Suction Peak.

BLANK

PAGE

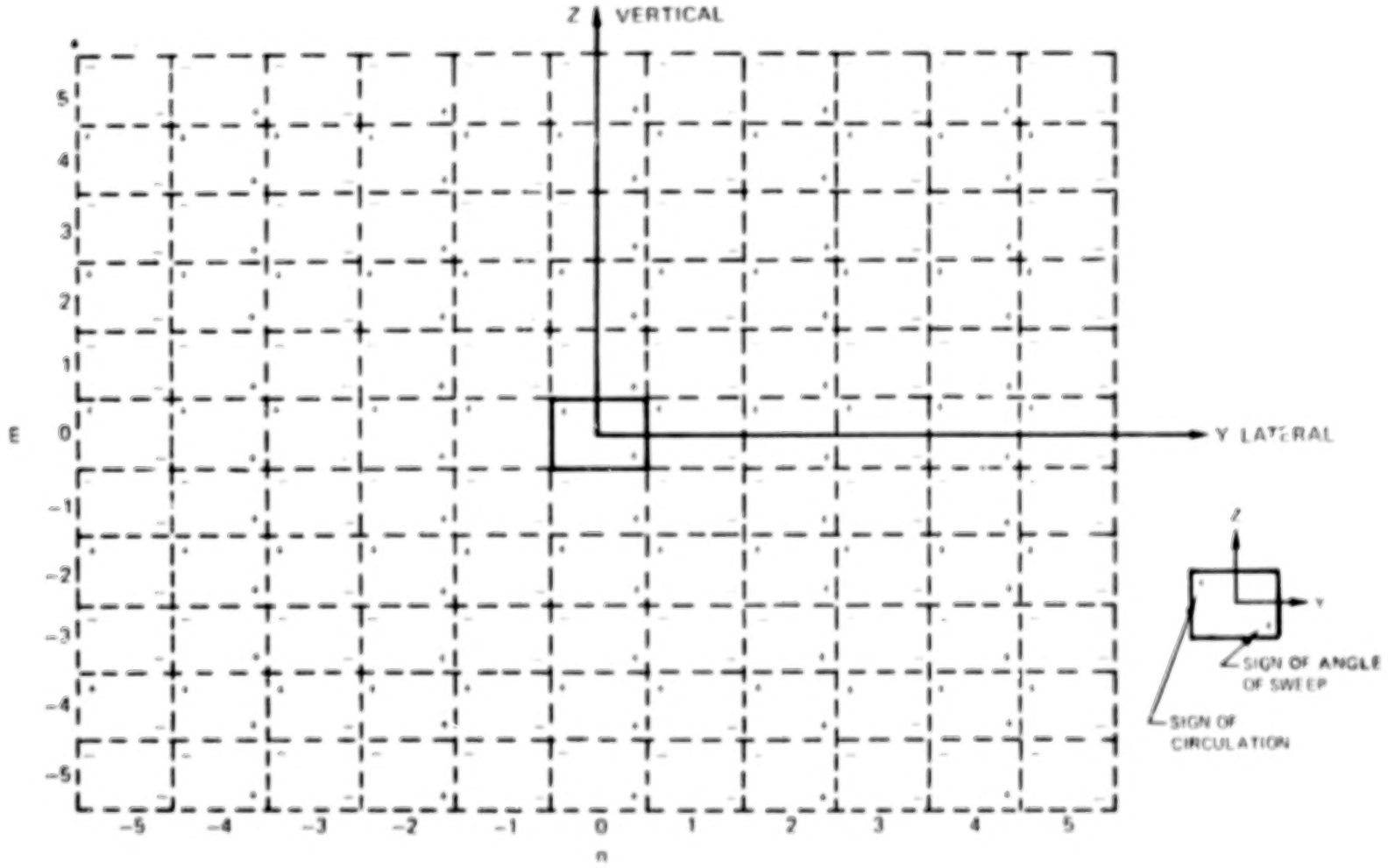

Figure 69 Image System Arrangement .

1 Report No	2 Government Accession No	3 Recipient's Catalog No
NASA CR-3092		

4 Title and Subtitle	5 Report Date
The Influence of Sweep on the Aerodynamic Loading of an Oscillating NACA 0012 Airfoil. Volume I - Technical Report	May 1979
	6 Performing Organization Code
7 Author(s) A. O. St. Hilaire, F. O. Carta, and M. R. Fink, United Technologies Research Center, and W. D. Jepson, Sikorsky Aircraft Division, U.T.C.	8 Performing Organization Report No
	10 Work Unit No
9 Performing Organization Name and Address United Technologies Research Center Silver Lane East Hartford, Conn. 06108	11 Contract or Grant No NAS1-14873
	13 Type of Report and Period Covered Contractor Report
12 Sponsoring Agency Name and Address National Aeronautics and Space Administration Washington, D.C. 20546	14 Sponsoring Agency Code

15 Supplementary Notes

Langley Technical Monitor: Warren H. Young, Jr.

Final Report

16 Abstract Aerodynamic experiments were performed on an oscillating NACA 0012 airfoil in the United Technologies Research Center (UTRC) Main Wind Tunnel utilizing a tunnel-spanning wing in both unswept and 30 degree swept configurations. The airfoil was tested in steady-state and in oscillatory pitch about the quarter chord. The unsteady aerodynamic loading was measured using pressure transducers along the chord. Numerical integrations of the unsteady pressure transducer responses were used to compute the normal force, chord force, and moment components of the induced loading.

The main objective of this report was to examine the effects of sweep on the induced aerodynamic load response. For the range of parameters tested, it was found that sweeping the airfoil tends to delay the onset of dynamic stall. Sweeping was also found to reduce the magnitude of the unsteady load variation about the mean response.

A stability analysis of the data was performed. It was determined that at mean incidence angle greater than 9 degrees, sweep tends to reduce the stability margin of the NACA 0012 airfoil; however, for all cases tested, the airfoil was found to be stable in pure pitch.

The fluctuating pressures on a steady airfoil in stalled flow were also examined. Turbulent eddies were found to convect downstream above the upper surface and generate forward-moving acoustic waves at the trailing edge which move upstream along the lower surface.

17 Key Words (Suggested by Author(s))		18 Distribution Statement
Aerodynamic Testing	Swept Wing Aerodynamics	Unclassified - Unlimited
Dynamic Stall	Trailing Edge Noise	
Oscillating NACA 0012 Airfoil	Turbulence Convection	
Pitching Oscillations	Unsteady Aerodynamics	Subject Category 02

19 Security Classif (of this report)	20 Security Classif (of this page)	21 No. of Pages	22 Price*
Unclassified	Unclassified	137	$7.25

* For sale by the National Technical Information Service, Springfield, Virginia 22161

NASA-Langley, 1979

90%

50%

END